# PHYSICOCHEMICAL PROPERTIES OF POLY (ε-CAPROLACTONE) AND MAGNESIUM OXIDE INCORPORATED POLY (ε-CAPROLACTONE) NANOFIBERS

A Thesis

By

DAISAKU GICHEHA

Submitted to the Office of Graduate Studies of
Prairie View A&M University
in a partial fulfillment of the requirements for the degree of

MASTER OF SCIENCE IN ENGINEERING, CHEMICAL ENGINEERING

August 2023

# PHYSICOCHEMICAL PROPERTIES OF POLY (ε-CAPROLACTONE) AND MAGNESIUM OXIDE INCORPORATED POLY (ε-CAPROLACTONE) NANOFIBERS

A Thesis

By

DAISAKU GICHEHA

Submitted to the Office of Graduate Studies of
Prairie View A&M University
in a partial fulfillment of the requirements for the degree of

MASTER OF SCIENCE IN ENGINEERING, CHEMICAL ENGINEERING

Approved as to style and content by:

| | |
|---|---|
| Dr. Nabila Shamim<br>Chair of Committee | Dr. Sheena M. Reeves<br>Member |
| Dr. Irvin Osborne-Lee<br>Member | Dr. Kazeem Olanrewaju<br>Member |
| Dr. Hongbo Du<br>Member | Dr. Sheena M. Reeves<br>Head of Department |
| Name<br>Dean of College | Name<br>Dean of Graduate Studies |

August 2023

Major Subject: Chemical Engineering

## ABSTRACT

Physicochemical properties of poly (ε-caprolactone) and MgO Incorporated PCL nanofibers

(August 2023)

Daisaku Gicheha, B.S., Prairie View A&M University

Advisor: Dr. Nabila Shamim

Polymer nanofibers are used to develop materials that possess customized characteristics for diverse applications. The applications of nanofibers are influenced by their significant surface-to-volume ratio, the porosity of the nanofiber lattice, and distinctive physicochemical characteristics. The molecular orientation of electrospun nanofibers is a crucial and intricate feature that has a direct impact on the structures and properties of the nanofiber mat. The utilization of Scanning Electron Microscopy (SEM), Fourier Transform Infrared Spectroscopy (FTIR), Differential Scanning Calorimetry (DSC), and X-Ray Diffractometry (XRD), facilitated the determination of the morphology, chemical structure, and thermal properties of nanofibers. The SEM analysis revealed that the nanofibers exhibited a random and interconnected orientation. The findings indicate that the level of crystallinity exhibited by the magnesium oxide incorporated PCL (ε-caprolactone) nanofibers, surpassed that of the PCL nanofibers. Increased crystallinity indicates chain mobility changes, leading to improved mechanical characteristics. Further evaluation was conducted on the DSC findings. The study delved into the kinetics of non-isothermal crystallization of PCL and MgO-PCL nanofibers with varying cooling rates.

The study used DSC-3 apparatus produced by Mettler Toledo to acquire crystallization information and investigate the kinetics behavior of the two types of nanofibers under different cooling rates ranging from 0.5-5 K/min. Several mathematical models, including Jeziorny, Ozawa, and Mo's models, were utilized to determine the parameters of non-isothermal crystallization kinetics. Mo's approach generates consistent ratios of Avrami exponent to Ozawa exponent (α) that are approximately 1.4 for PCL, MgO-PCL nanofibers, and bulk-PCL. The similarity of α values indicates that the structures of crystallization formed at different levels of relative crystallinity were analogous. The investigation with the Friedman method exhibited an increase in relative crystallinity was associated with a decrease in temperature and a rise in activation energy. According to the Kissinger and Friedman methodologies, it was observed that the activation energy of bulk-PCL was comparatively lower than that of PCL and MgO-PCL nanofibers. The observed phenomenon can be attributed to the nanoconfinement effect, which is characterized by geometric constraints imposed on PCL nanofibers.

**Keywords:** Poly (ε-caprolactone), magnesium oxide incorporated poly (ε-caprolactone), nanofibers, electrospinning; non-isothermal crystallization.

## DEDICATION

I want to dedicate my thesis to my mother Regina E. Gicheha, Fr. Robert Vujs, Gabriell Katembo, and my fiancée Annah Katembo. They have guided and supported me through my engineering studies. Also, my mentor Dr. Nabila Shamim for guidance throughout my research. I would not have been able to complete my studies without all their support.

## ACKNOWLEDGMENTS

I would like to thank God for giving me my health to pursue this degree. I am thankful to Dr. Nabila Shamim for her guidance throughout my entire graduate studies, giving me countless of advice as I started doing research. She has been my professor and mentor. I would also like to thank Dr. Sheena M. Reeves for teaching me chemical engineering principles as she was my professor in most of my bachelor's studies. I would also like to thank Dr. Irvin W. Osborne-Lee as he gave me countless pieces of advice when I joined my chemical engineering program and was my advisor all through my studies. I am so grateful for Dr. Kazeem Olanrewaju and Dr. Hongbo Du for being a part of my thesis committee members.

Lastly, I want to thank my friends and family for believing in me and encouraging me to finish my program. My mother Regina Gicheha, and my pastor Fr. Robert Vujs for being my supporters and encouraging me not to give up on my studies. I want to thank close friends such as Nigel Brooks and Erique Maingi for their moral support.

TABLE OF CONTENTS

Page

LIST OF FIGURES

FIGURE Page

## APPENDIX A: LIST OF FIGURES

FIGURE Page

LIST OF TABLES

TABLE Page

## APPENDIX A: LIST OF TABLES

TABLE Page

## NOMENCLATURE

| | |
|---|---|
| $D_{HKL}$ | Integral width (crystallite size) |
| DSC | Differential Scanning Calorimetry |
| F(T) | Cooling rate value chosen at a crystallization time when the system has a certain degree of crystallinity |
| FTIR | Fourier Transform Infrared |
| FWHM | Full width at half maximum |
| MgO | Magnesium Oxide |
| PCL | Poly (ε-caprolactone) |
| PLA | Polylactic acid |
| PLGA | Poly(lactic-co-glycolic acid) |
| SEM | Scanning Electron Microscopy |
| USFDA | U.S. Food and Drug Administration |
| XRD | X-ray Diffraction |
| $\Delta H_c$ | Enthalpy of crystallization |
| $\Delta H_c^\circ$ | Theoretical enthalpy value for 100% PCL |
| $\Delta E$ | Activation energy |
| $t_c$ | Crystallization time |
| $T_{endset}$ | The temperature determined by extrapolating the baseline from the point of intersection after thermal effect. |
| $T_o$ | The temperature determined by extrapolating the baseline from the point of intersection before thermal effect |
| $T_P$ | Temperature at the extreme point of the peak |

| | |
|---|---|
| R | Universal gas constant (J $mol^{-1}$ $K^{-1}$) |
| wt.% | Weight percentage |
| X(t) | Relative degree of crystallization |
| $Z_c$ | Corrected crystallization rate constant |
| $Z_t$ | Avrami crystallization rate |
| Ψ | Weight fraction of the polymer |
| λ | Wavelength |
| *n* | Avrami exponent |
| β | Cooling rate (K/min) |
| *α* | Ratio of Avrami exponent and Ozawa exponent |
| *m* | Ozawa exponent |

# 1. INTRODUCTION

The emergence of nanotechnology and nanoscience in the 1930s [1], has sparked considerable attention toward biodegradable polymeric nanofibers across various fields, including tissue engineering [2], wound dressing [3], oral drug delivery [4], dentistry [5], fixation devices [6], contraceptive devices [7], sutures [8] and others. Polymeric nanofibers, possessing a diameter ranging from 1nm to 1000 nm and exhibiting a high surface-to-volume ratio, have been identified as a potential material for scaffold fabrication [9]. These scaffolds' properties resemble the properties of the extracellular matrix (ECM) of a given tissue [10]. However, the mechanical properties of nanofibers significantly impact their practical applications, which can be adjusted by manipulating their internal structure, including their nanoscopic and substructural features [11]. Hence, a thorough investigation of the internal structure of polymeric nanofibers is imperative for optimizing their performance, an area that has yet to be extensively explored. The molecular orientation of the polymer has an impact on the structure and properties of nanofibers [12]. The high draw ratio associated with decreasing nanofiber diameter can amplify molecular orientation, as previously noted [13]. Acquiring the morphology of amorphous polymers is challenging due to the absence of an ordered and noticeable substructure, as noted in previous studies [14, 15].

---

This thesis follows the style of the Journal *Polymer.*

Polymer nanofibers are fabricated in various methods, such as melt spinning [16], electrospinning [17], and solution spinning (also categorized as dry and wet spinning) [18]. The electrospinning method is highly versatile due to its cost-effectiveness and efficiency, as supported by previous studies [19, 20]. Additionally, it has been suggested that this technique can produce results comparable to those achieved with extracellular matrix (ECM) tissue [21]. The various techniques employed in electrospinning can be categorized into blend/single-jet electrospinning, coaxial electrospinning, emulsion electrospinning, and needless electrospinning method [22]. The present investigation involved the fabrication of polymer nanofibers through the blend/single-jet electrospinning technique, a commonly employed method for engineering nanofibers.

Poly (ε-caprolactone) (PCL) is an aliphatic polyester that is both hydrophobic and semi-crystalline and is known for its favorable mechanical properties [23]. The commercial utility of PCL nanofibers has been widely recognized owing to their biocompatibility [24], biodegradability [16], low cost [25], and its U.S. Food and Drug Administration (FDA) approval to be used in human beings [26]. However, PCL has a disadvantage by itself due to its stiffness and hydrophobic nature [23]. This can be optimized by blending with another hydrophilic polymer [24] or performing chemical treatment [27].

As previously stated, PCL is an aliphatic synthetic polymer and highly hydrophobic. According to Edwards et al. [28], the combination of natural and synthetic polymers may result in the formation of harmful residues due to the necessity of utilizing chemical crosslinking agents to uphold their mechanical properties and structural integrity. Rijal et al. [29] fabricated PCL-CS/MgO and PCL/MgO nanofibers and their

results were highly favorable as all nanofibers showed satisfactory mechanical properties. They reported that the natural polymer Chitosan (CS)'s biological properties were preserved, while synthetic PCL's mechanical properties were maintained by blending these materials with inorganic MgO. This blending approach obviated the need for chemical crosslinking and the attendant toxic residues. Magnesium oxide (MgO) is an inorganic salt that facilitates the release of Mg++ ions. These ions are crucial in repairing nerve or damaged tissue for human metabolism and skeletal development [30, 31]. The selection of MgO in this research was based on its advantageous biodegradability and biocompatibility properties. Studies have shown that elevating the level of crystallinity can prolong the degradation and drug release kinetics of polycaprolactone (PCL). The manifestation of this phenomenon has been exhibited in thin coatings and small spherical particles. The investigation of post-drawn nanofibers has yet to include an analysis of crystallization kinetics, optimal temperature, and overall crystallinity alterations.

The current investigation aimed to examine the correlation between the structure and properties of PCL and MgO-PCL nanofibers through the utilization of various analytical techniques, including Differential Scanning Calorimetry (DSC-3), X-ray Diffraction (XRD), Fourier Transform Infrared (FTIR), Scanning Electron Microscopy (SEM), and Contact Angle. The crystal and chemical structure of the nanofibers are determined using XRD and FTIR, respectively [32]. The overall research goals for this study were:

1. Characterize nanofibers composed of polycaprolactone (PCL) and magnesium oxide (MgO)-PCL and conduct a comparative analysis of these nanofibers with bulk-PCL.

2. Examine the non-isothermal crystallization process of PCL and MgO-PCL nanofibers and conduct a comparative analysis with bulk-PCL.
3. Determine the crystallization kinetics of PCL and MgO-PCL nanofibers and compare them to bulk-PCL.
4. Determine activation energy of crystallization for PCL and MgO-PCL nanofibers, and compare it to that of bulk-PCL.

The objectives of this investigation were attained through the execution of the subsequent tasks:

**Task 1:** Conduct X-ray diffraction (XRD) and differential scanning calorimetry (DSC) analyses to determine the crystal structure of bulk-PCL, PCL, and Mg-PCL nanofibers. Analyze the results obtained from the XRD and DSC analyses to gain insights into the crystal structure of the materials, as mentioned earlier.

**Task 2:** Conduct an examination and evaluation of the chemical composition of Poly(ε-caprolactone) (PCL) and Magnesium-PCL (Mg-PCL) nanofibers through the utilization of FTIR.

**Task 3:** Conduct a morphological characterization analysis of Poly(ε-caprolactone) (PCL) and Magnesium-PCL (Mg-PCL) nanofibers utilizing SEM.

**Task 4:** Perform contact angle analysis of PCL and Mg-PCL nanofibers.

**Task 5**: Examine and evaluate non-isothermal crystallization kinetics for bulk-PCL, PCL, and Mg-PCL nanofibers.

Chapter 2 comprises a literature review on PCL and Mg-PCL nanofibers and an examination of the crystallization kinetics equations employed in relevant research. Chapter 3 presents the materials and methods employed in the current investigation.

Chapter 4 presents the experimental data results for the characterization of bulk-PCL, PCL, and MgO-PCL nanofibers. In Chapter 5, an examination is conducted on the non-isothermal crystallization process of PCL and MgO-PCL nanofibers, with a comparative analysis of bulk-PCL samples. Chapter 6 analyzes prospective investigations of nanofibers, while Chapter 7 presents a comprehensive summary and conclusion of the research.

# 2. LITERATURE REVIEW

## 2.1 Nanofibers

Polymer nanofibers are gaining significant attention for their potential in developing materials with tailored properties for various applications, including but not limited to oral drug delivery [33], wound healing [34], fine particle filtration [35], tissue engineering [36], optoelectronics [37], and sensor technology [38]. The utilization of nanofibers is contingent upon their significant surface-to-volume ratio, the porosity of their nanofiber mesh, and their unique physicochemical characteristics. The molecular orientation of electrospun nanofibers is a critical and complex feature that directly influences the structures and properties of the resulting nanofiber mat. Polymers' characteristics are influenced by their chemical composition, chain conformation, molecular weight, and condensed structure formed during processing. Therefore, it is crucial to comprehensively examine the internal structure of polymeric nanofibers to enhance their efficiency, a domain that has yet to be extensively explored.

## 2.2 Electrospinning Process

The process of electrospinning involves the generation of submicron and nano-size fibers with high surface area through the spinning of polymer solutions in a high electric field [39]. The electrospinning process involves the application of a high direct current (DC) electric field or electrostatic force to the surface of a polymeric solution. The high voltage serves to overcome the solution's surface tension and viscoelastic forces, producing a slender, charged jet [40]. The electrospinning process transpires in the following manner: a fine jet erupting from the tip of a capillary tube is attributed to the increase in the intensity of shearing forces resulting from mutual charge repulsion

under the influence of an applied electric field. These forces are observed to surpass the effects of surface tension and viscoelastic forces. The jet undergoes a transition from initial stability to a state of bending instability, characterized by plastic stretching, bending, pirouetting motion, evaporation of the jet, and looping pattern with growing amplitude. This leads to the formation of an ultrafine nonwoven mesh of fibers on a collector screen, which is positioned at a certain distance from the capillary tube, as reported in reference [41]. The instability of a jet induces thinning of fibers and subsequent solvent evaporation during its transit through a brief aerial distance, leading to whipping. The fiber undergoes bending and twisting due to the occurrence of whipping instability. The electrospinning process is illustrated in Figure 1. The process of electrospinning has gained significant popularity in the production of nanofibers. It has been observed that a majority of polymers can be utilized for electrospinning, provided they can be dissolved in solvents that are suitable and do not result in any form of degradation. The utilization of Polycaprolactone (PCL) has been extensively employed in the fabrication of 3D scaffolds within the biomedical domain due to its relatively lower acidic degradation in contrast to other polyesters, as well as its potential for loadbearing purposes [42]. Section 2.3 provides a detailed discussion on PCL.

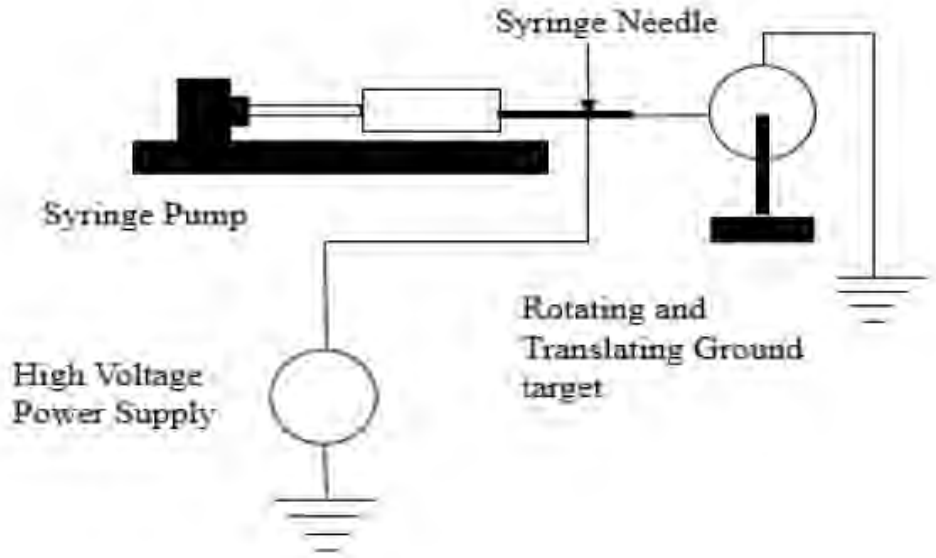


**Figure 1.** Schematic of an electrospinning system.

### 2.3 Poly (ε-caprolactone) (PCL)

Poly(ε-caprolactone) (PCL) is synthesized through the process of ring-opening polymerization of the cyclic monomer ε-caprolactone, as illustrated in Figure 2 [43]. A catalyst, such as stannous octoate, facilitate the polymerization process. The weight of the resulting polymer can be regulated by utilizing low molecular-weight alcohols, as previously noted [44]. It is a semi-crystalline polymer with a low melting point of 59-64°C, a glass-transition temperature of -60°C, and a rubbery state at room temperature [45].

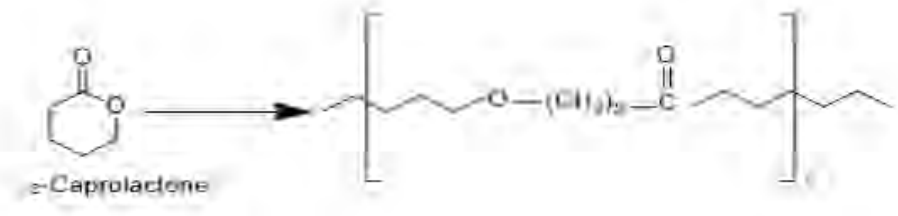


**Figure 2.** Ring opening polymerization of ε-caprolactone to polycaprolactone.

At ambient temperature, PCL exhibits solubility in organic solvents such as chloroform, dichloromethane, carbon tetrachloride, benzene, toluene, cyclohexanone, and 2-nitropropane. The substance exhibits a reduced solubility in 2-butanone, ethyl acetate, dimethylformamide, and acetonitrile, while it is deemed insoluble in alcohol, petroleum ether, and diethyl ether [46]. PCL has been observed to enhance stress crack resistance, dyeability, and adhesion when combined with other polymers. Its compatibility has been explored with various polymers, including cellulose propionate, cellulose acetate butyrate, polylactic acid, and polylactic acid-co-glycolic acid, to regulate the drug release rate from microcapsules [47].

PCL is the most biomedically suited polymer that is designed for long-term drug delivery systems due to its biophysical properties [48]. The utilization of PCL fiber in three-dimensional scaffolds for tissue engineering purposes has been the subject of recent investigation [48]. Previous studies show that modifying a polymer for drug delivery purposes alters its properties, including but not limited to ionic property, crystallinity, solubility, and degradation pattern [48]. PCL is an aliphatic, bio-degradable polyester commonly used for implantable biomaterials due to its non-toxic and crystallizable nature. The non-toxic and biodegradable properties of PCL render it suitable for various applications, including but not limited to drug delivery systems and medical, pharmaceutical, and tissue engineering [49]. The non-toxicity and biodegradability make PCL suitable for tissue engineering. The biodegradability of a solid polymer is influenced by its chemical structure and the degradation rate of semi-crystalline PCL that is primarily influenced by its crystallinity [50]. According to existing literature, the viscoelastic properties, crystallinity level, and crystals' size in electrospun mats are

affected by the orientation of molecules [51]**.** Hence, investigating the crystal kinetics of PCL nanofibers in depth is a compelling area of academic inquiry.

### 2.3.1 Application of Nanofibers

The biodegradability, biocompatibility, pliability, good solubility, low melting point, and exceptional blend compatibility of PCL have significantly influenced extensive research into its applications in biomedical fields [47, 52, 53]. PCL fibers have been utilized in various biomedical applications, including but not limited to sutures, pharmaceuticals, and tissue engineering.

### 2.3.2 Pharmaceuticals

Pharmaceutical substances have been extensively utilized to enhance well-being and extend lifespans. Drug delivery systems have been developed to facilitate the targeted release, activation, and localization of drugs to specific sites within the body. The year 1970 marked the development of a polymer known as poly(lactic-co-glycolic acid) (PLGA), which was designed to be biodegradable and utilized for the controlled release of narcotics. The permeability of PCL to numerous drugs, its biocompatibility, and its ability to be eliminated from the body upon bio resorption render it a viable option for employment as a controlled drug delivery system. Furthermore, in comparison to other polymers, its biodegradation rate is comparatively slower, rendering it more appropriate for extended delivery purposes. The degradation kinetics of PCL may be influenced by its compatibility blends with other polymers or inorganic nanoparticles which can be customized to achieve specific release profiles [54, 55]. Drug delivery systems utilizing nanoparticle-incorporated PCL have been developed to facilitate the controlled release of therapeutic agents within the human body. These systems include

various types of vehicles, such as nanospheres, microspheres, microcapsules, microfibers, and nanofibers.

### 2.3.3 Tissue Engineering

The field of tissue engineering involves the application of engineering principles and techniques to develop biological substitutes that can restore, maintain, or improve tissue function. The interdisciplinary domain of tissue engineering pertains to the application of engineering and life sciences principles in creating biological replacements that aim to reinstate, sustain, or enhance tissue function or an entire organ [56]. The deprivation of an organ or tissue can adversely affect a patient's health. According to Langer et al [56], the annual cost of healthcare in the United States is significantly impacted by the loss of tissue or organs, accounting for approximately 50% of the total cost, which amounts to over 400 billion dollars. As a result of this prominent concern, there have been noteworthy scientific developments in biomaterial research aimed at generating novel tissues and organs. Such developments have been achieved by constructing tissues utilizing a blend of matrix scaffolds, cells, and biologically active molecules [49].

Various scaffolds have been utilized in tissue engineering research within biomaterials. The scaffolds necessitate specific attributes, including a three-dimensional and extensively porous structure that features an interconnected pore network to facilitate cell growth and transport nutrients and metabolic waste. Additionally, they must be biocompatible and bioresorbable, with a degradation and resorption rate that can be controlled to align with cell and tissue growth in vitro and/or in vivo. The scaffolds must also possess surface chemistry appropriate for cell attachment, proliferation,

differentiation, and mechanical properties that correspond to those of the tissues at the implantation site [57].

The manipulation of physical properties, such as degradation rate and mechanical strength, gives synthetic polymers an advantage over natural polymers. PCL is considered the most suitable candidate for scaffold fabrication among the various categories of biodegradable polymers. The versatility of PCL as a bioresorbable polymer and its rheological properties enables the production of a diverse array of scaffolds. PCL can be utilized to produce 3D polymeric scaffolds with increased porosity and surface area, akin to its application in the textile industry. The utilization of this particular manufacturing technique in tissue engineering is attributed to its notable surface area advantage during application. The scaffolds are fabricated into slender meshes, thereby augmenting their permeability. Achieving the best mechanical and chemical properties for the suitable application, it is reported that tailored composite nanofibers have exhibited significant potential for biomedical applications in addition to polymeric nanofibers [42, 58].

## 2.4 Magnesium Oxide (MgO)

Magnesium (Mg) is essential for the optimal functioning of nerve tissue and recovery from nerve damage, as indicated by previous studies [30, 31, 59]. The selection of MgO in this research was based on its advantageous biodegradability and biocompatibility properties. Studies have shown that elevating the level of crystallinity can prolong the degradation and drug release kinetics of polycaprolactone (PCL) [60, 61]. For example, adding MgO in a polymer tailored to possess specific properties suitable for drug delivery, as reported in the literature [48]. According to Daniel et al. [62],

incorporating MgO nanoparticles in various polymer composites has been implemented to enhance their antibacterial properties. MgO possesses several characteristics that render it a highly desirable nanomaterial, including but not limited to its low density, high strength-to-weight ratio, biodegradability, and biocompatibility. The characteristic mentioned above renders MgO a compelling nanomaterial with diverse applications in the biomedical sector. MgO has diverse applications beyond the biomedical sector, including but not limited to the agricultural, anti-microbial, and environmental industries. The selection of MgO for this study was based on its safety profile, which the FDA has endorsed.

### 2.5 Nanocrystalline Phase in Electrospun Fiber

Electrospinning has been the most prevalent technique for producing nanofibers. Due to the rapid stretching of the electrical jet and evaporation of the solvent during the Electrospinning (ES) process, a portion of the polymer remains non-crystalline. The non-crystalline polymer chain eventually becomes entrapped between the growing crystals [63]. Recent research by Soleimani et al. [18] on the structure-property relationship of randomly aligned polylactide, revealed that spun fibers consist of crystalline and mesomorphic phases as well as oriented but mobile amorphous chain segments.

Therefore, the interpretation of the non-crystalline phase of electrospun fibers is of interest and can enhance the phase confinement effect in nanofibers. In addition, such research necessitates approaches to molecular orientation and molecular simulation to characterize the freeze-in stress that influences the nucleation mechanism and crystalline structure. The molecular orientation of electrospun nanofibers is a crucial characteristic that has a direct impact on the microstructure and properties of both the individual fibers

and the scaffold. Fiber orientation in tissue engineering has garnered increasing attention due to its potential to facilitate fiber-guided cell growth. Thermal analysis is a method to scrutinize the alterations in the structural composition of semi-crystalline polymer fibers. The objective is to evaluate the impact of fiber conformation on mobility. Recently, Xu et al. [32] reported the presence of cylinder-like structures in ES polycarbonate fibers, which resemble the super molecular structure that was initially hypothesized by Arinstein et al. [64]. Similarly, Ma et. al. [63] also reported that the entrapment of non-crystalline polymer chains occurs during crystallization, wherein they become embedded between the growing crystals within or outside the lamella structure, as illustrated in Figure 3. The present study examined the crystal kinetics of said crystals that undergo growth while confined. However, several aspects of the relationship between structure and property still require further investigation. Therefore, it is crucial to comprehensively examine the internal structure of polymeric nanofibers to enhance their efficiency, a domain that has yet to be extensively explored.

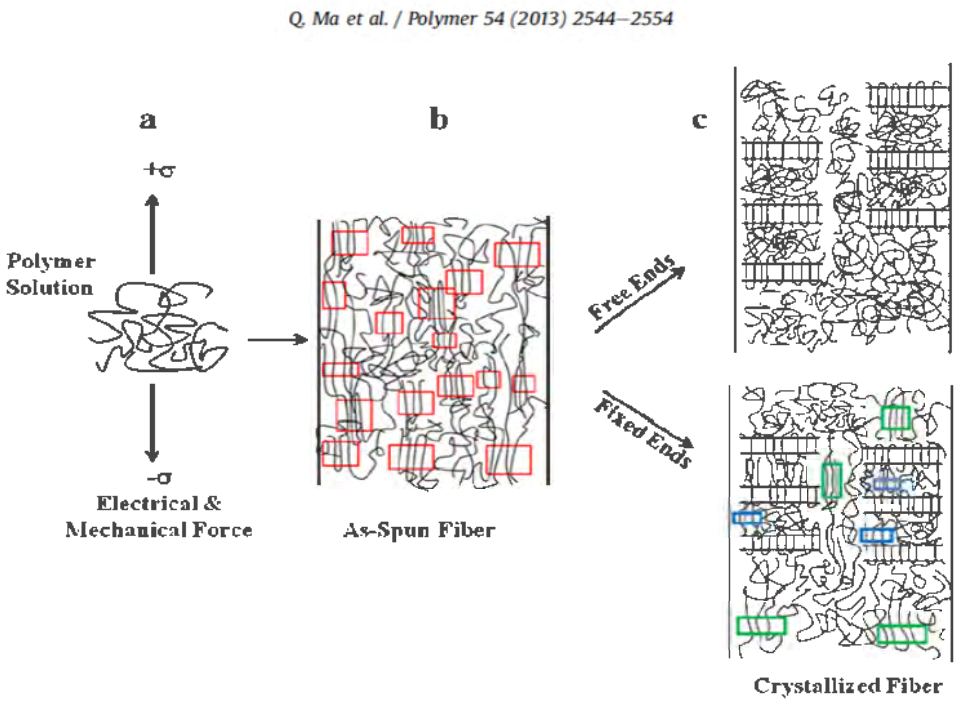


**Figure 3.** Schematic diagram of phase structure and molecular orientation for spun Polylactic acid (PLA) and crystallized fibers [63].

### 2.5.1 Analysis Methods

The non-isothermal crystallization in bulk-PCL, PCL, and MgO-PCL nanofibers is accurately investigated through DSC. It has been demonstrated that augmenting the level of crystallinity can result in a favorable outcome of prolonging the kinetics of degradation/drug release in PCL. The manifestation of this phenomenon has been exhibited in thin layers and small spherical particles. The post-drawn nanofibers have yet to be investigated regarding their crystallization kinetics, optimal temperature, and overall alterations in crystallinity. In general, isothermal crystallization kinetics is analyzed by Avrami model [65]. However, in non-isothermal process crystallization temperature changes with time and therefore, modified Avrami models such as Jeziorny [66]and Mo's model [66, 67], have been utilized to investigate the intricacies of non-isothermal crystallization dynamics. The Kissinger [67] and Friedman [68] models are

widely used to determine the activation energy of a polymer that is confined within electrospun nanofibers.

### 2.5.2 Crystallization

Crystallization is a phenomenon characterized by the transition of a substance from a liquid state to a solid state. However, the phenomenon of nanoconfinement significantly impacts the process of crystal formation, leading to modifications in the behavior of crystallization. Samanta et al. [67] reported that the crystallization temperature of a confined PEO sample was lower than that of bulk PEO. The findings from their study suggests that the change in degree of crystallinity is a structural attribute that impacts the surface characteristics relevant to drug loading and release kinetics. Hence, comprehending the crystallization mechanism of nanofibers is of utmost importance in customizing scaffolds for biomedical purposes.

### 2.5.3 Non-isothermal Crystallization

The present focus of research in polymer processing is to gain a comprehensive understanding of the non-isothermal crystallization behavior of polymers because such processing is typically conducted under non-isothermal conditions [67]. Various industrial processes, such as extrusion, injection molding, film blowing, and foaming, occur within a thermal environment that undergoes continuous fluctuations, commonly called non-isothermal conditions. Several models, including Ozawa, Avrami, and Mo's method, developed to assess non-isothermal crystallization using experimental data obtained from DSC are discussed in the following section.

## 2.6 Crystallization Kinetics

Differential scanning calorimetry (DSC) measurements were employed to examine the behavior of bulk-PCL, PCL, and MgO-PCL nanofibers. The Avrami model is a widely used theoretical framework to explain crystal kinetics for isothermal crystallization [65]. The current study pertains to the process of non-isothermal crystallization. It utilizes Jeziorny's [66], Ozawa's [69, 70], and Mo's [66, 67] methods, which will be elaborated upon in the following sections. Furthermore, the methodologies proposed by Kissinger and Friedman are examined to determine activation energy in bulk and confined polymer nanofibers.

### 2.6.1 Avrami

Avrami equation describes how phase changes occur in solid materials as relative function of time X(t). Relative crystallinity is described as shown in Equation (1) [65]:

$$1 - X(t) = e^{-Z_t t^n} \quad (1)$$

where $Z_t$ is Avrami crystallization rate, t is crystallization time and n is Avrami exponent. $Z_t$ and $n$ parameters can be calculated by transforming Equation (1) into a traditional linear form of Equation (2):

$$log\{-ln[1 - X(t)]\} = \log Z_t + n\, logt \quad (2)$$

Plotting log{- ln[1-X(t)]} against log t, $Z_t$, and n parameter, can be solved linearly as intercept and slope, respectively. In this study, Equation (2) is used to generate non-isothermal crystallization plots of bulk-PCL, PCL, and MgO-PCL nanofibers at different cooling rates.

### 2.6.2 Jeziorny Method

The Jeziorny model postulates a constant crystallization temperature and adjusts Avrami parameters to evaluate non-isothermal crystallization kinetics in polymers. This is achieved by assuming a constant cooling rate, as demonstrated in Equation (3). The corrected crystallization rate constant is shown below:

$$\log Z_c = \log Z_t/\beta \quad (3)$$

where $Z_c$ parameter can describe the non-isothermal crystallization kinetics that has been corrected in order to consider the effect of the cooling rate when the experiment was performed for polymers (also known as modified crystallization rate constant) and $\beta$ is the cooling rate. Jeziorny parameters $Z_c$, $Z_t$ and Avrami exponent, *n* can be determined by plotting $log\ \{-ln[1-X(t)]\}$ against *log t* using the following Equation (4).

$$log\ \{-ln[1-X(t)]\} = \mathrm{n}\log \mathrm{t} + \log Z_t \quad (4)$$

### 2.6.3 Mo's Method

Mo's equation was developed by combining Avrami Equation (2) and Ozawa Equation (5) that resulted in Equation (6):

$$ln\ \{-ln[1-X(t)]\} = \ln K(T) - m\ ln\beta \quad (5)$$

$$\log Z_t + n\log t = \log K(T) - m\log\beta \quad (6)$$

By solving $\log\beta$, we get:

$$\log\beta = \frac{1}{m}\log\left[\frac{K(T)}{Z_t}\right] - \frac{n}{m}\log t \quad (7)$$

Let $F(T) = \left[\frac{K(T)}{Z_t}\right]^{1/m}$ and $\alpha = \frac{n}{m}$;

The final equation is transformed to:

$$\log \beta = \log F(T) - \alpha \log t \quad (8)$$

where F (T) is the cooling rate value chosen at a crystallization time when the system has a certain degree of crystallinity and $\alpha$ is the ratio of Avrami exponent and Ozawa exponent. Avrami exponent ($n$) and Ozawa exponent ($m$) hinge on the type of nucleation and growth mechanism.

### 2.6.4 Kissinger Equation

The Kissinger Equation is a mathematical formula used in thermal analysis to determine the activation energy of a reaction. Activation energy is the minimum energy necessary for the reacting species to successfully undergo a particular reaction. The present investigation concerns a particular reaction that entails conveying macromolecular fragments to the surface of crystals within the polymers [71]. The activation energy during a polymer's phase transition is influenced by two factors: the dynamic factor, which pertains to the activation energy (ΔE) required for the transportation of crystalline units across the phase, and the static factor, which pertains to the free energy barrier for nucleation [72]. Kissinger equation is widely used for estimating the activation energy for non-isothermal crystallization studied by DSC, marked as Equation (9).

$$\frac{d\left[ln\left(\frac{\beta}{T_p{}^2}\right)\right]}{d\left(\frac{1}{T_p}\right)} = -\frac{\Delta E}{R} \quad (9)$$

where $\beta$ is the cooling rate (K/min), R is the gas constant and Tp is the peak temperature at its maximum value. Using Equation (9), the Kissinger method can estimate the ΔE from the slope of a straight-line plot ln ($\beta$ /$T_p^2$) versus 1/$T_p$.

### 2.6.5 Friedman Method

From the previous section, Vyazovkin et al. [68] suggested that by elimination of the negative sign from the cooling rate in the Kissinger equation, leads to the generation of ineffective energy values. For melt crystallization, the differential iso-conventional approach of Friedman (1964) and the integral iso-conventional method of Vyazovkin (2001) are applicable. Due to its dependability and simplicity, the Friedman approach will be utilized in this study. Friedman's equation is expressed as follows:

$$\ln\left(\frac{dX_t}{dt}\right)_{X_t} = constant - \frac{\Delta E_{X_t}}{\mathrm{R}T_{X_t}} \quad (10)$$

where $dX_t/dt$ is the instantaneous crystallization rate as a function of time for a given value of the relative crystallinity ($X_t$), R is the universal gas constant (J $mol^{-1}$ $K^{-1}$), and $\Delta E_{Xt}$ is the crystallization activation energy (kJ $mol^{-1}$) that corresponds to crystallization temperature, $T_{Xt}$ at various cooling rates. $-\Delta E_{Xt}/R$ was determined from the slope coefficient plots of ln ($dX_t/dt$) versus $1/T_{Xt}$ and exhibited a straight line.

# 3. MATERIALS AND METHODS

## 3.1 Materials

In this study, polycaprolactone pellets (CAS# 24980-41-4) with a molecular weight of 50,000 estimated by gel permeation chromatology (GPC), were obtained from Scientific Polymer Products Inc. (Ontario, New York). Acetone with a molecular weight of 50.08 g/mol was obtained from Fisher Healthcare. Magnesium Oxide ( size < 50 nm ) (CAS# 1309-48-4) with a molecular weight of 40.3 g/mol was obtained from Sigma Aldrich.

## 3.2 Sample Preparation

The electrospun nanofibers were prepared as described in the previous research [58]. The concentration of Poly (ε-caprolactone) in the solution was 10 wt.% and 5 wt.% MgO was incorporated in PCL solution to fabricate MgO-PCL nanofiber composites. The drum collector was spun using a direct current (DC) motor. By applying a high voltage (10 kV) generated by the Gamma High Voltage power source, the syringe needle was electrically energized. This electrically charged syringe needle was positioned above a drum collector to capture the PCL-aligned fiber stream. The distance between the needle and drum collector was approximately 5 cm. The feeding rate of the PCL solution was adjusted to a rate of 0.025 mL/minute. PCL cloths were directly collected on a drum with a 2-inch diameter. The rotation speed, distance between the needle and drum, and fiber deposition rate onto the drum were optimized. A sterilized sharp razor blade was used to cut the cloth into dimensions 18 cm long and 16 cm wide from the drum to be used for experimentation. The chemical composition and processing conditions are shown in Table 1. Bulk-PCL was prepared using sonication to mix 10 wt.% of Poly (ε-

caprolactone) in Acetone by using sonication. Once blended, PCL solution was dried inside a low heat vacuum oven.

**Table 1.** Chemical compositions of bulk-PCL, PCL and MgO-PCL nanofibers.

| Sample | Chemical compositions | | Voltage | Distance |
|---|---|---|---|---|
| | PCL (wt. %) | MgO (wt. %) | KV | cm |
| PCL | 100 | 0 | 10 | 5 |
| MgO-PCL | 95 | 5 | 10 | 5 |
| Bulk-PCL | 100 | 0 | - | - |

### 3.3 Differential scanning calorimetry

Non-isothermal crystallization kinetic studies were carried out using differential scanning calorimetry (DSC-3) from METTLER TOLEDO. DSC results were evaluated using a Star-E system software from METTLER TOLEDO. The experiments are carried out under a nitrogen atmosphere at a flow rate of 50 mL/min. In order to ensure the accuracy of the results, calibration was performed using high-purity indium. The samples were weighed and placed in standard 40-µL aluminum crucible pans. The experiment was conducted in series running concurrently as shown in Figure 4. The samples were heated from 25℃ to 90℃ at 10 K/min, and held at 90℃ for five minutes to remove any thermal history. Then the samples were cooled at different cooling rates ranging between 0.5 – 5 K/min.

The nanofibers were cut into thin strips along the fiber axis for DSC tests. The small fiber mats were then freely placed on the aluminum pan and the lid was then closed

by gentle mechanical compression. It allowed the most-free relaxation of the polymer chains [63].

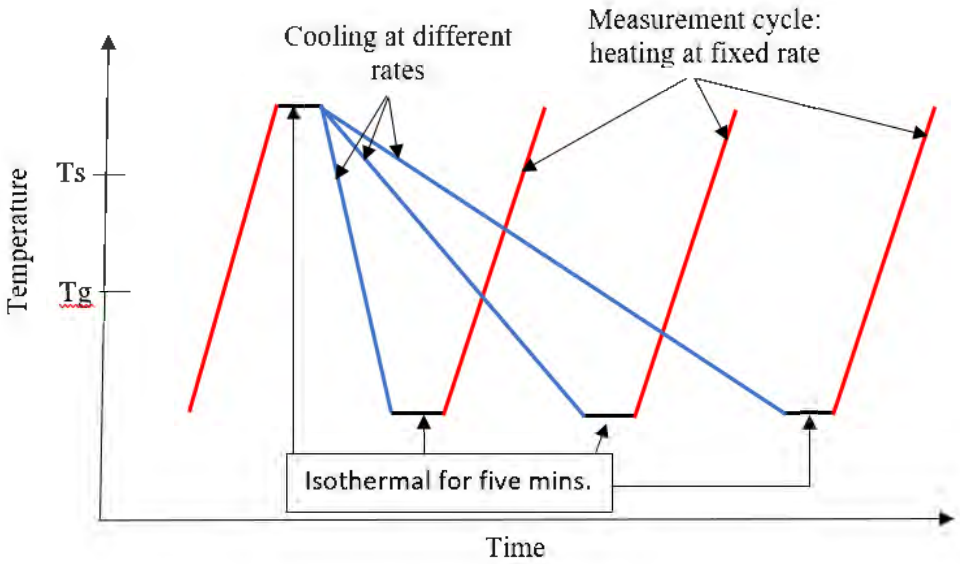


**Figure 4.** Schematic diagram of time-temperature profiles of DSC.

### 3.3.1 PCL solution for Electrospinning

The mass of PCL required to prepare 10 wt.% PCL solution was calculated using. Equation (11). The complete steps for the calculations are shown in Equation (12). The density of acetone is 784 kg/m$^3$ therefore in 100 ml solution we have 78.4 g of acetone. Therefore, to prepare 100 ml of 10 wt.% PCL solution it requires 8.711 g of PCL pellets.

$$10\ wt.\% = \left(\frac{PCL\ (g)}{PCL(g)+Acetone(g)}\right) \times 100 \qquad (11)$$

Simplify and solve for PCL in grams.

$$PCL\ (g) = \left(\frac{Acetone(g)\times 10\ wt.\%}{(100-10)\ wt.\%}\right) = \left(\frac{78.4g\times 10\ wt.\%}{(100-10)\ wt.\%}\right) = \left(\frac{78.4g\times 10}{100-10}\right) = 8.711\ \text{g} \qquad (12)$$

An ultrasonic energy Q55 Sonicator as shown in Figure 5 is used to agitate and blend PCL pellets solute and acetone solvent. The solution is ready to proceed to electrospinning experiment.

**Figure 5.** Q55 Sonicator that agitates PCL pellets in Acetone solvent.

### 3.3.2 Bulk - PCL

Bulk-PCL solution of 10 wt.% was dissolved in 100 ml of acetone. Equation (11) was used to calculate bulk-PCL required in grams. By using a simplified Equation (12), it produced 8.711g of bulk-PCL to be dissolved in 100 ml of acetone. The solution was blended and dried in a Fisher Scientific Isotemp 285 vacuum oven for 24 hours, as shown in Figure 6.

**Figure 6.** Isotemp 285 Vacuum Oven.

### 3.3.3 MgO – PCL

The mass of MgO required to prepare 5 wt.% MgO in 100 ml of acetone was calculated by using Equation (13). The detailed step of the calculation is expressed in Equation (14). From the calculation, 4.13g of MgO was mixed with 100 ml of acetone. An ultrasonic energy Q55 Sonicator as shown in Figure 5, was used to uniformly disperse the nanoparticles in acetone. Finally, 95 ml of 10 wt.% PCL solution was mixed with 5 ml of the 5 wt.% MgO solution by volume. The mixture was agitated using a sonicator to make homogeneous solution before using it for electrospinning.

Acetone = 100 ml or 78.4g

$$5\ wt.\% = \left(\frac{MgO\ (g)}{MgO(g)+Acetone(g)}\right) \times 100 \qquad (13)$$

Simplify and solve for MgO in grams

$$MgO\ (g) = \left[\frac{Acetone(g)\times 5\ wt.\%}{(100-5)\ wt.\%}\right] = \left[\frac{(78.4g\times 5)\ wt.\%}{(100-5)\ wt.\%}\right] = \left[\frac{78.4g\times 5}{100-5}\right] = 4.13g \qquad (14)$$

### 3.4 Characterization

Bulk-PCL, PCL and MgO-PCL nanofibers were characterized by using DSC, XRD, FTIR, SEM and contact angle measurement.

#### 3.4.1 Differential Scanning Calorimeter (DSC)

A differential scanning calorimeter (DSC-3) from METTLER TOLEDO as shown in Figure 7, was used to investigate how heat flow occurred in bulk-PCL, PCL and MgO-PCL nanofibers when they are heated and rapidly cooled. DSC is integrated with Mettler Toledo STAR$^{e}$ software that helps in evaluating and interpreting DSC curves. DSC temperature is calibrated by using pure zinc or indium. Once the measurement results are complete, they are compared to the manufacturer's value [73, 74] as shown in Table 2. It shows that our measured data are within the reference error limits of the accuracy and reliability of the equipment.

**Table 2.** DSC calibration measurements references.

| Reference | Literature Value [ºC] | Measured Value [ºC] | Error Limits [ºC] |
|---|---|---|---|
| Indium | 156.6 | 156.3 | $\pm$0.3 |
| Zinc | 419.5 | 419.07 | $\pm$0.7 |

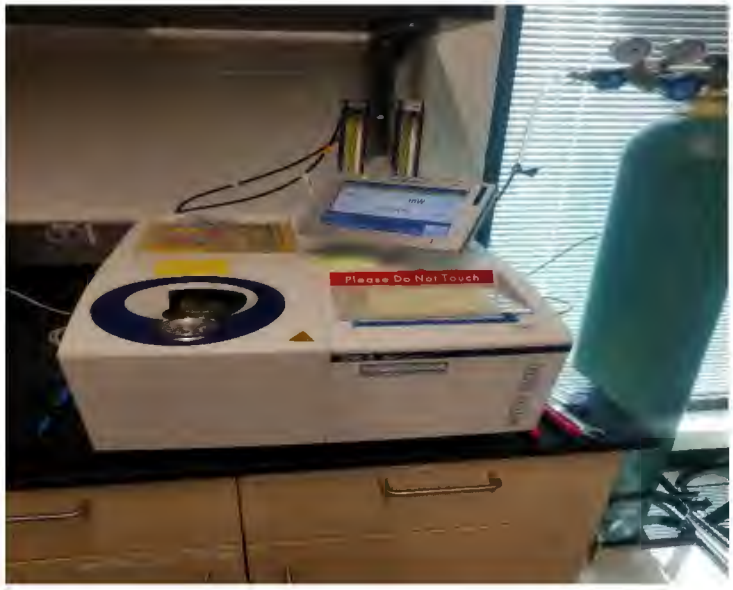


**Figure 7.** DSC equipment (left) and purge gas cylinder (right).

DSC measurements are carried out by using a sample and a reference standard 40 micro-liter aluminum crucibles. Below are the steps for preparing the samples for the DSC experiments.

- Cut small pieces of nanofibers and place them inside the crucible. Put a cover on the crucible and seal it with a crucible sealing press, see Figure 8a. The sample weight inside the crucible must not exceed 10 mg.
- For a reference crucible, an empty crucible is sealed with a crucible sealing press.
- Both crucibles are weighed with a microbalance Figure 8b and placed on their appropriate DSC sensors.

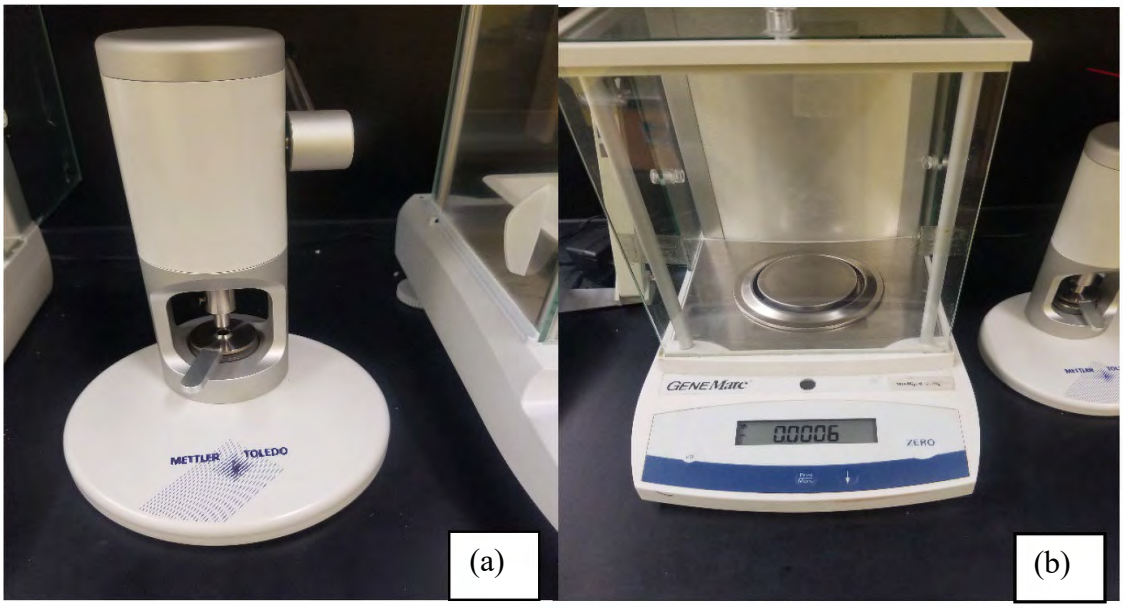


**Figure 8.** Crucible sealing press (left) and micro balance (right).

The DSC measurements were performed by purging the DSC measuring cell. Nitrogen gas at 20 mL/min was used to protect the measuring cell while Oxygen at 50mL/min was used for heating process, see Figure 9. The following section will describe the non-isothermal temperature profiles performed on DSC.

**Figure 9.** Oxygen gas cylinder (left) and Nitrogen purge gas cylinder (right).

#### 3.4.1.1 Non-Isothermal Crystallization

DSC experiments were performed to investigate the non-isothermal crystallization of bulk-PCL, PCL, and MgO-PCL nanofibers. Below are the steps used to investigate the time-temperature profile by using DSC:

1) Samples were heated from 25 to 90 ℃ at a heating rate of 10 K/min and held at a constant 90 ℃ to remove their thermal history. Samples were then cooled back to their amorphous state at 25 ℃.
2) For non-isothermal experiments only, step 1 was repeated but using constant cooling rates of 0.5, 0.8, 1, 2, 3, 4, and 5 K/min. A total of seven runs were performed as one experiment in addition to step 1 was voided.
3) Repeated steps 1 and 2 twice to have total of three separate experiments with new samples.
4) DSC curve results are shown in Figure10 and are available in DSC STAR$^e$ software ready to be analyzed and evaluated.

DSC curves are only plotted with respect to sample temperature in non-isothermal crystallization. By using STARe software in thermal analysis, the most common evaluations (see Figure 11) can be determined:

- $T_o$ – The temperature is determined by extrapolating the baseline from the point of intersection before the thermal effect.
- $T_{endset}$ - The temperature is determined by extrapolating the baseline from the point of intersection after the thermal effect.
- $T_p$ – The measurement value at the extreme point of the peak.

- Normalized value – Also known as sample Enthalpy (J/g).

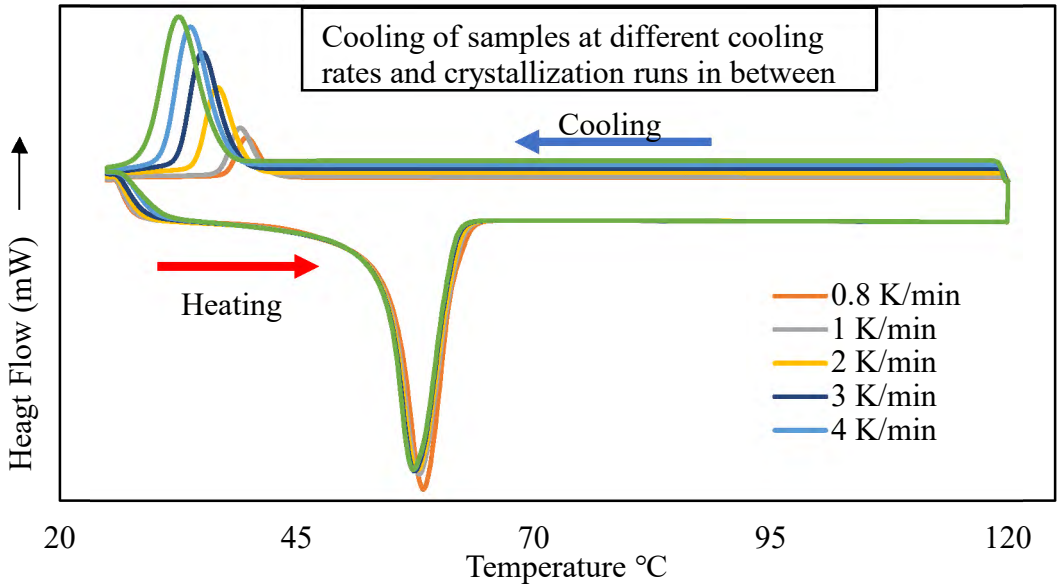


**Figure 10.** Example of non-isothermal crystallization DSC cooling curves with respect to sample temperature.

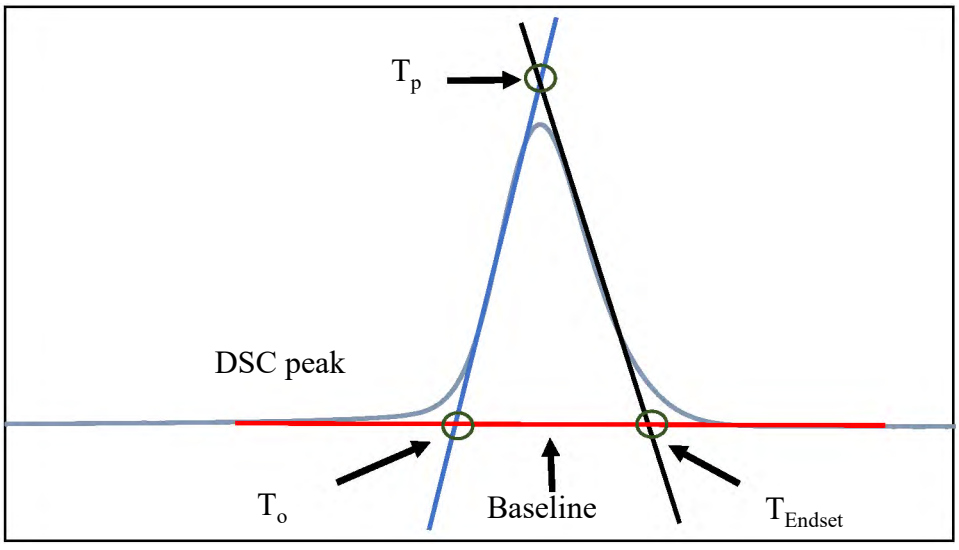


**Figure 11.** DSC peak characteristics points of onset, peak and endset temperatures.

### 3.4.1.2 Crystallinity

The DSC curves were analyzed to obtain heat of crystallization. Bulk-PCL, PCL, and MgO-PCL nanofiber's degree of crystallinity were evaluated. Equation (15) was used

to calculate individual crystallinities, while Equation (16) was used to calculate the crystallinity of the blends.

$$X_c(\%) = \frac{samples\ of\ heat\ of\ \text{Crystallization}\ \left({}^{j}/_{g}\right)}{heat\ of\ \text{Crystyllization}\ \left({}^{j}/_{g}\right)} = \frac{\Delta H_c}{\Delta H_c^{\circ}} \times 100 \quad (15)$$

$$X_c(\%) = \frac{\Delta H_c}{(1-\Psi)\Delta H_c^{\circ}} \times 100 \quad (16)$$

where $\Delta H_c$ is the enthalpy of crystallization, $\Delta H_c^{\circ}$ is the theoretical enthalpy of crystallization of 100% crystalline PCL polymer of which is 139 J/g [75] and Ψ is the weight fraction of the polymer. The enthalpy of crystallization units is shown below:

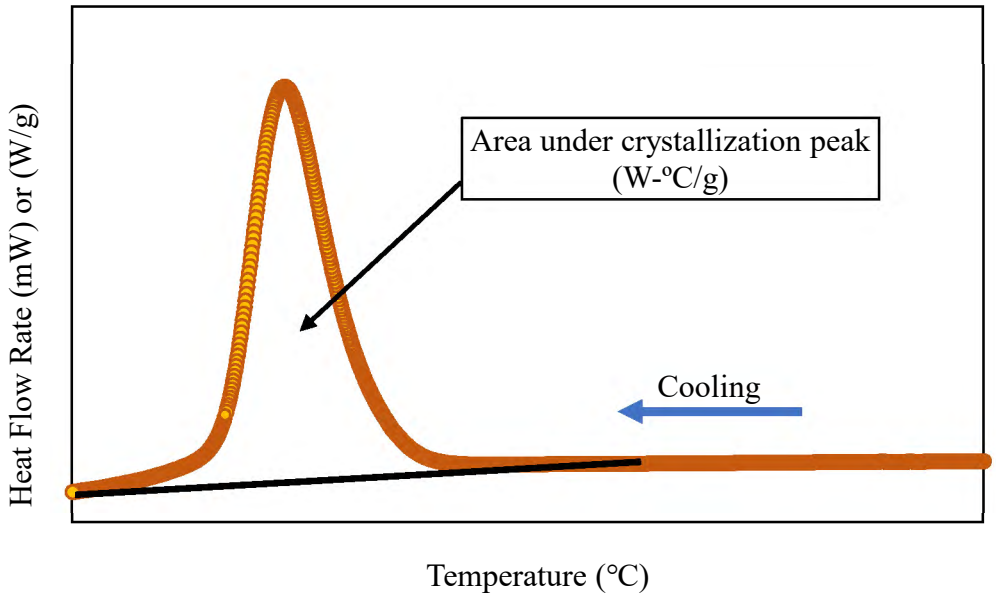


**Figure 12.** Schematic diagram on how area under the curve is calculated.

$$\Delta H_c = \frac{Area\ under\ crystallization\ peak\ (W-{}^{\circ}C/g)}{Cooling\ rate\ ({}^{\circ}C/s)} = \frac{\frac{W}{g}\times {}^{\circ}C}{{}^{\circ}C/S} = \frac{J}{g} \quad (17)$$

where the heat of crystallization ($\Delta H_c$) is calculated by dividing the area under the crystallization peak (product of heat flow rate and temperature) by cooling rate.

### 3.4.2 X-Ray Diffractometer (XRD)

The crystal structure of bulk-PCL, PCL and MgO-PCL nanofibers were examined using a Shimadzu X-Ray Diffractometer (XRD-7000 series) equipped with Cu-$K_\alpha$ radiation ($\lambda = 0.154$ nm). XRD is shown in Figure 12. XRD measurement conditions were set as follows: The Cu X-ray tube voltage was set at 40 kV, current at 30 mA, divergent and scatter slit at 1º, receiving slit at 0.3 mm, and the scanning speed was set at 0.5º/min to ensure a more detailed scan. Fast scan speed is used for quick analysis while a low scan speed is for detailed scan. The scanning range was 10 - 80º, sampling pitch and present time were set at 0.0189º and 2.27 seconds respectively. All three samples were performed at ambient temperature. Once the experiments are complete, crystallinity of the samples are automatically calculated by Shimadzu XRD software. Crystallite average size was calculated by using Scherrer's method as shown in Equation (18). XRD analysis was carried out to compare crystallinity with the DSC results.


**Figure 13.** Shimadzu X-Ray Diffractometer.

$$D_{HKL} = \frac{K \times \lambda}{FWHM \times \cos\theta} \quad (18)$$

where $D_{HKL}$ is the integral width (crystallite size), K is Scherrer's constant (1.05), λ is the wavelength of the X-ray (λ = 0.154 nm), FWHM is the angle measuring full width at half maximum of peaks and θ is the Bragg angle.

### 3.4.3 Fourier Transform Infrared (FTIR-ATR) Spectroscopy

The functional groups present in the samples were analyzed by using Fourier transform infrared spectroscopy (FTIR-ATR model: Agilent Cary 630 FTIR spectrometer with Diamond ATR accessory) as shown in Figure13. The FTIR uses Agilent MicroLab PC software to assist in analyzing the results. The FTIR spectra were collected from 4000 to 650 $cm^{-1}$ with a resolution of 16 $cm^{-1}$.


**Figure 14.** FTIR model: Agilent Cary 630 FTIR spectrometer with Diamond ATR.

### 3.4.4 Scanning Electron Microscopy (SEM)

Morphological characterization of the nanofibers was observed using a JEOL EDS scanning electron microscope (model JSM-6010LA). The electrospun nanofibers were first removed from the collector and then cut to prepare the test samples. The samples were observed at an accelerating voltage of 10 KV.

### 3.4.4 Contact Angle

The wettability and hydrophobic/hydrophilic were evaluated by Contact Angle Meter (model: Cam-Plus Micro/Film) on the sample's surfaces, see Figure 14. Figure 15 shows the contact angle which is between the sample's smooth surface and the tangent line where it contacts the distilled water droplet (substrate). A suspended syringe filled with distilled water is used to dispense droplets on the tested surface. The contact angle meter produces a beam across the projection lens, through an inversion prism and dispensed droplet image is projected on a circular angle measured screen (in degrees) at the end of the platform.

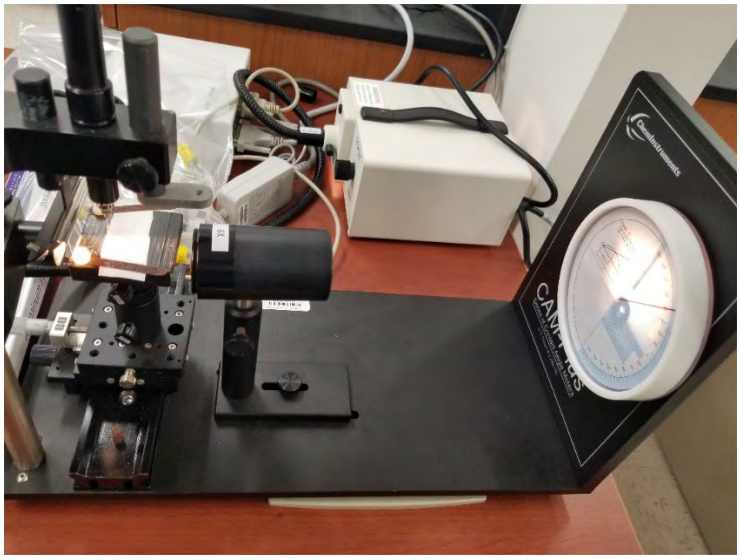

**Figure 15.** Contact Angle Meter (model: Cam-Plus Micro/Film).


**Figure 16.** Contact angle formed by dropping a liquid on a smooth flat surface.

# 4. CHARACTERIZATION OF NANOFIBERS

Crystallinity is a characteristic of a structure that influences surface properties for drug loading, and release kinetics. Therefore, understanding the crystallization mechanism of nanofibers is crucial for tailoring scaffolds for biomedical applications. In this chapter, we have characterized bulk-PCL, PCL and MgO-PCL nanofibers by using different characterization instruments such as DSC, XRD, FTIR, SEM, and contact angle meter. The results are discussed below.

## 4.1 Differential Scanning Calorimeter (DSC)

The cooling cycles of DSC curves for bulk-PCL, PCL and MgO-PCL nanofibers at different cooling rates are shown in Figures 16-18. It shows a distinct exothermic peak attributed to the crystallization temperatures as a function of cooling rates. Additional experiments were carried out at a higher cooling rate of 10-30 K/min; however, no crystallization peaks were observed. The onset temperature ($T_o$) denotes the initial temperature at which the crystallization process commences, while $T_c$ signifies the temperature at which the maximum of the crystallization peak can be ascertained. Similar to other researchers [60, 61, 76], a shift toward higher crystallization temperature was noted with a decreased cooling rate. The data suggest that an increase in cooling rates results in a reduction of the crystallization temperature. In brief, it has been observed that an increase in the cooling rate results in a corresponding increase in the degree of supercooling. According to Wang et al. [77], an increase in the cooling rate resulted in a leftward shift of the heat flow curves of crystallization.

Table 3 summarized the onset and crystallization temperature of the bulk-PCL sample, PCL, and MgO-PCL nanofibers. The result shows that the nuclei will easily

develop and the crystallization process would start at a lower temperature. Likewise, Xu et al. [78] also reported that at high cooling rates, the crystallization time allowed for the crystalline entities to develop is reduced, and the nuclei present within the melted matrix would not be able to develop due to the high motion of the polymer molecules at these cooling rates. Moreover, it has been suggested that the molecular chains at high cooling rates have less time to diffuse into the crystallite lattice, adjust, and organize their configurations into more perfect crystallites [79]. The intensity of that motion at such cooling rates could be reduced if the temperature of the exposed material is decreased.

The date represented in Table 4 showed that crystallization temperature of PCL nanofiber (37.54 ℃ ± 0.22) at a cooling rate of 0.5 k/min is lower compared to the crystallization temperature of MgO-PCL (41.17 ℃ ± 0.37) at the same cooling rate. This was attributed to the nucleating ability of the MgO nanoparticle incorporated fibers that ease the crystallization process of the polymer matrix, basically at the interface area between MgO-PCL of the composite materials [61, 80]. As a result, such a process should occur at earlier temperatures, increasing both $T_c$ and $T_o$. Equation (16) reported in literature review was used to calculate the crystallinities of the blends, and the results are tabulated in Table 4. The data shows the average degree of crystallinity of MgO-PCL (56 ± 0.001%) is much higher compared to the PCL nanofiber (40 ± 0.012%) performed by DSC equipment. In addition, the relative crystallinity of bulk-PCL is 60% at a cooling rate of 2 K/min. In the next section, crystallinity was also measured with XRD, and the results are compared with DSC results as shown in Table 4.

The higher crystallization of MgO-PCL nanofibers compared to PCL nanofibers can be explained as follows: pure polymer contains a minor volume of impurities in the

form of unreacted monomers, and these impurities are randomly dispersed throughout the domains of the amorphous polymer matrix. Therefore, impurity-free domains will crystallize via homogenous crystallization, necessitating a considerably lower nucleation temperature. In contrast, PCL nanofibers containing MgO crystallize heterogeneously at relatively higher temperatures. Similar consequences were observed for PEO encapsulated in PS nanofibers with a glassy surface [67].

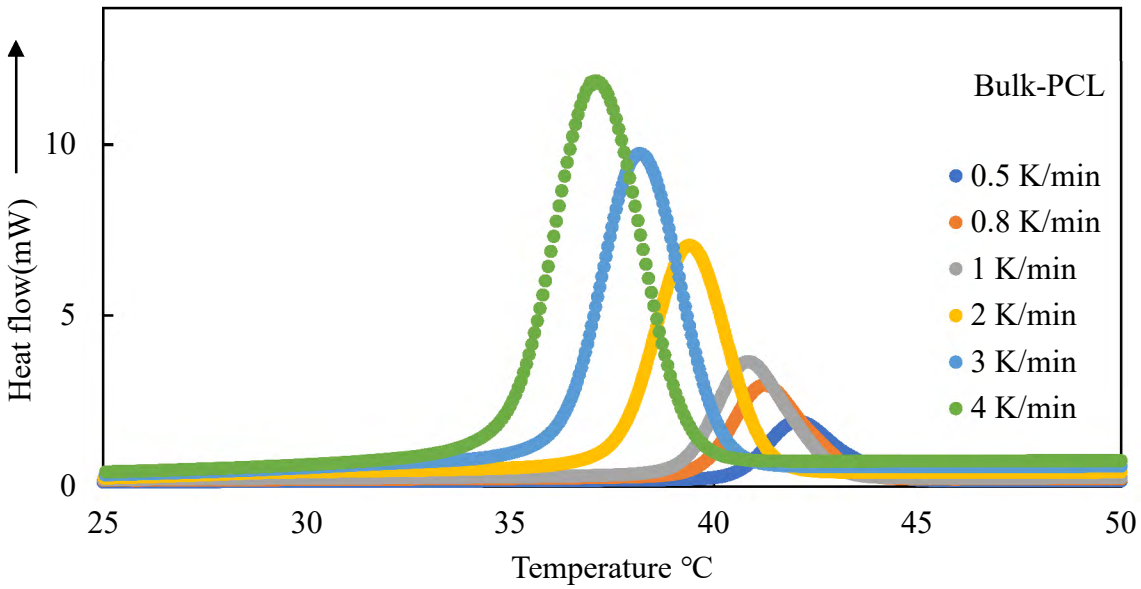


**Figure 17.** Non-isothermal crystallization exotherms of bulk-PCL measured at various cooling rates between 0.5 and 4 K/min.

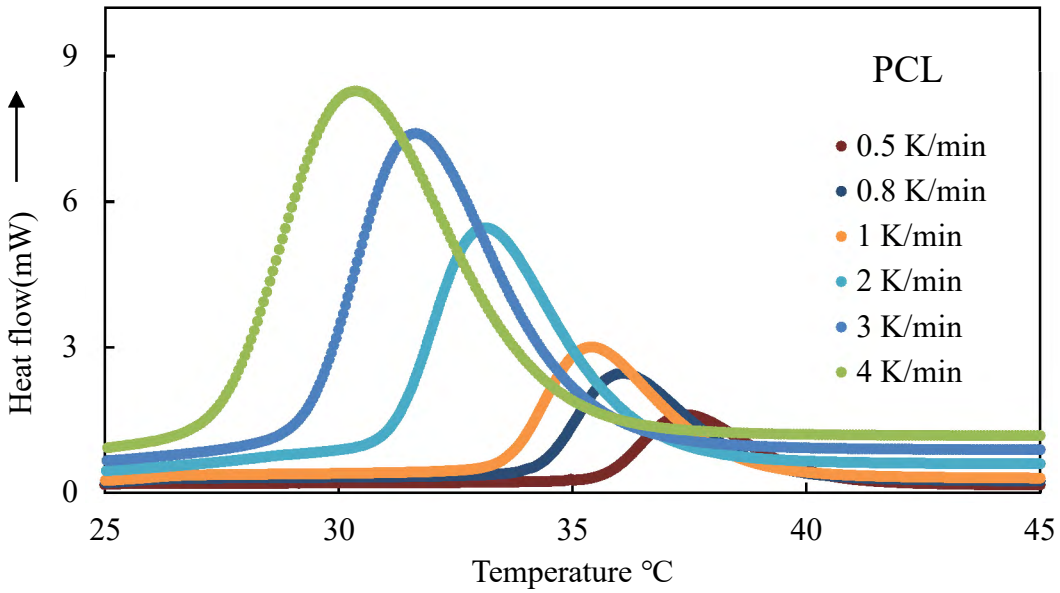


**Figure 18.** Non-isothermal crystallization exotherms of PCL nanofibers measured at various cooling rates between 0.5 and 4 K/min.

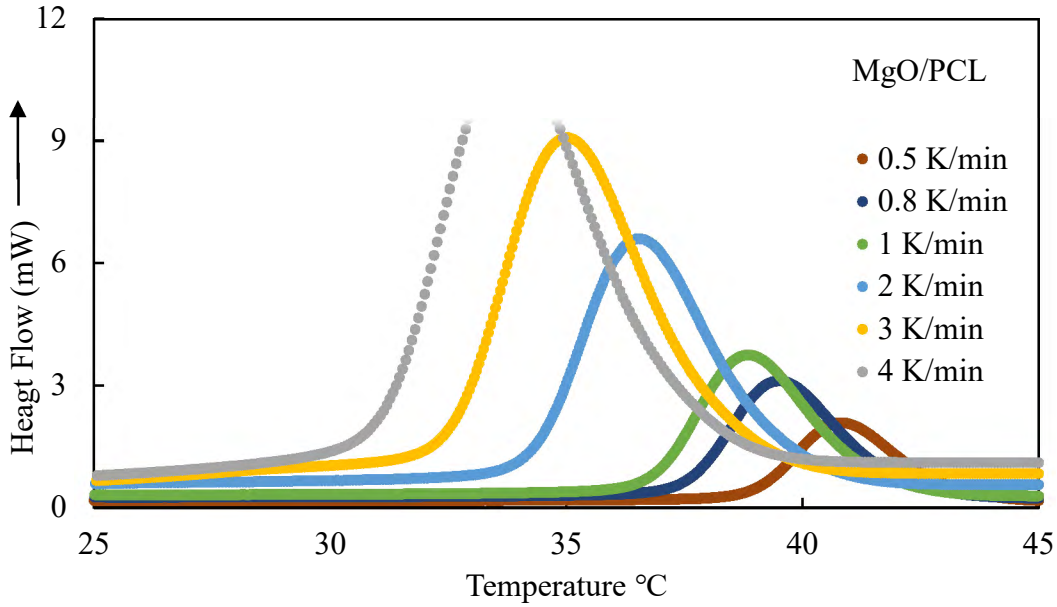


**Figure 19**. Non-isothermal crystallization exotherms of MgO-PCL nanofibers measured at various cooling rates between 0.5 and 4 K/min.

**Table 3.** Onset and crystallization temperature of bulk-PCL sample, PCL and MgO-PCL nanofibers.

| | $T_C$ (°C) | | | $T_o$ (°C) | | |
|---|---|---|---|---|---|---|
| β (k/min) | PCL | MgO-PCL | Bulk-PCL | PCL | MgO-PCL | Bulk-PCL |
| 0.5 | 37.54 ± 0.22 | 41.17 ± 0.4 | 42.00 ± 0.14 | 40.25 ± .04 | 43.49 ± 0.4 | 43.93 ± 0.8 |
| 0.8 | 36.21 ± 0.14 | 39.82 ± 0.24 | 41.16 ± 0.2 | 39.14 ± 0.3 | 42.30 ± 0.3 | 43.07 ±0.1 |
| 1 | 35.54 ± 0.14 | 39.16 ± 0.2 | 40.75 ± 0.25 | 38.54 ± 0.23 | 41.73 ± 0.26 | 42.69 ± 0.16 |
| 2 | 33.28 ± 0.1 | 36.82 ± 0.1 | 39.31 ± 0.3 | 36.62 ± 0.24 | 39.59 ± 0.16 | 41.20 ± 0.02 |
| 3 | 31.75 ± 0.1 | 35.30 ± 0.1 | 38.22 ± 0.2 | 35.47 ± 0.3 | 38.50 ± 0.2 | 40.18 ±0.1 |
| 4 | 29.84 ± 0.6 | 34.01 ± 0.06 | 37.29 ± 0.15 | 34.28 ± 0.2 | 37.58 ± 0.2 | 39.37 ± 0.1 |

## 4.2 X-Ray Diffractometer (XRD)

The crystal lattice of bulk-PCL, PCL, and MgO-PCL nanofiber composite materials were investigated by using XRD. The XRD patterns are shown in Figure 19. The Figure shows Bulk-PCL, PCL, and MgO-PCL nanofiber have (110) and (200) diffraction peaks at 21.4$^o$ and 23.8$^o$ respectively which are associated with the well-known orthorhombic crystal lattice of PCL [81]. Comparably, Rijal et al. [29] performed an XRD analysis of PCL/MgO nanofibers and found two strong peaks (21.5 $^o$ and 23.6 $^o$) that are similar to our experimental results. Abdelrazek et al. [82] also had similar XRD results. A full XRD scan from 10° - 80° is provided in Appendix C. Reduction in the corresponding peak intensities and peak broadening were also observed in composite nanofibers compared to pristine PCL. From XRD results, crystallized sizes were calculated for PCL and MgO-PCL nanofibers using Equation (18) to be 20 and 23 nm respectively. The crystallinity obtained from XRD using 'Basic Process' application

window, is tabulated in Table 4, and the result shows that both DSC and XRD give similar values.

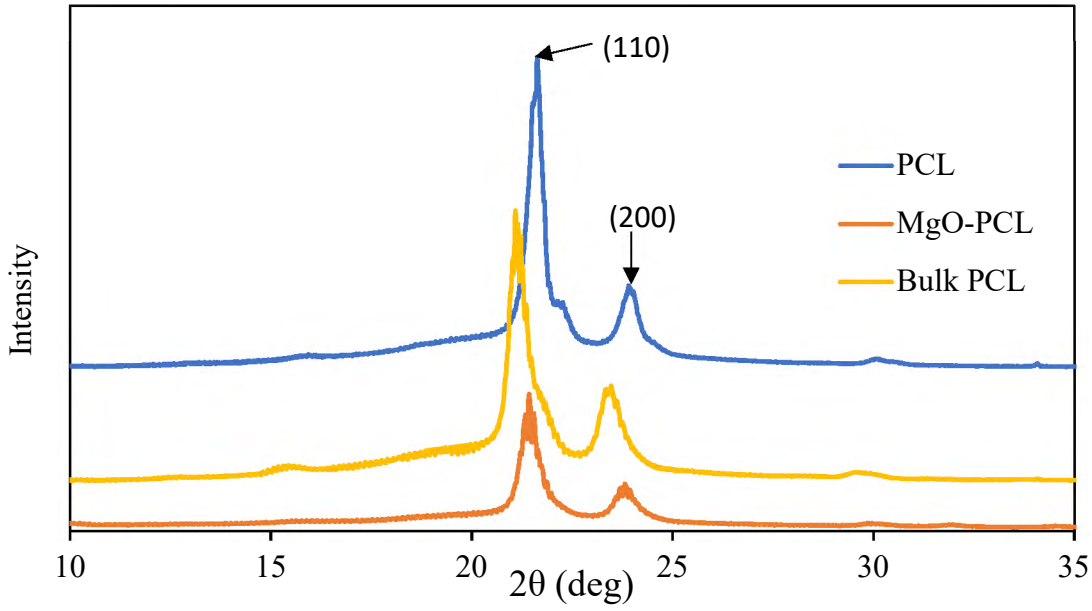


**Figure 20**. X-ray diffraction patterns of bulk-PCL, PCL and MgO-PCL nanofibers.

**Table 4.** Crystallization summary of bulk-PCL, PCL, and MgO-PCL nanofibers.

| Sample | Peak position (2 Theta) | FWHM (deg) | Crystallite Size D (nm) | Crystallinity (X%) XRD | Crystallinity (X%) DSC |
|---|---|---|---|---|---|
| MgO-PCL | 21.63 | 0.407 | 23.17 | 56.37±1.7 | 56±0.01 |
| PCL | 21.47 | 0.4705 | 20.05 | 46.73±4.0 | 40±0.01 |
| Bulk-PCL | 21.19 | 0.4915 | 19.18 | 64.52±0.1 | 60±0.01 |

### 4.4 Fourier Transform Infrared (FTIR) Spectroscopy

The FTIR characterization was performed using Agilent Cary 630 FTIR spectrometer with a Diamond ATR accessory, and the results of PCL and MgO-PCL nanofibers are shown in Figure 20 and Table 5. The absorbance intensities of the two

spectra were almost identical, which suggests that the infrared beam encountered almost the same number of characteristics. The characteristics peaks were located at: 1724 $cm^{-1}$ for C=O stretching vibrations; 1470 $cm^{-1}$, 1395 $cm^{-1}$ and 1365 $cm^{-1}$ for $CH_2$ bending vibrations; 2940 $cm^{-1}$ and 2865 $cm^{-1}$ for stretching vibrations; 1238 $cm^{-1}$, 1104 $cm^{-1}$and 1044 $cm^{-1}$ for C-O-C stretching vibrations; 1165 $cm^{-1}$ for C-O stretching vibrations and 1290 $cm^{-1}$ for C-C for stretching vibrations. This is because when most molecular chains are oriented in a specific direction the infrared beam encounter a large number of C-O-C, C-O, and C-C bond as a result, higher absorbance intensities are observed. From the results, the compound appears to be saturated because of no visible C=C stretch, and no unsaturated C-H absorption above 3000$cm^{-1}$. Similar to the vibration wave number reported by Abdelrazek et al. [82] we also observed higher absorbance intensities for PCL nanofibers compared to MgO-PCL nanofiber which suggests that the molecular chains are oriented along the axis of PCL nanofibers.

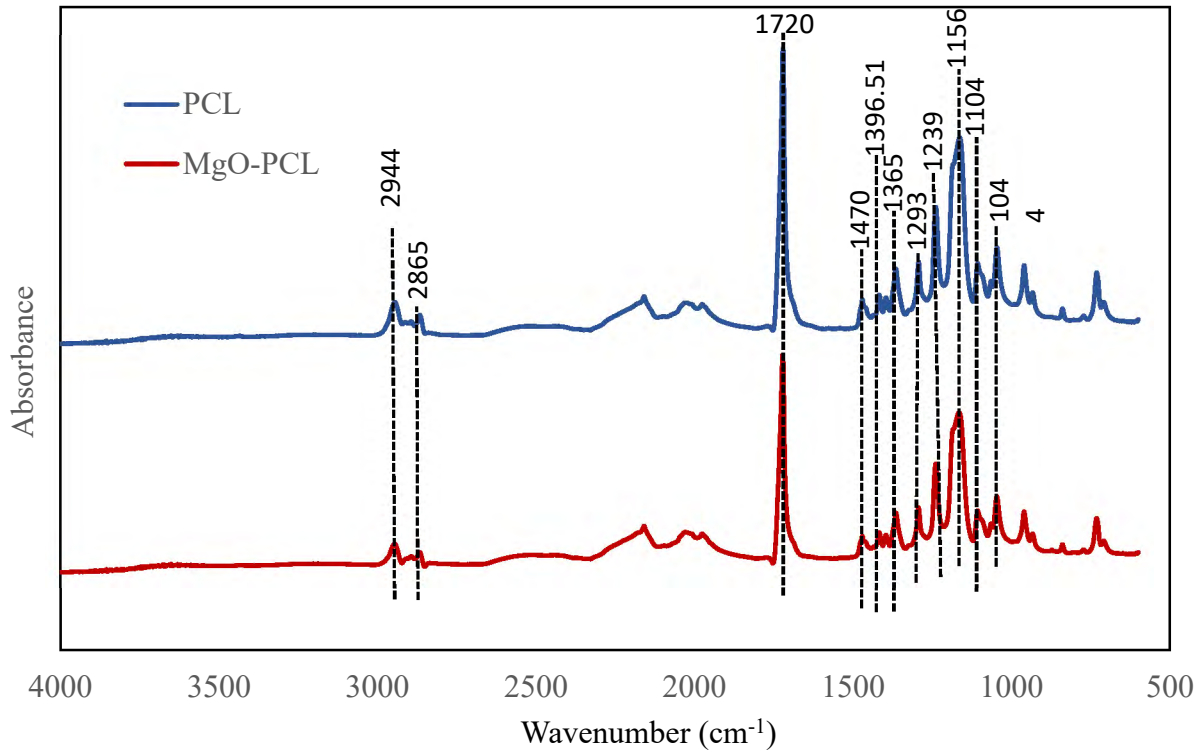


**Figure 21**. FTIR result of PCL and MgO-PCL nanofiber composite.

**Table 5.** Vibrations and wave numbers displayed by PCL nanofibers.

| Description of vibrations | Wavenumber ($cm^{-1}$) | Reference |
|---|---|---|
| $CH_2$ stretching | 2940, 2865 | [83] |
| C=O stretching | 1724 | [83] |
| $CH_2$ bending | 1470, 1395, 1365 | [83] |
| C-C stretching | 1290 | [83] |
| C-O-C stretching | 1238, 1104, 1044 | [83] |
| C-O stretching | 1156 | [83] |

## 4.5 Scanning Electron Microscopy (SEM)

In Figure 21, PCL nanofibers are depicted as SEM images. The images depict non-aligned electrospun nanofibers. According to the SEM findings, scaffolds have high porosity and interconnectivity. These scaffold characteristics provide ample surface area for cell adhesion. In this work, we did not calculate the size of the nanofibers or the porosities of the scaffold. However, Morshed et al. [58] did an SEM analysis and reported that the fiber diameter is approximately 300nm. Additionally, Sajeev et al. [84] reported the average porosities of PCL samples ranged from 10-20 microns. Figure 21b shows the SEM images of PCL nanofibers containing MgO. Nanofibers containing MgO exhibited a rigid structure with a homogeneous and smooth surface. However, the presence of the nanofibers was not clearly visible, therefore, to obtain a clearer image of the MgO -PCL nanofibers, more SEM images must be acquired. As morphology is not within the ambit of our work, we did not capture additional images.

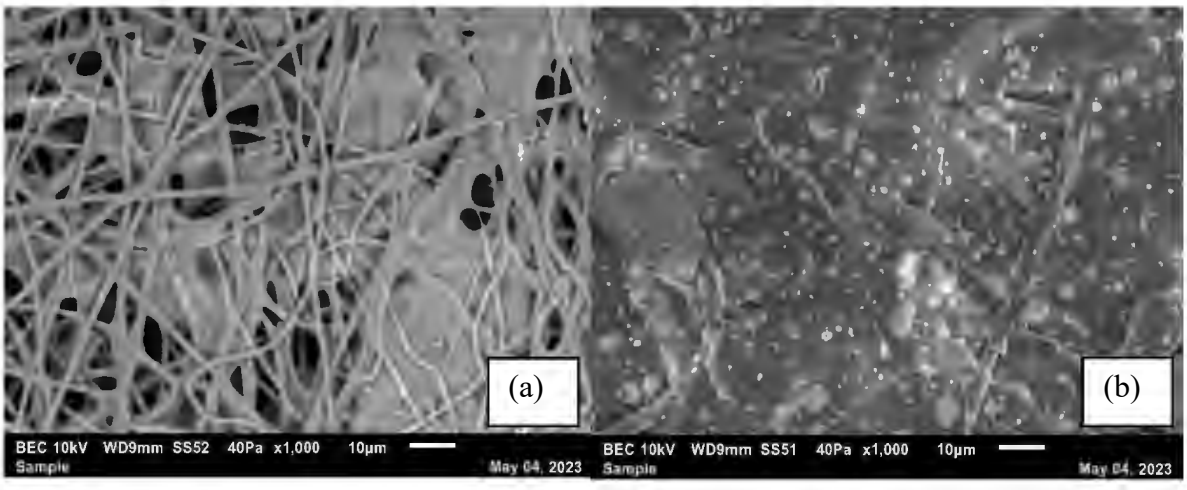


**Figure 22.** SEM images of electrospun nanofiber of a) poly(ε-caprolactone) (PCL) and b) MgO incorporated PCL.

## 4.4 Contact Angle

The contact angle meter is used to measure the contact angle (θ) that characterizes its surface wettability for PCL and MgO-PCL nanofibers by using distilled water. The contact angle for PCL and MgO-PCL nanofibers are 83.5 º ± 0.5, and 106 º ± 0.5. If the contact angle is $\theta \geq 90°$, it's said to have non-wetting conditions, and its surface is hydrophobic. However, if it's $0° < \theta < 90°$, it's said to have wetting conditions, and the surface is hydrophilic. The results show that both fibers are hydrophobic, and incorporating magnesium into the PCL nanofiber increases its hydrophobicity. Tan et al. [85] measured the water contact angle non-NaOH treated PCL membranes were measured to be 82.5 º ± 1.0, which is similar to the PCL contact angle of 83.5 º ± 0.5. Also, by adding MgO nanoparticles to the scaffold, MgO-PCL nanofiber's hydrophobicity increased by 27%.

## 4.5 Conclusion

Characterization of PCL, MgO-PCL nanofibers were performed by using DSC, XRD, FTIR, and contact angle measurement. From the DSC cooling curves, crystallization temperature shifted to the right as the cooling rate decreases, and thus required a higher supercooling degree. MgO-PCL nanofiber had a higher crystallization temperature due to the nucleating ability of the MgO nanoparticle incorporated fibers that ease the crystallization process. XRD results showed the bulk-PCL has the highest crystallinity followed by MgO-PCL nanofiber then PCL nanofiber. The surface wettability of PCL nanofiber was reduced as MgO was incorporated.

# 5. NON-ISOTHERMAL CRYSTALLIZATION OF ELECTROSPUN POLY (Ɛ-CAPROLACTON) (PCL) AND MGO INCORPORATED PCL NANOFIBERS

Differential Scanning Calorimetry (DSC) is used to precisely examine the non-isothermal crystallization in bulk-PCL, PCL, and MgO-PCL nanofibers. DSC results were evaluated using STARe software from METTLER TOLEDO. Due to the complexity of the non-isothermal crystallization method, various modified Avrami models [39, 86, 87], such as the Jeziorny model [40], Ozawa's model [41], and Lui-Mo's model [40, 88], have been developed to comprehend the process better. In the past, these models were utilized frequently to comprehend bulk polymeric materials' non-isothermal crystallization kinetics behavior [43, 44, 45, 46]. The activation energy of confined polymer in electrospun nanofibers was then calculated using the Kissinger and Friedman method.

## 5.1: Results and Discussions

### 5.1.1: Non-isothermal crystallization

The relative crystallinity as a function of the cooling rate was obtained from the DSC curves shown in chapter 4 (Figures16-18). During the crystallization process at a constant cooling rate (β), the relative degree of crystallization X(t) within the matrix of confined PCL, MgO-PCL nanofiber and bulk-PCL materials after a given crystallization time t, can be determined using the following Equation (19) [89]:

$$X_t = \frac{\int_{T_o}^{T} (dH_c/dT)dT}{(1-\psi)\Delta H_c} \qquad (19)$$

where $dH_c$ is the enthalpy of crystallization during the time interval dT, $T_o$ is the onset temperature, T is arbitrary temperature at time t, ψ is the weight fraction of the polymers, and $\Delta H_c$ is the overall enthalpy of 100% crystalline PCL which is taken as 139 J/g [89]. Such relative crystallization is usually obtained by the integration of the area under the exothermic peak, within the heat flow curves. Moreover, during non-isothermal conditions, the crystallization temperatures can be converted to crystallization time [90], marked as Equation (20):

$$t = |T - T_O|/\beta \tag{20}$$

where $\beta$ is the cooling rate applied for the non-isothermal crystallization. Crystallization kinetics is widely analyzed by the Avrami equation [91, 92]. The overall effect of the cooling rate of bulk-PCL, PCL, and MgO-PCL nanofiber was investigated to determine the overall crystallization time ($t_c$). The following Equation (21) was used to calculate each $t_c$ of the samples:

$$t_c = \frac{T_O - T_{endset}}{\beta} \tag{21}$$

where $T_o$ is the initial crystallization temperature, $T_{endset}$ is the finishing crystallization temperature, and β is the cooling rate considered. As seen from Table 6, demonstrates a significant reduction in crystallization time with an increased cooling rate. The above outcome is expected due to the accelerated cooling rate impeding the development of crystalline structures within the molten matrix, consequently diminishing the duration of the materials' crystallization process. Furthermore, it can be observed from Table 6 that the composite nanofiber exhibits a reduced crystallization time ($t_c$) in comparison to the

pure PCL nanofiber. The acceleration of the crystallization process in MgO-incorporated PCL and the consequent reduction in crystallization time can be attributed to the inclusion of heterogeneities. In comparison to confined PCL and MgO-PCL nanofibers, non-electrospun bulk-PCL exhibits the shortest crystallization time. According to Labet et. al. [93], the bulk-PCL exhibits a relative crystallinity of 60% when subjected to a 2 K/min cooling rate. The level of crystallinity exhibits a reduction in the case of confined nanofibers. The restricted mobility of polymer chains within smaller domains is a probable cause for the hindered development of crystallinity. The following table presents the mean outcomes of three trials.

**Table 6.** Crystallization behavior of bulk-PCL and confined PCL and MgO-PCL nanofibers.

| Samples | Cooling rate (K/min) | $T_o$ (°C) | $T_p$ (°C) | $t_{0.5}$ (min) | Rate $(t_{0.5})^{-1}$ ($min^{-1}$) | Overall $t_c$ (min) | Crystallinity (%) |
|---|---|---|---|---|---|---|---|
| PCL | 0.5 | 40.25 | 37.54 | 15.14 | 0.07 | 9.2 | |
| | 0.8 | 39.14 | 36.21 | 15.05 | 0.07 | 6.15 | |
| | 1 | 38.54 | 35.54 | 10.67 | 0.1 | 5.06 | |
| | 2 | 36.62 | 33.28 | 6.26 | 0.17 | 2.85 | 46 |
| | 3 | 35.47 | 31.75 | 4.46 | 0.23 | 2.46 | |
| | 4 | 34.28 | 29.84 | 2.94 | 0.26 | 1.97 | |
| MgO-PCL | 0.5 | 43.49 | 41.17 | 15.02 | 0.06 | 8.28 | |
| | 0.8 | 42.3 | 39.82 | 10.16 | 0.1 | 5.69 | |
| | 1 | 41.73 | 39.16 | 9.2 | 0.1 | 4.73 | |
| | 2 | 39.59 | 36.82 | 5.01 | 0.18 | 2.62 | 56 |
| | 3 | 38.5 | 35.3 | 4.05 | 0.25 | 1.99 | |
| | 4 | 37.58 | 34.01 | 2.53 | 0.22 | 1.66 | |
| Bulk-PCL | 0.5 | 43.93 | 42 | 7.89 | 0.13 | 7.74 | |
| | 0.8 | 43.07 | 41.16 | 4.76 | 0.21 | 4.83 | |
| | 1 | 42.69 | 40.75 | 3.87 | 0.26 | 3.94 | |
| | 2 | 41.2 | 39.31 | 2.5 | 0.4 | 2.14 | 60 |
| | 3 | 40.18 | 38.22 | 1.49 | 0.67 | 1.55 | |
| | 4 | 39.37 | 37.29 | 0.96 | 1.04 | 1.26 | |

Table 6 also displays the characteristics data for non-isothermal crystallization exotherms of bulk-PCL, PCL, and MgO-PCL nanofibers. $T_p$ represents the temperature at the maximum crystallization rate, $t_{0.5}$ is the crystallization half-time, and $t^{-1}_{0.5}$ is the inverse of the crystallization half-time.

### 5.1.2: Kinetics of non-isothermal crystallization

The relative crystallinity versus crystallization time profiles for bulk-PCL, PCL, and MgO-PCL nanofibers samples at various cooling rates, are depicted in Figures 22-24 Each curve demonstrates a time dependence that follows a sigmoidal pattern. The leftward shift of sigmoid curves was observed with increased cooling rates. This suggests that an increase in the cooling rate reduces the time needed to achieve maximum crystallinity. Consequently, an increase in the cooling rate leads to a decrease in the half-life $t_{0.5}$ values, as evidenced by the DSC curves. In the context of crystallization, the relative degree of crystallization $X_t$ can be ascertained for confined PCL, MgO-PCL nanofiber, and bulk-PCL materials by subjecting them to a constant cooling rate ($\beta$) during the crystallization process and measuring the resulting X(t) after a given crystallization time t. This can be achieved through the application of the following methodology.

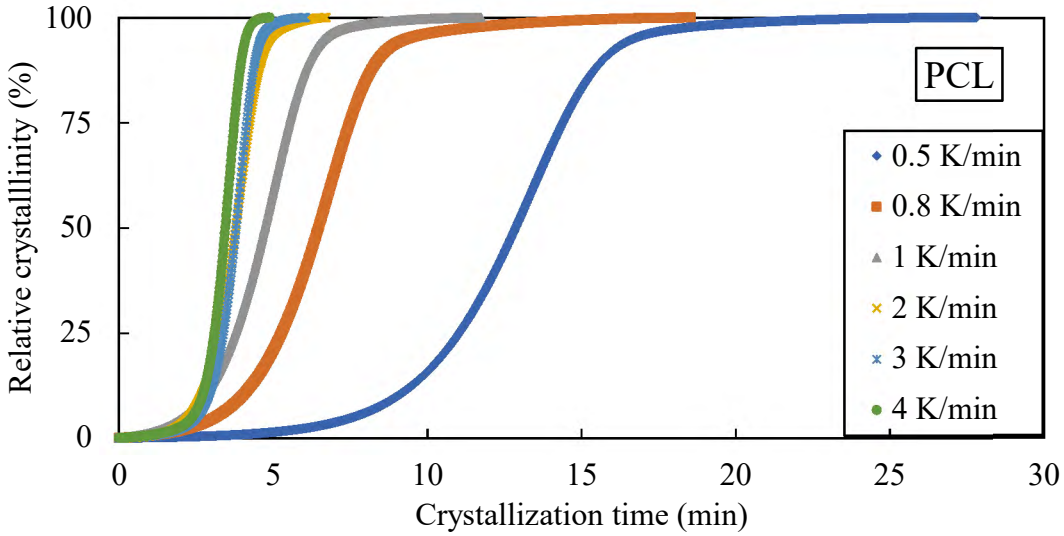


**Figure 23.** Plot of relative crystallinity verses crystallization time for the PCL polymers crystallized non-isothermally at various cooling rates.

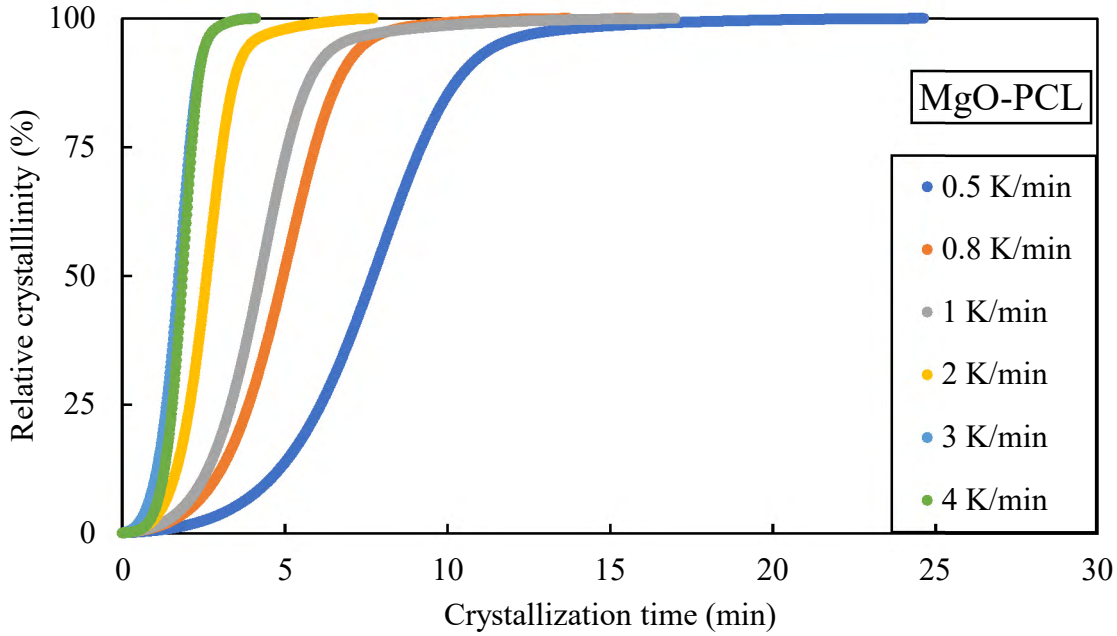


**Figure 24.** Plot of relative crystallinity verses crystallization time for the MgO-PCL polymer crystallized non-isothermally at various cooling rates.

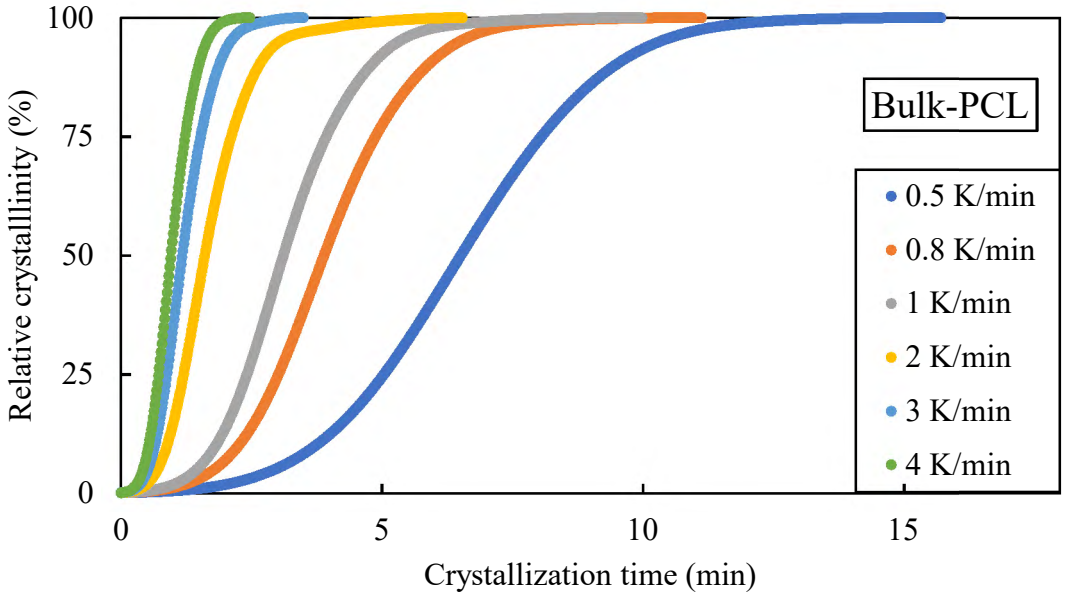


**Figure 25.** Plot of relative crystallinity verses crystallization time for the bulk-PCL non-isothermally at various cooling rates.

The rate of crystallization is defined as the inverse time it takes for crystallization to reach 50% and is expressed as:

$$Rate\ (t_{0.5})^{-1} = {}^{1}/_{t_{0.5}} \qquad (22)$$

Using Crystallization Rate Coefficient (CRC) and Crystallization Rate parameter (CRP), the non-isothermal crystallization rates are compared. CRC categorizes polymers based on their slope. The steeper the slope, the quicker the crystallization rate. A linear fitting is used in CRC plot to determine the slope of a line plotted through cooling rate against peak temperature, $T_p$ for bulk-PCL, PCL, and MgO-PCL nanofibers. The steeper the slope, the quicker the crystallization rate. CRP also utilized linear fitting slope to determine the slope of a line plotted through inverse of half-time against cooling rate for bulk-PCL, PCL, and MgO-PCL nanofibers. The higher the slope, the faster the crystallization rate. CRP parameter determines the relative position of the crystallization rate. Figure 25 demonstrates using the CRC ranking system, that bulk has a steeper slope

than nanofibers. Comparing the crystallization rate of nanofibers and bulk-PCL reveals that nanoconfinement decreases the crystallization rate, as shown in Figures 25-26:

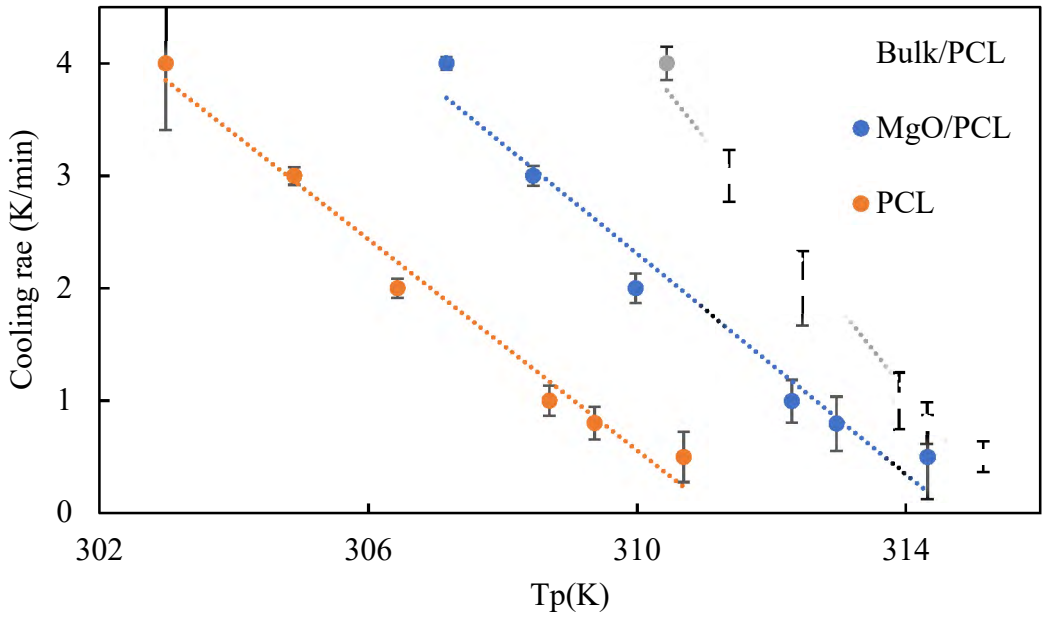


**Figure 26.** Plot of cooling rate as a function of the temperature at the maximum crystallization rate (CRC). Error bars represent standard deviation from 3 measurements on each sample.

The error bars were calculated from the averages of three different experiment runs (see Appendix A) on each sample. The use of error bars gave confidence of data within a defined range.

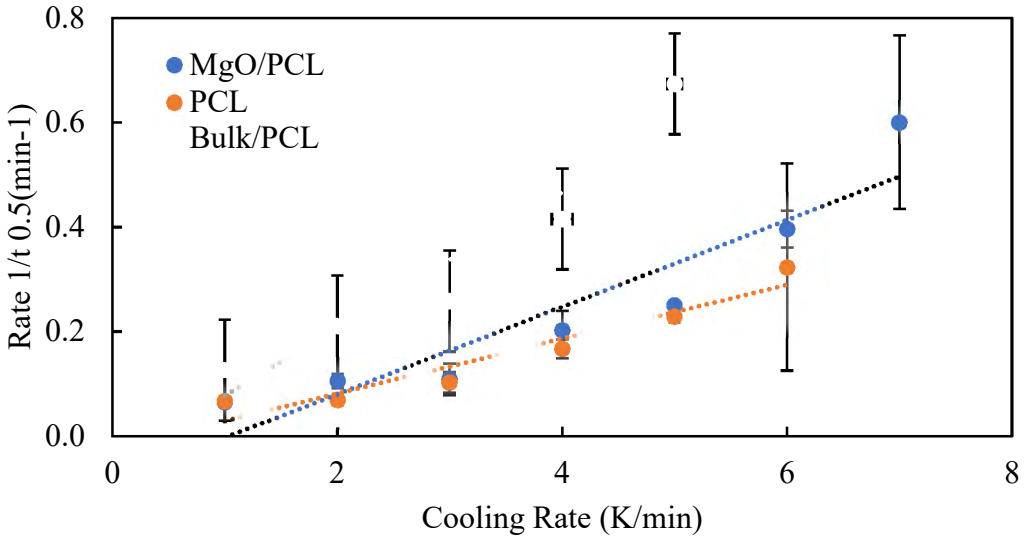


**Figure 27** Plot of reciprocal half-time of crystallization as a function of the heating rate of the bulk-PCL, PCL and MgO-PCL nanofibers (CRP). Error bars represent standard deviation from 3 measurements on each sample.

Table. 6 shows that the peak temperature $T_p$ (°C) and half-time of non-isothermal crystallization $t_{0.5}$ (min) are reducing with the increase of the cooling rate. The decrease of $t_{0.5}$ values indicates that the samples crystallize faster as the cooling rate is reduced. The $t^{-1}_{0.5}$ values are found to increase as the cooling rate increases. This indicates that the higher the cooling rate, the faster the crystallization rate.

### 5.1.3: Non-isothermal mathematical modeling

Several mathematical models have been developed to describe non-isothermal mathematical modeling. Such as; Jeziorny-modified Avrami equation, Ozawa equation, Case Average Avrami exponent, Chuah Average Avrami exponent, and Combined Avrami/Ozawa Equation and Kissinger activation energy.

#### 5.1.3.1: Jeziorny Modified Avrami equation

A widely used Avrami model [66] for describing isothermal crystallization kinetics for polymers as shown in Equation (23), is formulated as:

$$1 - X(t) = exp\ (-Z_t t^n) \quad (23)$$

where $Z_t$ is the Avrami crystallization rate constant and *n* is the Avrami exponent. $Z_t$ and *n* parameters can be calculated by transforming Equation (23) into a traditional linear form Equation (24):

$$log\ \{-ln[1 - X(t)]\} = \text{n log t} + \log Z_t \quad (24)$$

where a linear relationship can be seen when plotted $log\ \{-ln[1 - X(t)]\}$ vs *log t*.

Jeziorny model assumes that the crystallization temperature is constant and modifies Avrami parameters to analyze non-isothermal crystallization kinetics for polymers by assuming that the cooling rate is constant. The corrected crystallization rate constant is shown below:

$$\log Z_c = \log Z_t/\beta \quad (25)$$

where $Z_C$ parameter can describe the non-isothermal crystallization kinetics for polymers and β is the cooling rate. Jeziorny parameters $Z_c$, $Z_t$ and Avrami exponent, *n* can be determined by plotting $log\ \{-ln[1 - X(t)]\}$ against *log t* using the following Equation 24-25. The *n* and *t* values were determined from the slope and intercept of the linear plots.

Jeziorny's corresponding plots of bulk-PCL, PCL, and MgO-PCL nanofibers are shown in Figures 27-29. The result shows a good linear relationship for all samples for the primary crystallization stage, therefore Jeziorny method is applicable. The linear part was used to calculate n, $Z_t$, and $Z_c$ values which are listed in Table 7. Pearson's correlation coefficient $R^2$ for all samples are close to 1 and it supports the linearity of the

plots. The n values varied from 1.2 to 1.4 for bulk-PCL, PCL, and MgO-PCL nanofibers at different cooling rates. The n values indicate a one-dimensional growth phenomenon [94]. On average, $Z_t$ values increased with an increase in the cooling rate. This shows their symbiotic dependency.

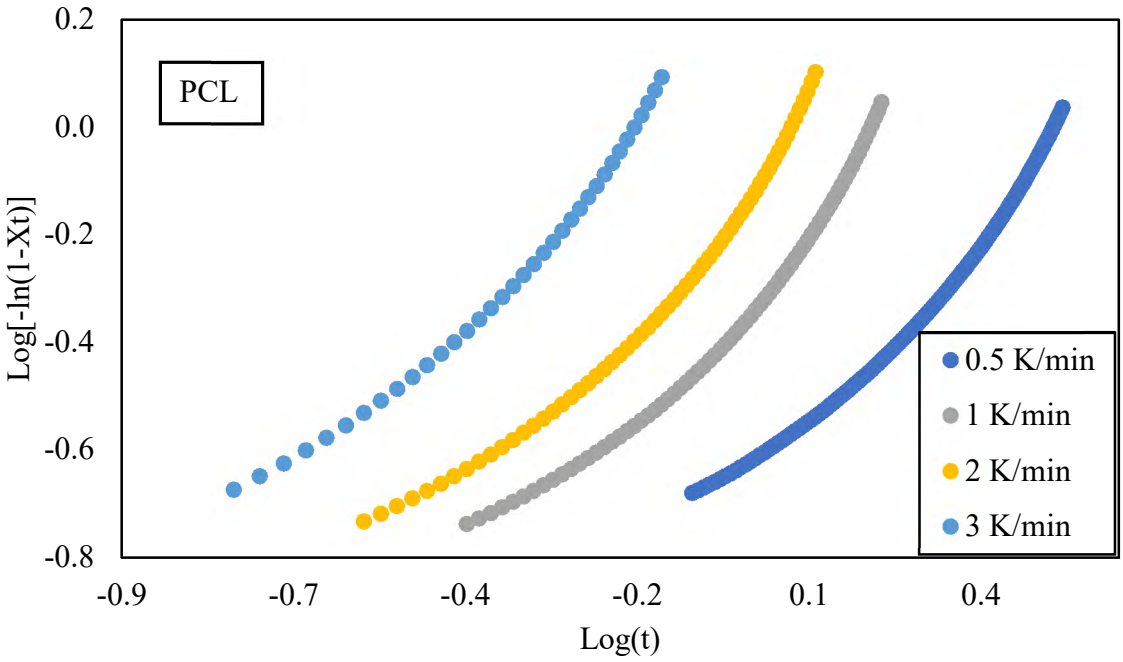


**Figure 28.** Plot of log{-ln[1-X(t)]} against log of PCL nanofibers according to Jeziorny model at various cooling rates.

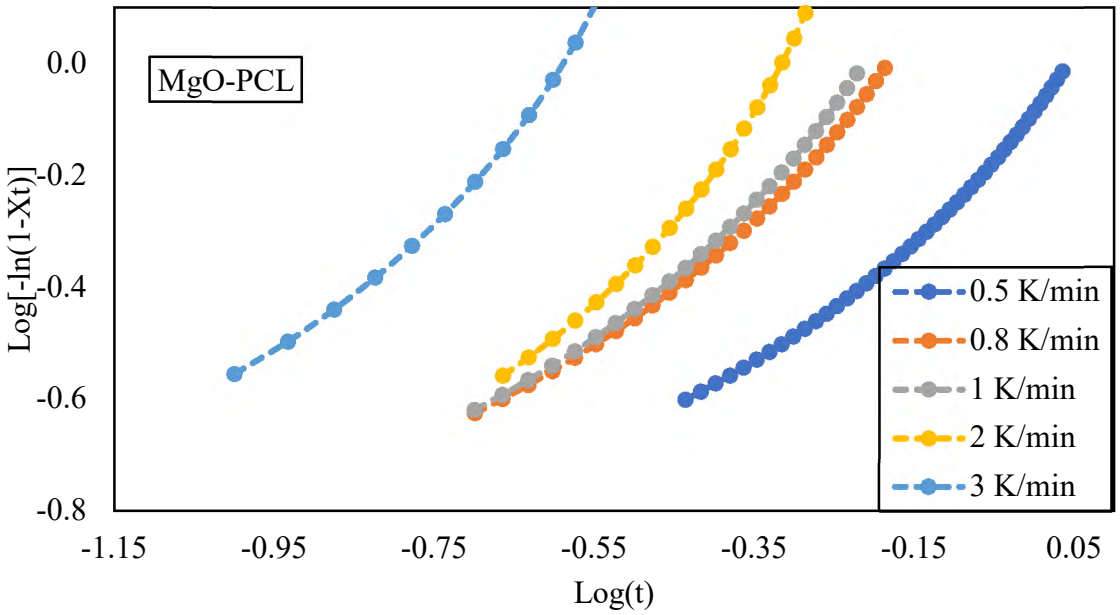


**Figure 29** Plot of log{-ln[1-X(t)]} against log of MgO-PCL nanofibers according to Jeziorny model at various cooling rates.

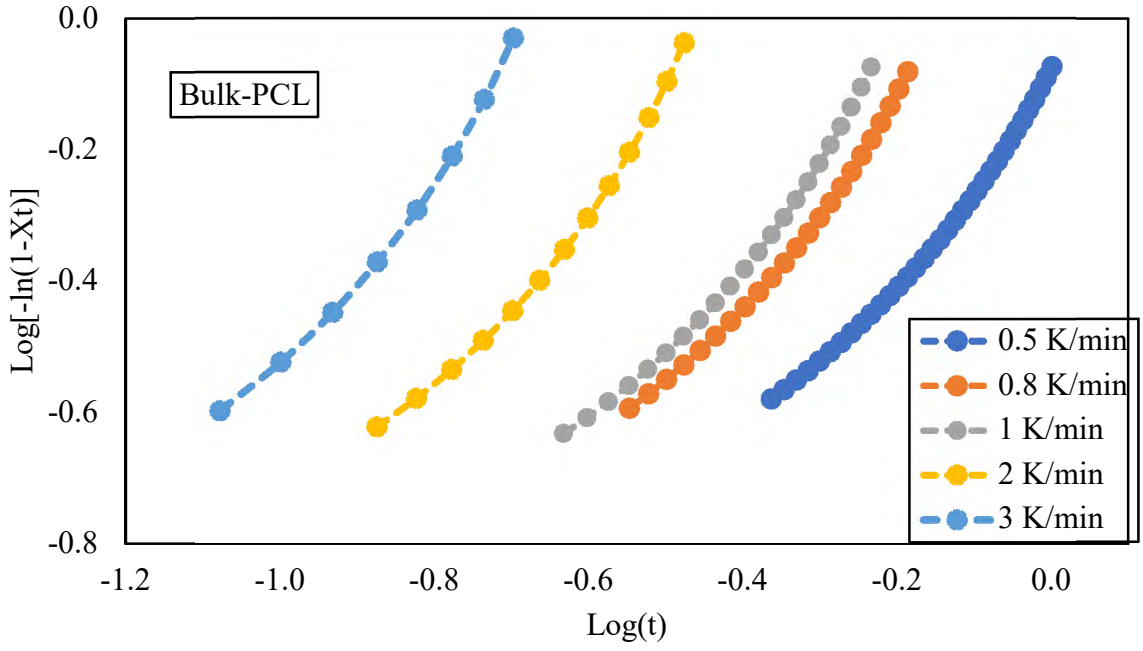


**Figure 30.** Plot of log{-ln[1-X(t)]} against log of bulk-PCL according to Jeziorny model at various cooling rates.

**Table 7** Parameters obtained from Jeziorny method for bulk-PCL, PCL, MgO-PCL nanofibers.

| Primary Crystallization Stage | | | | | |
|---|---|---|---|---|---|
| Samples | ß (K/min) | n | $Z_t$ | $Z_c$ | $R^2$ |
| PCL | 0.5 | 1.44 | 0.322 | 0.104 | 0.97 |
| | 1 | 1.29 | 0.985 | 0.985 | 0.97 |
| | 3 | 1.31 | 1.290 | 1.089 | 0.98 |
| | 4 | 1.33 | 1.966 | 1.184 | 0.98 |
| MgO-PCL | 0.5 | 1.19 | -0.156 | 0.487 | 0.97 |
| | 0.8 | 1.22 | 0.063 | 1.198 | 0.97 |
| | 1 | 1.20 | 0.179 | 1.512 | 0.97 |
| | 2 | 1.37 | 0.394 | 1.573 | 0.96 |
| | 3 | 1.22 | 0.762 | 1.795 | 0.97 |
| Bulk-PCL | 0.5 | 1.2 | -0.176 | 0.444 | 0.97 |
| | 0.8 | 1.2 | 0.109 | 1.369 | 0.96 |
| | 1 | 1.3 | 0.216 | 1.644 | 0.98 |
| | 2 | 1.2 | 0.516 | 1.811 | 0.97 |
| | 3 | 1.3 | 0.794 | 1.840 | 0.97 |

#### 5.1.3.2 Ozawa method

Considering the non-isothermal character of the process, the cooling rate (β) is the factor that needs to be considered. Ozawa method modifies the Avrami equation to

describe all non-isothermal crystallization kinetics for polymers. The mathematical model is shown as follows [66, 95]:

$$1 - X(t) = exp[-k(T)/\beta^m] \quad (26)$$

$$ln\{-ln[1 - X(t)]\} = \ln k(T) - m\, ln\, \beta \quad (27)$$

where k(T) is the kinetics crystallization rate constant and *m* is the Ozawa exponent. k(T) and *m* parameters can be obtained from the intercept and slope respectively. However, during crystallization, the Ozawa method does not consider secondary crystallization that occurs in the early stages [60].

**5.1.3.3: Mo's method**

Mo and Liu [96, 97] suggested a novel kinetic method by combining Avrami equation and Ozawa equation to describe non-isothermal crystallization kinetics [98]. Equation (10) is calculated by combining Equation (24) and Equation (27) as described below:

$$\log Z_t + n \log t = \log K(T) - m \log \beta \quad (28)$$

By solving log β, we get:

$$\log \beta = \frac{1}{m} \log \left[\frac{K(T)}{Z_t}\right] - \frac{n}{m} \log t \quad (29)$$

Let $F(T) = \left[\frac{K(T)}{Z_t}\right]^{1/m}$ and $\alpha = \frac{n}{m}$;

The final equation is transformed to:

$$\log \beta = \log F(T) - \alpha \log t \quad (30)$$

where F (T) is the cooling value chosen at a crystallization time when the system has a certain degree of crystallinity and $\alpha$ is the ratio of Avrami exponent and Ozawa exponent. Avrami exponent ($n$) and Ozawa exponent ($m$) hinge on the type of nucleation and growth mechanism. The variations of $log\ \beta$ vs. $log\ t$, for some specific relative degrees of crystallinity X (t), i.e., 20%, 40%, 50%, 60% and 80% and for pure and composite nanofibers that are considered in this study, are shown in Figure 30-32. Also, F (T) and α can be obtained from the intercept and slope.

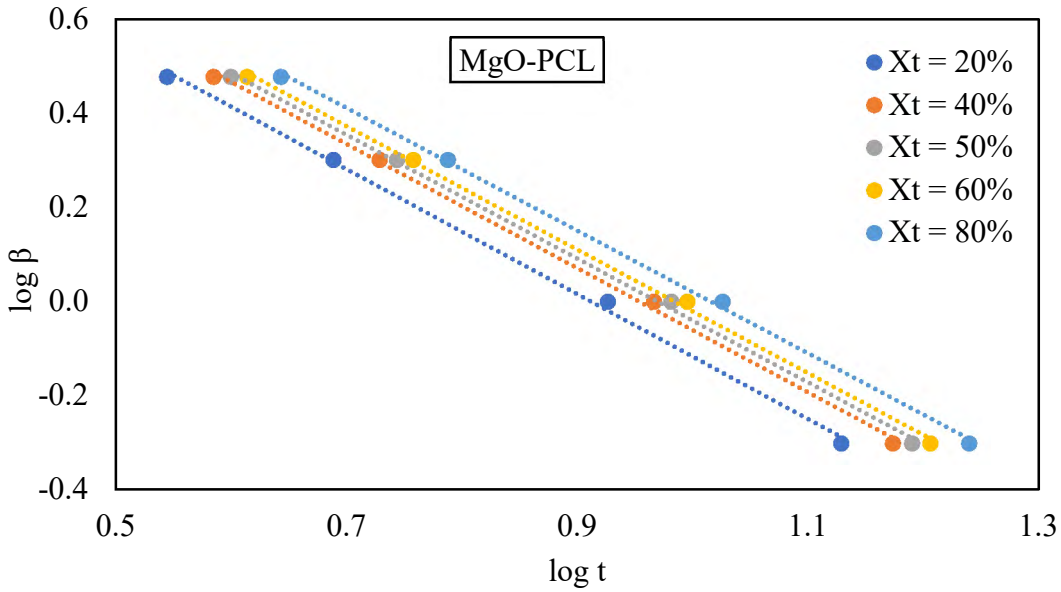


**Figure 31** Plot of log β versus log t from Mo's method for non-isothermal crystallization MgO-PCL nanofibers.

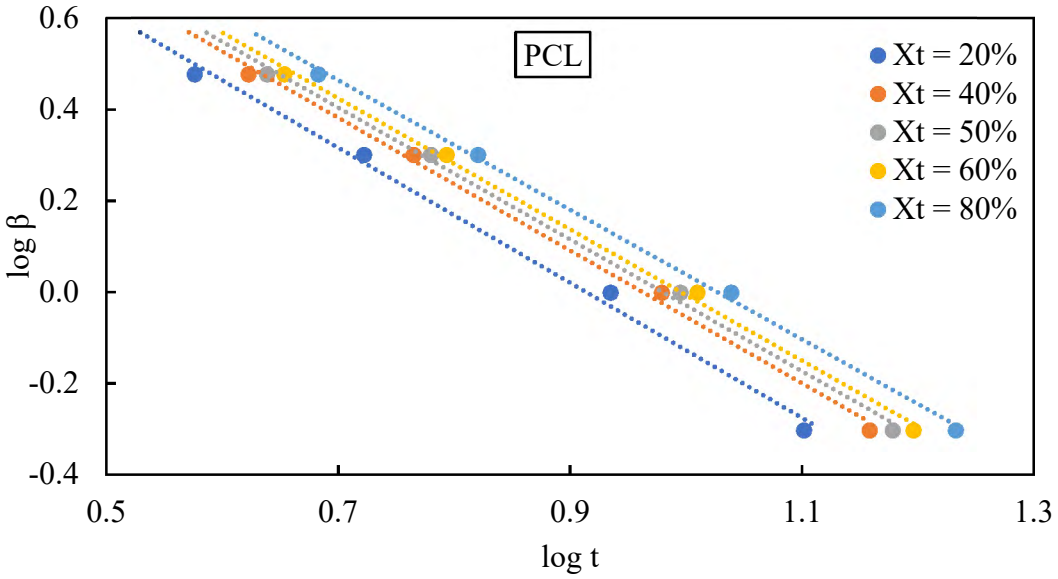


**Figure 32** Plot of log β versus log t from Mo's method for non-isothermal crystallization PCL nanofibers.

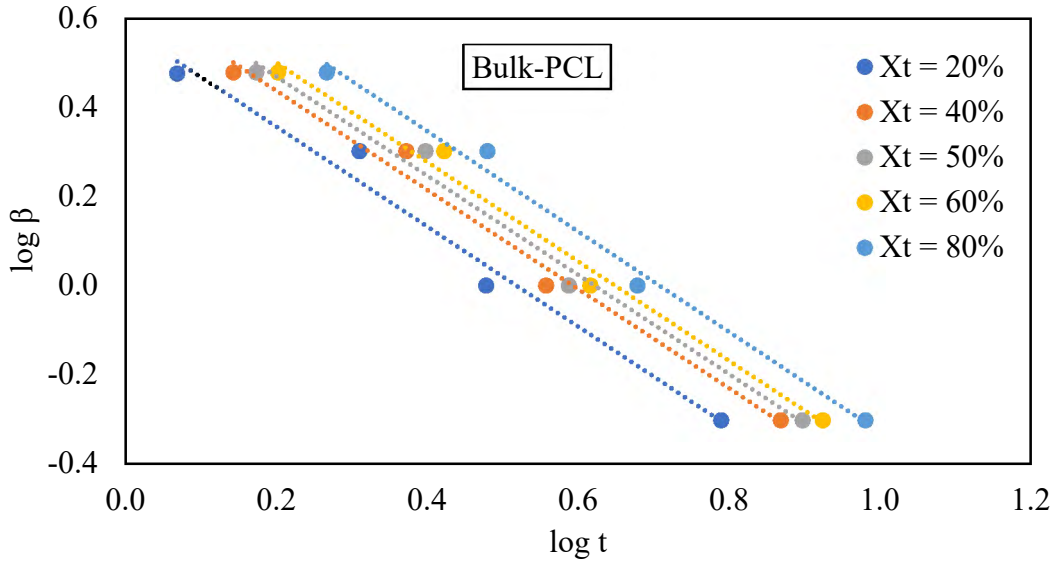


**Figure 33** Plot of log β versus log t from Mo's method for non-isothermal crystallization bulk-PCL.

The results show that the higher the cooling rate, the shorter the crystallization time for a specific relative crystallinity. The linearity as shown from these plots, best describes Mo's equation. The result is consistent with literature [67, 79, 99] they reported

Mo's model best describes the non-isothermal crystallization kinetics of polymers and polymer composites.

**Table 8** Non-isothermal crystallization kinetic parameters of bulk-PCL, PCL and MgO-PCL nanofibers obtained from Mo's method.

| Sample | $X_t$ (%) | 20 | 40 | 50 | 60 | 80 |
|---|---|---|---|---|---|---|
| Bulk PCL | F(T) | 3.81 | 4.91 | 4.56 | 5.28 | 6.25 |
| | α | 1.12 | 1.11 | 1.11 | 1.11 | 1.12 |
| MgO-PCL | F(T) | 16.25 | 18.11 | 18.83 | 19.57 | 21.07 |
| | α | 1.33 | 1.32 | 1.32 | 1.31 | 1.30 |
| PCL | F(T) | 18.84 | 21.64 | 22.66 | 23.70 | 25.75 |
| | α | 1.475 | 1.451 | 1.441 | 1.433 | 1.415 |

Table 8 shows the relationship between α, F (T), and crystallization rate. Bulk-PCL, PCL and MgO-PCL nanofibers' values of the slope (α) are at a constant of 1.1, 1.4, and 1.3, respectively. The values of α clearly show that at different relative crystallinities, the crystallization structures formed are nearly the same. In addition, the variation in the values of α for all the bulk-PCL, PCL, and MgO-PCL nanofibers were small, indicating that the method of Mo and coworkers (Equation (30)) was strongly in detailing the non-isothermal process in a process related to PP-clay nanocomposites [100], and PP-surface-treated $SiO_2$ nanocomposites [101].

The value of F (T) increases as the relative crystallinity increases. This means that a higher cooling rate is required at a set crystallization time to observe a higher crystallinity. The F (T) value of pristine PCL nanofibers is higher than MgO-PCL

nanofibers value. This shows that MgO-PCL nanofibers require less cooling rate than PCL nanofibers to obtain a given relative crystallinity. At a set relative crystallization (i.e., $X_t$ = 20%), MgO-PCL nanofibers have a lower F (T) value than PCL nanofibers. This indicates that a faster crystallization rate is observed by adding a nucleating agent with PCL nanofibers. Also, a polymer in bulk conditions (bulk-PCL) crystallizes faster than polymers in a confined state (PCL and MgO-PCL nanofibers). Similar results were obtained by Wu et al. [79], and showed composite of 1 wt.% PBT/MMT crystallized at a higher rate than that of pristine PBT.

### 5.1.4: Activation energy

The crystallization of polymers is controlled by two factors: one is the dynamic factor, which is related to the activation energy ΔE for the transport of crystalline units across the phase, and the other is the static factor which is related to the free energy barrier for nucleation [72]. The Kissinger method is widely used as a way of estimating the activation energy for non-isothermal crystallization studied by DSC. Kissinger's equation is given as follows [102]:

$$\frac{d\left[ln\left(\frac{\beta}{T_p^2}\right)\right]}{d\left(\frac{1}{T_p}\right)} = -\frac{\Delta E}{R} \tag{31}$$

where $\beta$ is the cooling rate (K/min), R is the gas constant and $T_p$ is the peak temperature at its maximum value. Using Equation (31), the Kissinger method can estimate the ΔE from the slope of a straight-line plot ln ($\beta$ /$Tp^2$) versus 1/$T_p$ as shown in Figure 33 and Table 9. Tianxi Liu et al. [98] states that an ΔE is the total activation energy which

consists of the transport activation energy that is required to transport molecular segments across the phase boundary to the crystallization surface.

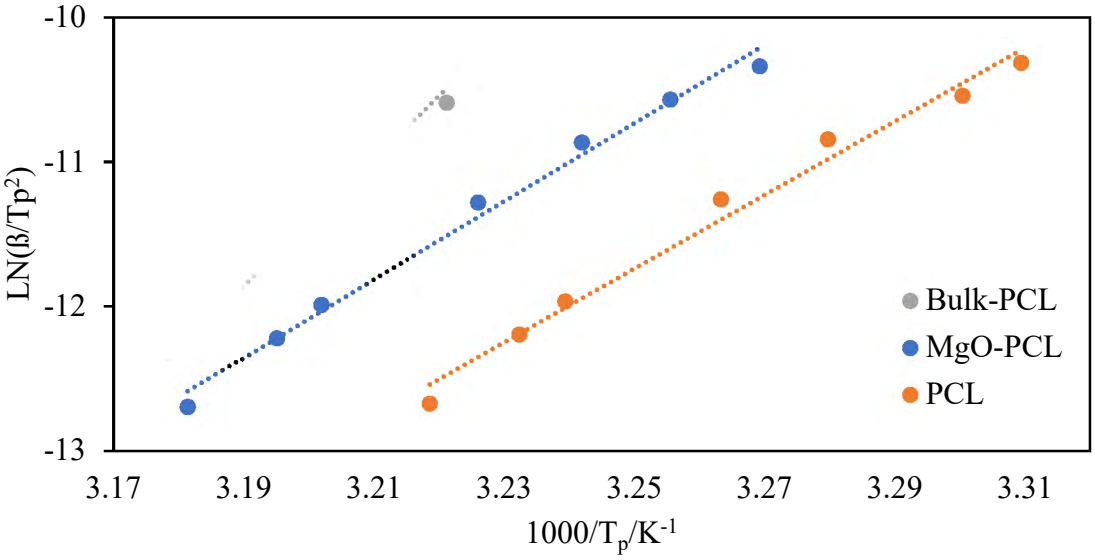


**Figure 34** Kissinger's plot for bulk-PCL, PCL and PCL-MgO nanofibers.

**Table 9** Activation energy values for bulk-PCL, PCL, MgO-PCL nanofibers.

| Samples | $E_a$ (kJ/mol) |
|---|---|
| PCL | -212.01 |
| MgO-PCL | -226.89 |
| Bulk-PCL | -364.74 |

The activation energies of bulk-PCL, PCL, and MgO-PCL nanofibers are -364.74, -212, and -226.3 kJ/mol respectively. MgO-PCL nanofibers (-226.3 kJ/mol) exhibit a slightly lower ΔE than PCL nanofibers (-212 kJ/mol). This indicates that adding 5 wt.% MgO to PCL facilitated the crystallization of PCL molecular chains and boosted crystallization rates due to the nucleation activity of MgO. Furthermore, documented is a rise in $E_a$ with increasing weight fractions of MWCNTs between 0.5 and 5% [95].

Nevertheless, Vyazovkin [68] established in 2002 that the Kissinger equation does not apply to the cooling processes. For melt crystallization, therefore, the differential iso-conversional approach of Friedman (1964) and the integral iso-conversional method of Vyazovkin (2001) are applicable. Due to its dependability and simplicity, the Friedman approach will be utilized in this study [103]. The Friedman equation is expressed as follows:

$$\ln\left(\frac{dX_t}{dt}\right)_{X_t} = constant - \frac{\Delta E_{X_t}}{\mathrm{R}T_{X_t}} \tag{30}$$

where dXt/dt is the instantaneous crystallization rate as a function of time for a given value of the relative crystallinity ($X_t$), R is the universal gas constant (J/mol K and $\Delta E_{Xt}$ is the crystallization activation energy (kJ/mol) that corresponds to crystallization temperature, $T_{Xt}$ at various cooling rates. $-\Delta E_{Xt}/R$ was determined from the slope coefficient plots of ln ($dX_t/dt$) versus $1/T_{Xt}$, and exhibited a straight line as shown in Figures 34-36 at each relative crystallinity. The regression coefficient ($R_2$) has high values which supports the effectiveness of the Friedman equation in calculating activation energy for various relative crystallinities.

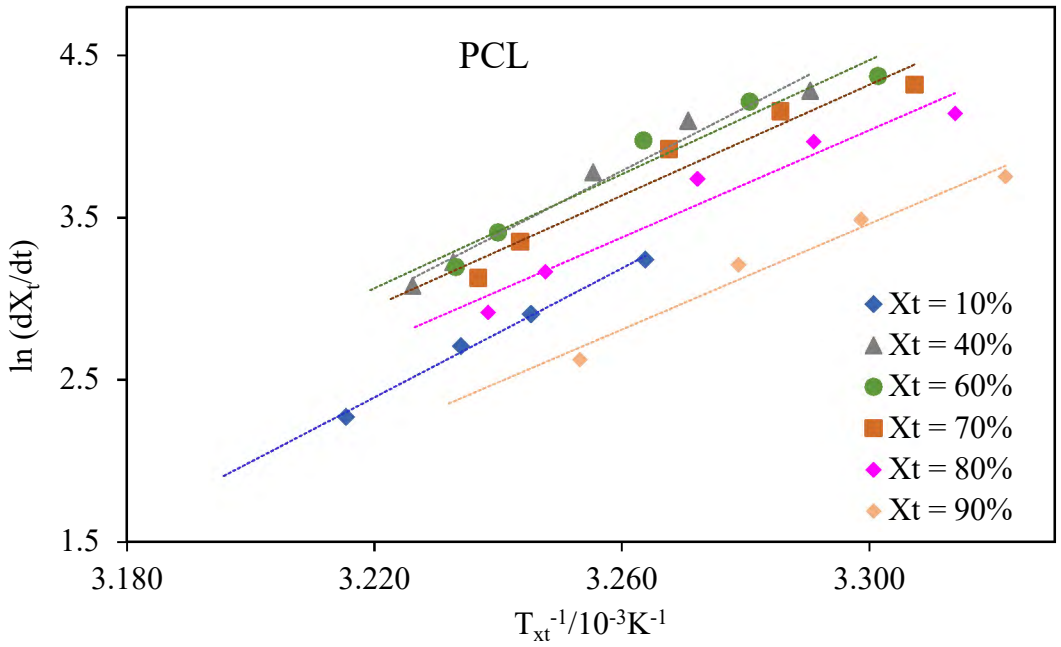


**Figure 35** Plots $\ln(dX_t/dt)$ versus $1/T_{xt}$ of PCL nanofiber at different relative crystallinities.

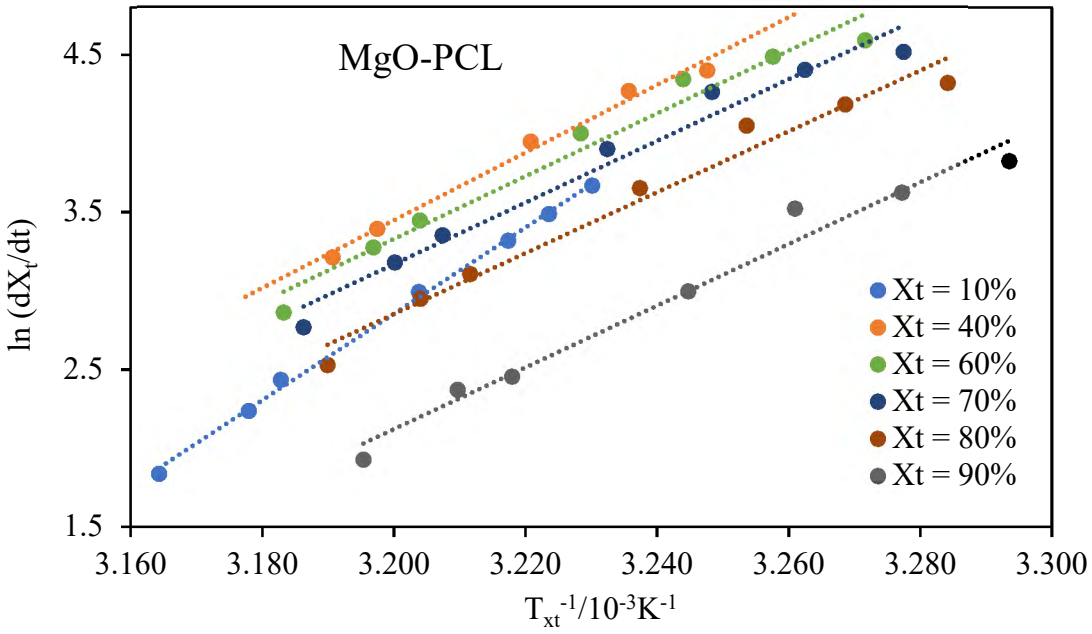


**Figure 36** Plots $\ln(dX_t/dt)$ versus $1/T_{xt}$ of MgO-PCL nanofiber at different relative crystallinities.

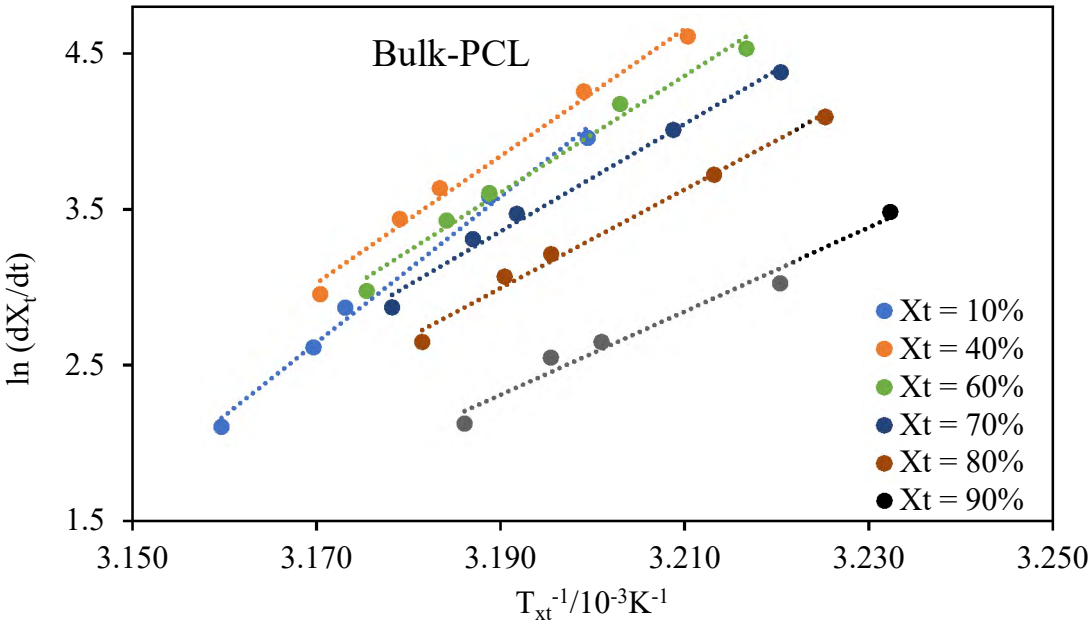


**Figure 37** Plots ln ($dX_t/dt$) versus $1/T_{xt}$ of bulk-PCL at different relative crystallinities.

Figure 37 was plotted based upon Friedman equation on the reliance of the effective energy on the relative crystallinity. All samples show that the activation energy increases as relative crystallinity increases. This suggests that the polymer difficulty of crystallization increases as the relative crystallinity increases. Activation energy for all samples follows the order: PCL nanofibers > MgO-PCL nanofibers > Bulk-PCL. Both nanofibers have a higher activation energy than bulk-PCL, suggesting that crystallinity is reduced due to nanoconfinement of the nanofibers. Also, as relative crystallinity increases, temperature reduces, and activation energy increases. Therefore, crystallization ability becomes harder as the temperature reduces. Freidman equation proves to be accurate as Kissinger's activation energy equation as shown in Table 9, provides the same result. Therefore, the higher the activation energy, the lower the crystallization ability and vice versa [104]. The results clearly indicated that the composite nanofibers

with 5 wt.% MgO presented lower activation energy than PCL nanofibers. A similar trend of activation energy was observed for clay loading on PBT for the isothermal and non-isothermal crystallization process [105].

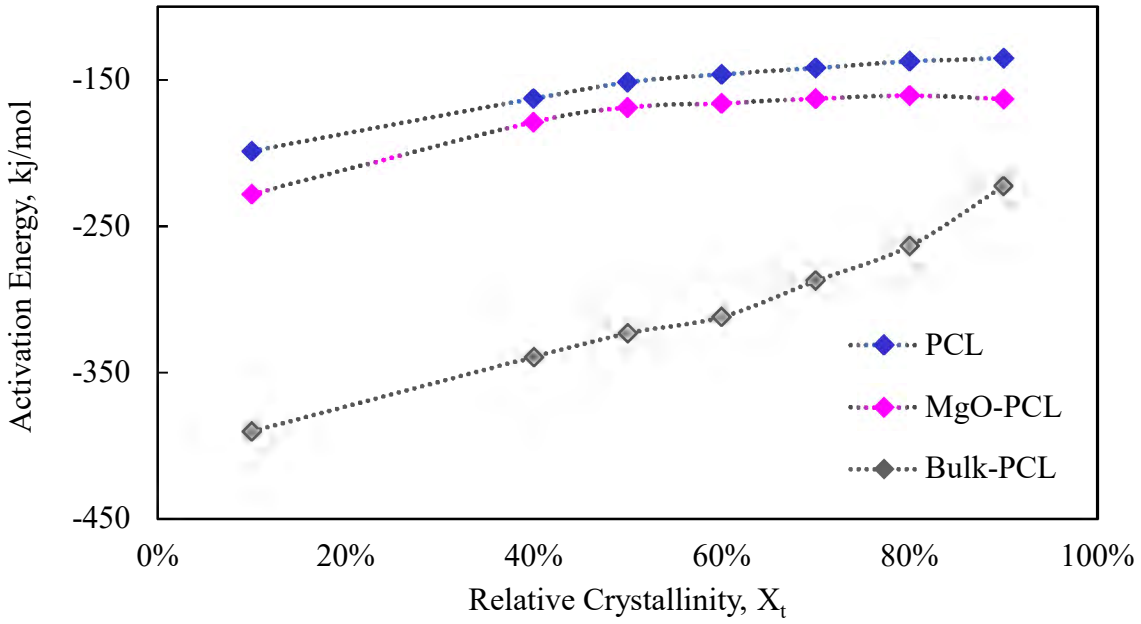


**Figure 38** Activation energy dependence on the relative crystallinity for bulk-PCL, PCL and PCL-MgO nanofibers.

## 5.2: Conclusion

DSC was used to evaluate the non-isothermal crystallization kinetics of PCL and MgO-PCL blends at varied cooling rates. Mo's method was used to examine the profile of non-isothermal crystallization kinetics, and its α value for bulk-PCL, PCL, and MgO-PCL nanofibers samples is constant. This demonstrates that the nucleation and growth mechanisms for crystals in each sample, regardless of their relative crystallinity, are remarkably comparable. In the meantime, the value of F(T) increases as relative crystallinity increases, indicating that a bigger F (T) value makes crystallization more

challenging as relative crystallinity increases. Moreover, at a given relative crystallization rate, MgO-PCL crystallizes faster than PCL.

Using the CRC and CRP methods, the non-isothermal crystallization rates of PCL and MgO-PCL nanofibers were analyzed based on their compositions and cooling rates. In both the CRC and CRP procedures, the MgO-PCL crystallization rate was rated as greater. According to CRC and CRP statistics, the following crystallization rates apply: Bulk-PCL > MgO-PCL (5/95) > PCL. Friedman's approach determined the $E_a$ values for bulk PCL, PCL nanofibers, and MgO-PCL nanofibers. As necessary energy is lost during crystallization from a melt, the activation energy is negative. Since the $E_a$ value of nanofiber is larger than that of bulk PCL, this shows that nanoconfinement makes it more difficult to transfer PCL chain segments to develop crystals.

# 6. FUTURE STUDY

Isothermal crystallization is a process whereby samples in DSC are heated, cooled, and kept under isothermal conditions [106]. The sample's crystallization kinetics are investigated using this procedure. However, the offered differential scanning calorimeter (DSC-3) from METTLER TOLEDO has restricted capabilities. The samples can only cool down to room temperature. As a result, the thermographs for isothermal crystallization for the samples were not complete, as shown in Figure 39.

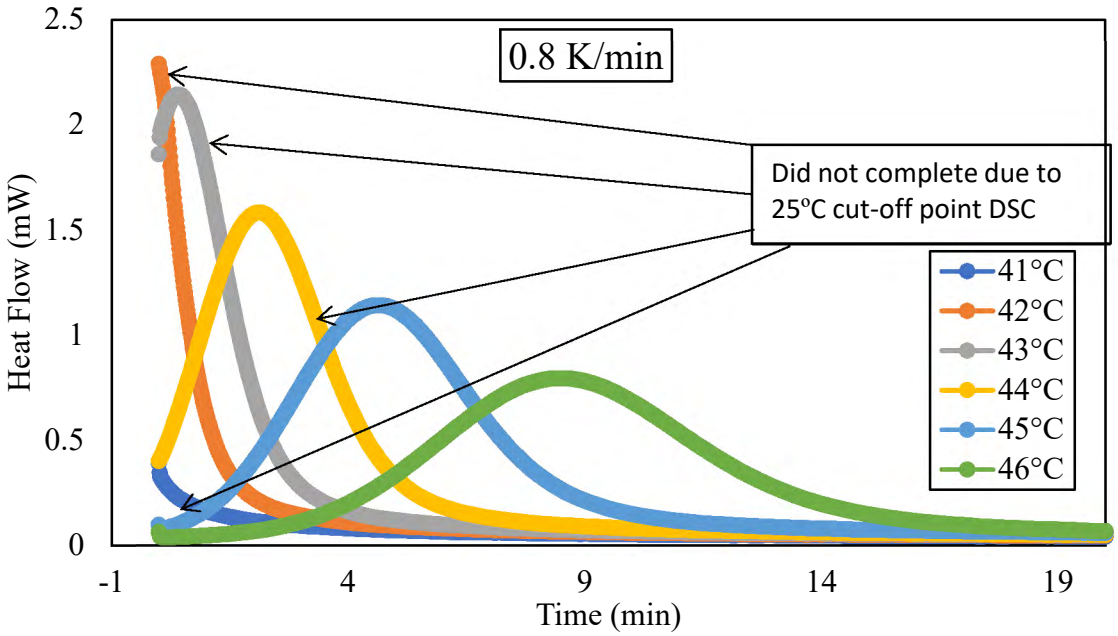


**Figure 39** MgO-PCL isothermal data by using 0.8K/min cooling rate.

Flash DSC 2+, which can analyze rapid crystallization from -95 to 1000ºC, was recently purchased through external equipment funding. Under nitrogen purge, the Flash DSC 2+ conducts calorimetry tests with a Freon intercooler [107] . An image of the new cutting-edge equipment is shown in Figure 39. A time-temperature-transformation (TTT) diagram can be made with this instrument predicting isothermal kinetics [108]. Figure 40

shows the flash DSC sensor in different magnifications [109]. These sensors give the possibility to perform heating and cooling of a single nanofiber to understand the behavior of a single crystal and its impact on polymer chain mobility.

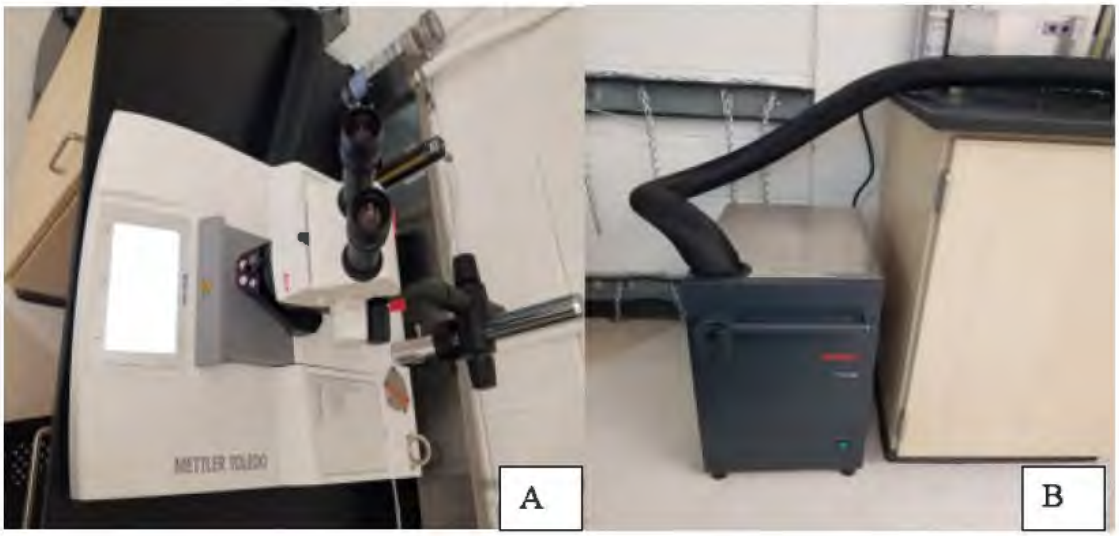


**Figure 40** Mettler Toledo Flash Differential Scanning Calorimetry (FDSC 2+) 1 (A) and Freon Intercooler (B).

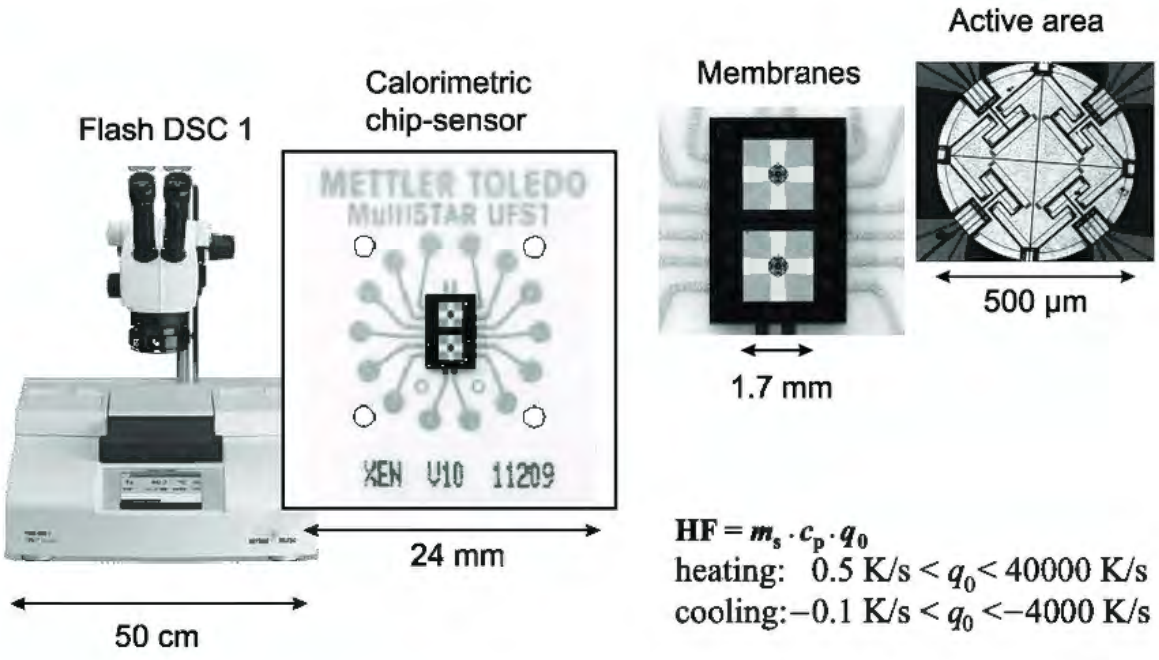


**Figure 41** Flash DSC sensor in different magnifications [109].

Bulk-PCL samples were prepared under atmospheric pressure and vacuum. Studies showed crystallinity of samples prepared under vacuum had lower crystallinity, see Table 10. Future studies will be performed to investigate crystallization kinetics for samples in both isothermal and non-isothermal conditions.

**Table 10** XRD crystallinity results of bulk-PCL of air and vacuum prepared samples.

| Samples | Crystallinity (%) | | |
|---|---|---|---|
| Bulk/PCL(Air) | 64.52 | ± | 0.090 |
| Bulk/PCL(Vacuum) | 34.86 | ± | 1.036 |

# 7. SUMMARY AND CONCLUSIONS

The morphology, chemical structure, and thermal properties of nanofibers were determined with the help of scanning electron microscopy (SEM), Fourier transform infrared spectroscopy (FTIR), differential scanning calorimetry (DSC), X-ray diffractometry (XRD), and contact angle. According to the SEM analysis, the orientation of the nanofibers was found to be both random and interconnected. The findings indicate that the crystallinity of MgO-PCL was greater than that of PCL nanofibers, as demonstrated by the similar outcomes obtained through DSC and XRD analyses. The findings additionally categorized the percentage of crystallinity as follows: bulk-PCL exhibited the highest percentage, followed by MgO-PCL and PCL nanofibers. . The findings obtained from Fourier Transform Infrared Spectroscopy (FTIR) indicate that the molecular chains exhibit alignment along the axes of Poly(ε-caprolactone) (PCL) nanofibers. Comparatively, PCL nanofibers exhibited greater absorbance intensities than MgO-PCL nanofibers. The incorporation of MgO was found to decrease the surface wettability of PCL nanofiber, as evidenced by contact angle measurements.

This investigation examined the non-isothermal physicochemical characteristics of poly(ε-caprolactone) and magnesium oxide using DSC-3, with cooling rates ranging from 0.5 to 5 K/min. Various mathematical models for kinetics analysis, such as Jeziorny, Ozawa, and Mo's models, were employed to ascertain the parameters of non-isothermal crystallization kinetics. The result shows Mo's method best described the non-isothermal crystallization kinetics profile of bulk-PCL, PCL, and MgO-PCL nanofibers. A similar α value of 1.4 was obtained for all samples, implying that the nucleation and growth mechanisms for crystals exhibit significant similarity. It was found that the

confined polymeric nanofibers crystallized at lower temperatures compared to bulk samples. The activation energy obtained through Kissinger and Friedman methodologies revealed that bulk-PCL exhibited lower activation energy than nanofibers. The results suggest that the crystal development process is hindered by nanoconfinement. Therefore, the knowledge of non-isothermal crystallization kinetics under confinement in nanofibers will be helpful for the processing of optimized scaffolds, maintaining a balance between the degree of crystallinity polymer nanofibers and the resulting properties such as wettability or mechanical properties.

# REFERENCES

[1] S. A. Formals, R. Schreiber-Gastell, "Process and apparatus for preparing artificial threads," 1934.

[2] C.M Srivastava, R. Purwar, A.P Gupt, "Enhanced potential of biomimetic, silver nanoparticles functionalized Antheraea mylitta (tasar) silk fibroin nanofibrous mats for skin tissue engineering," *International Journal of Biological Macromolecules,* vol. 130, pp. 437-453, 1 June 2019.

[3] M. Khil, D. Cha, H. Kim, I. Kim, N. Bhattarai, "Electrospun nanofibrous polyurethane membrane as wound dressing," *Biomedical Materials Research,* vol. 67B, no. 2, pp. 675-679, 2003.

[4] S. Maghsoudi , B.T Shahraki , N. Rabiee , Y. Fatahi, B. Dinarvand , M. Tavakolizadeh, S. Ahmadi, M. Rabiee, M. Bagherzadeh, A. Pourjavadi, H. Farhadnejad, M. Tahriri , T.J Webster , L. Tayebi, "Burgeoning Polymer Nano Blends for Improved Controlled Drug Release: A Review," vol. 2020, p. 4363—4392, 19 June 2020.

[5] A. Alani, J.C Knowles, W. Chrzanowski, N. Yuan-Ling, K. Gulabivala, "Ion release characteristics, precipitate formation and sealing ability of a phosphate glass–polycaprolactone-based composite for use as a root canal obturation material," *Dental Materials,* vol. 25, pp. 400-10, 2009.

[6] R. Kulkarni, E. Moore, A. Hegyeli, F. Leonard, "Biodegradable poly(lactic acid) polymers," *J Biomed Mater Res.,* vol. 5, pp. 169-81, 1971.

[7] MD. Dhanaraju, D. Gopinath, MR. Ahmed, R. Jayakumar, C. Vamsadhara, "Characterization of polymeric poly(epsilon-caprolactone) injectable implant delivery system for the controlled delivery of contraceptive steroids," *Journal of Biomedical Materials Research Part A,* vol. 76A, pp. 63-72, 2006.

[8] E. Frazza, E. Schmitt, "A new absorbable suture," *J Biomed Mater Res Symposium,* pp. 43-58, 1971.

[9] Z. Huang, Y.-Z. Zhang, M. Kotaki, S. Ramakrishna, "A review on polymer nanofibers by electrospinning and their applications in nanocomposites," *Composites Science and Technology,* vol. 63, no. 15, pp. 2223-2253, 2003.

[10] V. Leung, F. Ko, "Biomedical applications of nanofibers," *Polymers for Advanced Technologies,* vol. 22, no. 3, pp. 350-365, 2011.

[11] D. Papkov, Y. Zou, M.N. Andalib, Alexander Goponenko, Stephen Z D Cheng,Yuris A Dzenis, "Simultaneously Strong and Tough Ultrafine Continuous Nanofibers," *ACS Nano,* vol. 7, no. 4, pp. 3324-3331, 2013.

[12] M. Richard-Lacroix, C. Pellerin, "Molecular Orientation in Electrospun Fibers: From Mats to Single Fibers," *Macromolecules,* vol. 46, no. 24, pp. 9473-9493, 2013.

[13] D. Papkov, N. Delpouve, L. Delbreilh, S. Araujo, T.A. Stockdale, S. Mamedov, K. Maleckis, Y. Zou, M.N. Andalib, E. Dargent, V. Dravid, M. Holt, C. Pellerin, Y. Dzenis, "Quantifying Polymer Chain Orientation in Strong and Tough Nanofibers with Low Crystallinity: Toward Next Generation Nanostructured Superfibers," *ACS nano,* vol. 13, no. 5, pp. 4893-4927, 2019.

[14] R. Lacroix, Marie, C. Pellerin, "Orientation and partial disentanglement in individual electrospun fibers: diameter dependence and correlation with mechanical properties," *Macromolecules,* vol. 48, no. 13, pp. 4511-4519, 2015.

[15] Pai, Chia-Ling, M.C. Boyce, G.C. Rutledge, "Mechanical properties of individual electrospun PA 6 (3) T fibers and their variation with fiber diameter.," *Polymer,* vol. 52, no. 10, pp. 2295-2301, 2011.

[16] A. Charuchinda, R. Molly, J. Siripitayananon, N. Molloy, M. Sriyai, "Factors influencing the small-scale melt spinning of poly(ε-caprolactone) monofilament fibres," *Polymer International,* vol. 52, pp. 1175-1181.

[17] B. Gupta, N. Revagade, J. Hilborn , "Poly (lactic acid) fiber: An overview," *Progress in Polymer Science,* vol. 32, pp. 455-482, 2007.

[18] S. Arbab, P. Noorpanah, N. Mohammadi, M. Soleimani, "Designing index of void structure and tensile properties in wet-spun polyacrylonitrile (PAN) fiber. I. Effect of dope polymer or nonsolvent concentration," *Journal of Applied Polymer Science,* vol. 109, pp. 3461-3469, 2008.

[19] S.K Nune, K.S. Rama, V.R. Dirisala, M.Y. Chavali, "Electrospinning of collagen nanofiber scaffolds for tissue repair and regeneration. In Nanostructures for novel therapy: Synthesis, characterization and applications," in *Nanostructures for novel therapy*, Elsevier, 2017, pp. 281-311.

[20] S.Agarwal, A. Greiner, J. .Wendorff, "Functional materials by electrospinning of polymers," *Progress in Polymer Science,* vol. 38, no. 6, pp. 963-991, 2013.

[21] T.J. Sill, H.A.V. Recum, "Electrospinning: applications in drug delivery and tissue engineering," *Biomaterials,* vol. 29, no. 13, pp. 1989-2006, 2008.

[22] S. Parham, A.Z. Kharazi, H.R. Bakhsheshi-Rad, H. Ghayour, A.F. Ismail, H. Nur, F. Berto, "Electrospun nano-fibers for biomedical and tissue engineering applications: A comprehensive review," *Materials,* vol. 13, no. 9, p. 2153, 2020.

[23] B. Sowmya, P.K. Panda, "Electrospinning of poly(ε-caprolactone) (PCL) and poly ethylene glycol (PEG) composite nanofiber membranes using methyl ethyl ketone (MEK) and N N'-dimethyl acetamide (DMAc) solvent mixture for anti-adhesion applications," *Materials Today Communications,* vol. 33, 2022.

[24] A. Cipitria, A. Skelton, T.R Dargaville, P. Dalton, D.W. Hutmacher, "Design, fabrication and characterization of PCL electrospun scaffolds—a review," *Journal of Materials Chemistry,* vol. 21, pp. 9419-9453, 2011.

[25] T. Nakamura, Y. Shimizu, T. Matsui, N. Okumura, S. Hyon, K. Nishiya, "A novel bioabsorbable monofilament surgical suture made from (caprolacton , L Lactide)

copolymer," *Degradation Phenomena on Polymeric Biomaterials,* pp. 153-162, 1992.

[26] D.N Bikiaris, G.Z. Papageorgiou, D.S. Achilias, E. Pavlidou, A. Stergiou, "Miscibility and enzymatic degradation studies of poly(e-caprolactone)/poly(propylene succinate) blends," *European Polymer Journal,* vol. 43, pp. 2491-2503, 2007.

[27] H. Jiang, Y. Qian, C. Fan, Y. Ouyang, "Polymeric guide conduits for peripheral nerve tissue engineering," *Frontiers in Bioengineering and Biotechnology,* vol. 8, p. 1140, 2020.

[28] A. Edwards, D. Jarvis, T. Hopkins, S. Pixley, N. Bhattarai, "Poly(ε-caprolactone)/keratin-based composite nanofibers for biomedical applications," *Journal of Biomedical Materials Research Part B: Applied Biomaterials,* vol. 103, no. 3, pp. 21-30, 2015.

[29] N.P. Rijal, U. Adhikari, S. Khanal, D. Pai, J. Sankar, N. Bhattarai, "Magnesium oxide-poly(ε-caprolactone)-chitosan-based composite nanofiber for tissue engineering applications," *Engineering B: Solid-State Materials for Advanced Technology,* vol. 228, pp. 18-27, 2018.

[30] I. Slutsky, N. Abumaria, L. Wu, C. Huang, L. Zhang, Bo Li, X. Zhao, A. Govindarajan, M. Zhao, M. Zhuo, S. Tonegawa, G. Liu, "Enhancement of learning

and memory by elevating brain magnesium," *Neuron,* vol. 65, no. 2, pp. 165-177, 2010.

[31] C.S. ANAST, J.M. MOHS, S.L. KAPLAN, T.W. BURN, "Evidence for Parathyroid Failure in Magnesium Deficiency," *Science,* vol. 177, no. 4049, pp. 606-608, 1972.

[32] Y. Xu, Yanhong Gao, X. Wang, J. Jiang, J. Hou, Q. Li, "Internal Structure of Amorphous Electrospun Nanofiber: Oriented Molecular Chains," *Macromolecular Materials and EngineeringMacromolecular Materials and Engineering,* vol. 302, no. 7, 2017.

[33] J.M. Goodson, D. Holborow, R.L. Dunn, P. Hogan, S. Dunham, "Monolithic Tetracycline-containing Fibers for Controlled Delivery to Periodontal Pockets, J Periodontol. 54 (1983) 575–579.," pp. 575-579.

[34] M. Hajikhani, Z. Emam-Djomeh, G. Askari, "Fabrication and characterization of mucoadhesive bioplastic patch via coaxial polylactic acid (PLA) based electrospun nanofibers with antimicrobial and wound healing application," *International Journal of Biological Macromolecules,* vol. 172, pp. 143-153, 2021.

[35] Y. Liu, S. Li, W. Lan, M.A. Hossen, W. Qin, K. Lee, "Electrospun antibacterial and antiviral poly(ε-caprolactone)/zein/Ag bead-on-string membranes and its application in air filtration," *Mater Today Adv.,* vol. 12, 2021.

[36] I. Grigoriadou, N. Nianias, A. Hoppe, Z. Terzopoulou, D. Bikiaris, J. Will, J. Hum, J.A. Roether, R. Detsch, A.R. Boccaccini, "Evaluation of silica-nanotubes and strontium hydroxyapatite nanorods as appropriate nanoadditives for poly(butylene succinate) biodegradable polyester for biomedical applications," *Compos B Eng.,* vol. 60, pp. 49-59, 2014.

[37] B. Yuan, M.R.F Aziz, S. Li, J. Wu, D. Li, R. Li, "An electro-spun tri-component polymer biomaterial with optoelectronic properties for neuronal differentiation," *Acta Biomaterialia,* pp. 82-90, 2022.

[38] L. Liu, J. Zhang, X. Zou, M. Arslan, J. Shi, X. Zhai, J. Xiao, X. Wang, X. Huang, Zhihua Li, Y. Li, "A high-stable and sensitive colorimetric nanofiber sensor based on PCL incorporating anthocyanins for shrimp freshness," *Food Chemistry,* vol. 377, 2022.

[39] W. S. Khan, R. Asmatulu, M. Ceylan, A. Jabbarnia, "Recent progress on conventional and non- conventional electrospinning processes," *Fibers and Polymer,* 2013.

[40] P. Gupta, G. L. Wilkes, "Some investigations on the fiber formation by utilizing a side-by-side bicomponent electrospinning approach," *Polymer,* 2003.

[41] J. H. Harry, "Synthesis, characterization, processing and physical behavior of melt-processible acrylonitrile co- and terpolymers for carbon fibers: Effect of

synthetic variables on copolymer structure," *Virginia Polytechnic Institute and State University,* 2006.

[42] M.J. Mochane, T.S. Motsoeneng, E.R Sadiku, T.C. Mokhena, J.S. Sefadi, "Morphology and Properties of Electrospun PCL and Its Composites for Medical Applications: A Mini Review," *Appl. Sci,* vol. 9, p. 2205, 2019.

[43] F.J. Van Natta, J.W. Hill, W.H. Carruthers, "Polymerization and ring formation, ε-caprolactone and its polymers," *Am Chem Soc,* vol. 56, pp. 455-459, 1934.

[44] R.F. Storey, A.E. Taylor, "Effect of stannous octoate concentration on the ethylene glycol-initiated polymerization of epsilon-caprolactone," *Am Chem Soc,* vol. 211, pp. 114-120, 1996.

[45] T. Hayashi, "Biodegradable polymers for biomedical uses," *Progress in Polymer science,* vol. 19, no. 4, pp. 663-702, 1994.

[46] O. Coulembier, P. Degee, J.L. Hedrick, P. Dubois, "From controlled ring-opening polymerization to biodegradable aliphatic polyester: Especially poly(beta-malic acid) derivatives," *Progress in Polymer Science,* vol. 31, pp. 723-747, 2006.

[47] R. Rustgi, R. Chandra, , "Biodegradable polymers.," *Progress in Polymer Science,* pp. 1273-335, 1998.

[48] T.K. Dash, V.B. KonkimallaK, "Poly-ϵ- caprolactone based formulations for drug delivery and tissue engineering: A review," *Journal of Controlled Release,* vol. 158, pp. 15-33, 2012.

[49] T.K. Dash, V.B. Konkimalia, "Poly-ϵ-caprolactone based formulations for drug delivery and tissue engineering: A review," *Journal of controlled release : official journal of the Controlled Release Society,* vol. 158, no. 1, pp. 15-33, 2012.

[50] B. Azimi, P. Nourpanah, M. Rabiee, S. Arbab, "Poly (ε-caprolactone) Fiber: An Overview," *Engineered Fibers and Fabrics,* vol. 9, no. 3, 2014.

[51] M. Mochizuki, M.Hirami., "Structural effects on the biodegradation of aliphatic polyesters," *Polymers for advanced technologies,* vol. 8, no. 4, pp. 203-209, April 1997.

[52] B. Wang, R. Utzeri, M. Castellano, P. Stagnaro, A.J. Müller, D Cavallo, "Heterogeneous nucleation and self-nucleation of isotactic polypropylene microdroplets in immiscible blends: from nucleation to growth-dominated crystallization," *Macromolecules,* vol. 14, no. 53, pp. 5980-5991, 2020.

[53] M. Okada, "Chemical syntheses of biodegradable polymers," *Progress in Polymer Science,* vol. 27, no. 1, pp. 87-133, 2002.

[54] L.S. Nair,C.T. Laurencin, "Biodegradable polymers as biomaterials," *Progress in Polymer Science,* vol. 32, pp. 762-798, 2007.

[55] A. Merkli, C. Tabatabay, R. Gurny, J. Heller, "Biodegradable polymers for the controlled release of ocular drug," *Progress in Polymer Science,* vol. 23, pp. 563-580, 1998.

[56] V.R. Sinha, K. Bansal, R. Kaushik, R. Kumria, A.Trehan, "Poly-epsilon-caprolactone microspheres and nanospheres: an overview," *Int J Pharm.,* vol. 278, pp. 1-23, 2004.

[57] R. Langer, J.P. Vacanti, "Tissue engineering," *Science,* vol. 260, pp. 920-926, 1993.

[58] W. Hutmacher, "Scaffolds in tissue engineering bone and cartilage," *Biomaterials,* vol. 21, pp. 2529-2543, 2000.

[59] M. Khandaker , H. Progri, D.T Arasu, S. Nikfarjam, N. Shamim, "Use of Polycaprolactone Electrospun Nanofiber Mesh in a Face Mask," *Materials,* 2021.

[60] H. Zreiqat, C.R. Howlett, A. Zannettino, P. Evans, G. Schulze-Tanzil, C. Knabe, M. Shakibaei, "Mechanisms of magnesium-stimulated adhesion of osteoblastic cells to commonly used orthopaedic implants," *J. Biomed. Mater. Res,* vol. 62, pp. 175-184, 2002.

[61] A. Grozdanov, A. Buzarovska, G. Bogoeva-Gaceva, M. Avella, M.E. Errico, G. Gentile, "Nonisothermal crystallization kinetics of kenaf fiber/polypropylene composites," *Polymer Engineering & Science,* vol. 47, pp. 745-749, 2007.

[62] Y. Huang, H. Liu, P. He, L. Yuan, H. Xiong, Y. Xu, Y. Yu, "Nonisothermal crystallization kinetics of modified bamboo fiber/PCL composites," *Journal of Applied Polymer Science,* vol. 116, no. 4, p. 2119–2125, 2010.

[63] H. Daniel, W. Thomas, "Magnesium oxide nanoparticles increase osteoblast and fibroblast functions on polylactic acid composites for tendon to bone insertion applications," *International Conference on NanoTek and Exposition,* 2013.

[64] Q. Ma, M. Pyda, B. Mao, P. Cebe, "Relationship between the rigid amorphous phase and mesophase in electrospun fibers," *Polymer (Guildf),* vol. 54, p. 2544–2554, 2013.

[65] A. Arinstein, "Confinement mechanism of electrospun polymer nanofiber reinforcement," *Journal of Polymer Science Part B: Polymer Physics,* vol. 51, no. 9, pp. 756-763, 2013.

[66] Y. Li, L. Duan, L. Cheng, "Thermal analysis and crystallization kinetics of polyurethane," *Therm Anal Calorim,* vol. 135, pp. 2843-2848, 2019.

[67] L. Wang, W.M. Gramlich, D.J. Gardner, Y. Han, M. Tajvidi, "Spray-dried cellulose nanofibril-reinforced polypropylene composites for extrusion-based additive manufacturing: Nonisothermal crystallization kinetics and thermal expansion," *Journal of Composites Science,* p. 2, 2018.

[68] P. Samanta, V. Thangapandian, R. Srivastava, B. Nandan, "Non-isothermal crystallization kinetics of confined poly (ethylene oxide) in electrospun nanofibers

prepared from polystyrene/ poly (ethylene oxide) blends," *Journal of Polymer Research,* vol. 125, no. 29, 2022.

[69] S. Vyazovkin, "Is the Kissinger Equation Applicable to the Processes that Occur on Cooling," *Macromol,* vol. 23, pp. 771-775, 2002.

[70] M. Avrami, "Granulation, phase change, and microstructure kinetics of phase change. III.," *J. Chem. Phys,* vol. 9, no. 2, pp. 177-184, 1941.

[71] T. Ozawa, "Kinetics of non-isothermal crystallization," *Polymer,* vol. 12, no. 3, pp. 150-158, 1971.

[72] N.T. Phuong, V. Gilbert, "Non-isothermal Crystallization Kinetics of Short Bamboo Fiber-reinforced Recycled Polypropylene Composites," *Journal of Reinforced Plastics and Composites,* vol. 29, no. 17, p. 2576, 2010.

[73] A. Chafidz, R. Ali. S.E. Al-Zahrani, "Atomic Force Microscopy, thermal, viscoelastic and mechanical properties of HDPE/CaCO3 nanocomposites," *Journal of Polymer Research,* vol. 9860, no. 4, p. 19, 2012.

[74] W. L. Falke, A. E. Schwaneke, R. W. Nash , "Surface tension of zinc: The positive temperature coefficient," *Metall Trans,* vol. 8, pp. 301-303, 1977.

[75] Y. Shu, K. Rajathurai, F. Gao, Q. Cui, Z. Gu, "Synthesis and thermal properties of low melting temperature tin/indium (Sn/In) lead-free nanosolders and their

melting behavior in a vapor flux," *Journal of Alloys and Compounds,* vol. 626, pp. 391-400, 2015.

[76] J.P. Mofokenga, A.S. Luyt, "Dynamic mechanical properties of PLA/PHBV, PLA/PCL, PHBV/PCL blends and their nanocomposites with TiO2 as nanofiller," *Thermochimica Acta,* vol. 613, pp. 41-53, 2015.

[77] W. Hao, W. Yang, H. Cai, Y. Huang, "Non-isothermal crystallization kinetics of polypropylene/silicon nitride nanocomposites," *Polymer Testing,* vol. 29, pp. 527-533, 2010.

[78] D. Wang, B. Yang, QT. Chen, J. Chen, LF. Su, P. Chen, ZZ. Zheng, JB Miao, JS Qian, R. Xia, Y. Shi, "A facile evaluation on melt crystallization kinetics and thermal properties of low-density polyethylene (LDPE)/Recycled polyethylene terephthalate (RPET) blends," *Advanced Industrial and Engineering Polymer Research,* vol. 2, no. 3, pp. 126-135, 2019.

[79] W. Xu, G. Liang, W. Wang, S. Tang, P. He, W.P. Pan, "Poly(propylene)–poly(propylene)-grafted maleic anhydride–organic montmorillonite (PP–PP-g-MAH–Org-MMT) nanocomposites. II. Nonisothermal crystallization kinetics," *Journal of Applied Polymer Science,* vol. 88, pp. 3093-3099, 2003.

[80] D. Wu, C. Zhou, X. Fan, D. Mao, Z. Bian, "Nonisothermal crystallization kinetics of poly(butylene terephthalate)/montmorillonite nanocomposites," *Application Polymer Science,* vol. 99, pp. 3257-3265, 2006.

[81] N. Pengfei, W. Xiaojun, L. Baoying, L. Shengru, Y. Jie, "Melting and nonisothermal crystallization behavior of polypropylene/hemp fiber composites," *Journal of Composite Materials,* vol. 46, p. 203–210, 2012.

[82] K.H. Lee, H.Y. Kim, Khil M S, Y.M. Ra, D.R. Lee, "Characterization of nano-structured poly(ε-caprolactone) nonwoven mats via electrospinning," *Polymer,* vol. 44, pp. 1287-1894, 2003.

[83] E.M. Abdelrazek, A.M. Hezma, A. El-khodary, A.M. Elzayat, "Spectroscopic studies and thermal properties of PCL/PMMA biopolymer blend," *Egyptian Journal of Basic and Applied Sciences,* vol. 3, no. 1, pp. 10-15, 2016.

[84] S. Rajendran, T. Uma, "Lithium ion conduction in PVC–LiBF4 electrolytes gelled with PMMA," *Journal of Power Sources,* vol. 80, no. 2, pp. 282-285, 2000.

[85] U.S. Sajeev, K. Anoop Anand, D. Menon, S. Nair, "Control of nanostructures in PVA, PVA/chitosan blends and PCL through electrospinning," *Bulletin of Materials Science,* vol. 31, pp. 343-351, 2008.

[86] P.S. Tan, S.H. Teoh, "Effect of stiffness of polycaprolactone (PCL) membrane on cell proliferation," *Materials Science and Engineering: C,* vol. 27, no. 2, pp. 304-308, 2007.

[87] Arbab S, Noorpanah P , Mohammadi N, Zeinolebadi A, "Simultaneous effects of polymer concentration, jet-stretching, and on microstructural of wet-spun fibers,"

*Polymer hot-drawing development poly(acrylonitrile) Bulletin,* vol. 66, pp. 1267-1280, 2011.

[88] A.R. Shirvan, A. Nouri, A. Sutti, "A perspective on the wet spinning process and its advancements in biomedical sciences," *European Polymer Journal,* vol. 181, 2022.

[89] L. Feuillerat, "Effect of Melt Spinning on the Integrity of Poly(Ether Ether Ketone) for Commingled Yarn Based Composite Preforms," *Polymer Degradation and Stability,* vol. 191, 2021.

[90] T. Patrício, P. Bártolo, "Thermal stability of PCL/PLA blends produced by physical blending process," *Procedia Engineering,* vol. 59, p. 292 – 297, 2013.

[91] T. Chen, J. Zhang, "Non-isothermal cold crystallization kinetics of poly(ethylene glycol-co-1,4-cyclohexanedimethanol terephthalate) (PETG) copolyesters with different compositions," *Polymer Testing,* pp. 23-30, 2015.

[92] Y. Niu, Y. Song, H. Hou, Y. Zhu, "Synthesis, structure, and large optical limiting effect of the first coordination polymeric cluster based on an {I@[AgI (inh)] 6} hexagram block," *Inorganic chemistry,* pp. 44, 7, 2553-2559, 2005.

[93] A. Romankiewicz, T. Sterzynski, W. Brostow, "Structural characterization of α- and β-nucleated isotactic polypropylene," *Polymer International,* pp. 2086-2091, 2004.

[94] M. Labet, W. Thielemans, "Synthesis of polycaprolactone: A review," *Chem Soc Rev.,* vol. 38, 2009.

[95] X. Zhu, C.S. Wang., B. Wang, H.P. Wang, "Non-isothermal crystallization kinetics and nucleation activity of filler in polypropylene/microcrystalline cellulose composites," *Iran. Polym. J.,* vol. 17, pp. 297-309, 2008.

[96] N. Coburn, P. Douglas, D. Kaya, J. Gupta, T. McNally, "Isothermal and non-isothermal crystallization kinetics of composites of poly(propylene) and MWCNTs, Advanced Industrial and Engineering Polymer Research.," vol. 1, pp. 99-110, 2018.

[97] T. Liu, Z. Mo, S. Wang, H. Zhang, "Nonisothermal melt and cold crystallization kinetics of poly(aryl ether ether ketone ketone)," *Polym. Eng. Sci.,* vol. 37, pp. 568-575, 1997.

[98] J. Liu, Z. Mo, "Crystallization kinetics of polymers," *Chinese. Polym. Bull,* vol. 4, pp. 199-207, 1991.

[99] T. Liu, Z. Mo, H. Zhang, "Isothermal and nonisothermal melt crystallization kinetic behavior of poly(aryl ether biphenyl ether ketone ketone): PEDEKK," *Journal of Polymer Engineering,* vol. 18, pp. 283-299, 1998.

[100] R. Ou, C. Guo, Y. Xien, Q. Wang, "Non-isothermal crystallization kinetics of Kevlar fiber-reinforced wood flour/HDPE composites," *Bioresources,* vol. 6, 2011.

[101] Q. Yuan, S. Awate, R.D.K. Misra, "Nonisothermal crystallization behavior of polypropylene–clay nanocomposites.," *Eur Polym J.,* vol. 42, pp. 1994-2003, 2006.

[102] G.Z. Papageorgiou, D.S. Achilias, D.N. Bikiaris, G.P. Karayannidis, "Crystallization kinetics and nucleation activity of filler in polypropylene/surface-treated SiO2 nanocomposites," *Thermochim Acta.,* vol. 427, pp. 117-128, 2005.

[103] S. Vyazovkin, "Kissinger Method in Kinetics of Materials: Things to Beware and Be Aware of," *Molecules,* vol. 25, 2020.

[104] S. Vyazovkin, "Modification of the integral isoconversional method to account for variation in the activation energy," *J. Comput. Chem.,* vol. 22, pp. 178-183, 2001.

[105] P. Supaphol, N. Dangseeyun, P. Srimoaon, "Non-isothermal melt crystallization kinetics for poly(trimethylene terephthalate)/poly(butylene terephthalate) blends.," *Polym. Test.,* vol. 23, pp. 175-183, 2004.

[106] A. Al-Mulla, J. Mathew, S.-K. Yeh, R. Gupta, "Nonisothermal crystallization kinetics of PBT nanocomposites," *Compos. Part A Appl. Sci. Manuf.,* vol. 39, pp. 204-217, 2008.

[107] X.F. Lu, J.N. Hay, "Isothermal crystallization kinetics and melting behaviour of poly(ethylene terephthalate)," *Polymer 42,* pp. 9423-9431, 2001.

[108] N. Shamim, Y.P. Koh, S.L. Simon, G.B. McKenna, "The glass transition of trinitrotoluene (TNT) by flash DSC," *Thermochimica Acta,* vol. 620, pp. 36-39, 2015.

[109] S. Fernando, LJs Vandi, M. Heitzmann, D. Fernando, "Cure cycle optimisation of structural epoxies used in composite civil infrastructure through the use of TTT diagrams," *Construction and Building Materials,* vol. 383, 2023.

[110] C. Schick, Z. Evgeny, R. Androsch, A. Wurms. W.P. Schmelzer, "Influence of thermal prehistory on crystal nucleation and growth in polymers," *Glass: Selected Properties and Crystallization,* pp. 1-93, 2014.

# APPENDICES

## *Appendix A: Non-isothermal crystallization exotherms for all runs.*

Section 4.1 discusses crystallization exotherms in details on each run per sample.

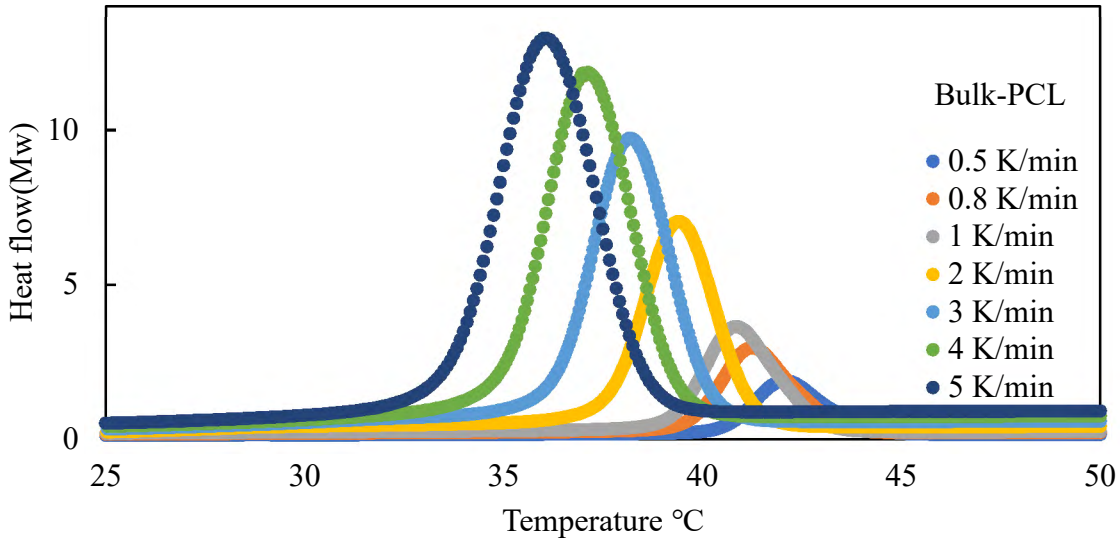


**Figure A 1.** Experiment 1: Non-isothermal crystallization exotherms of bulk-PCL measured at various cooling rates between 0.5 and 5 K/min.

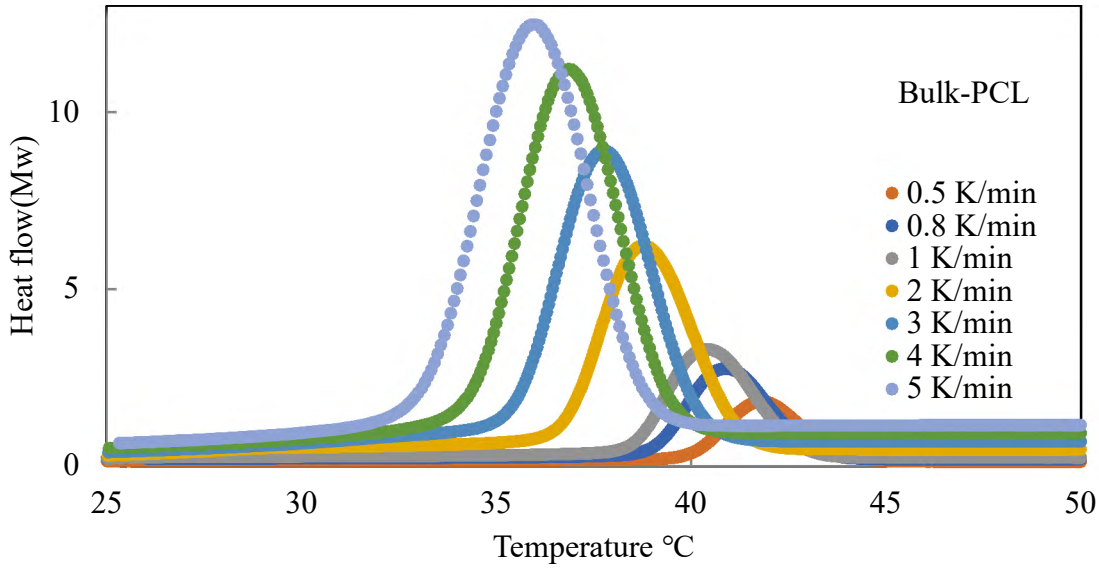


**Figure A 2.** Experiment 2: Non-isothermal crystallization exotherms of bulk-PCL measured at various cooling rates between 0.5 and 5 K/min.

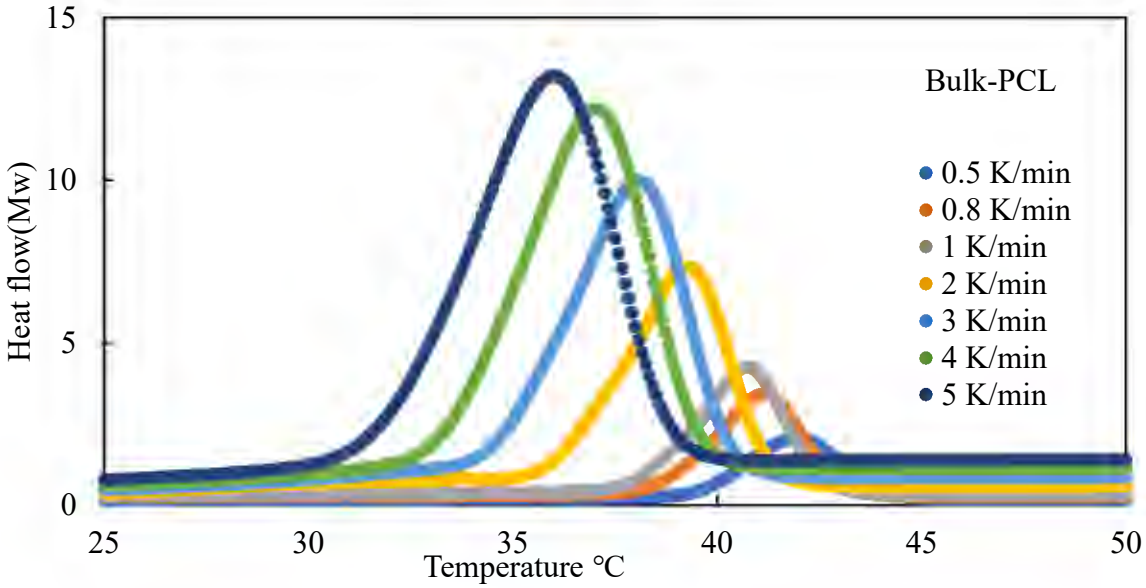


**Figure A 3.** Experiment 3: Non-isothermal crystallization exotherms of bulk-PCL measured at various cooling rates between 0.5 and 5 K/min.

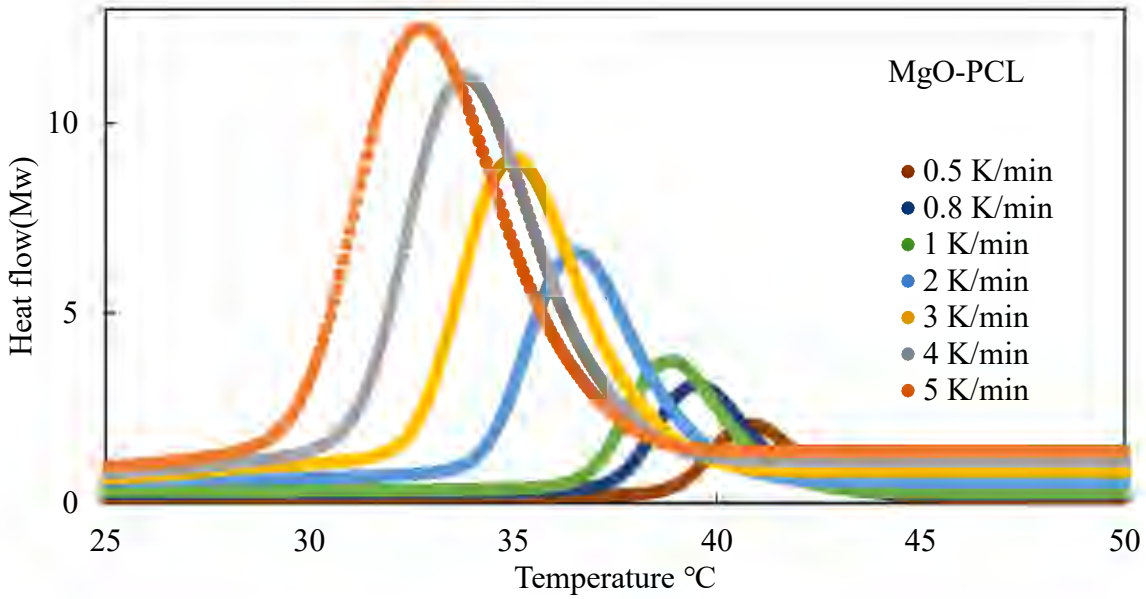


**Figure A 4.** Experiment 1: Non-isothermal crystallization exotherms of MgO-PCL samples measured at various cooling rates between 0.5 and 5 K/min.

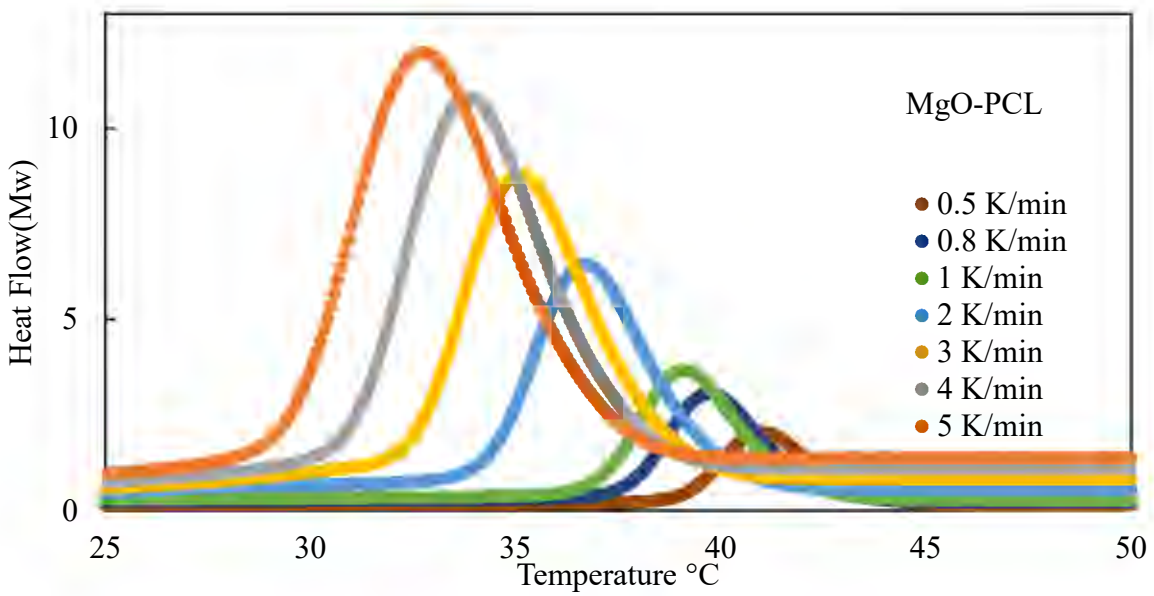


**Figure A 5.** Experiment 2: Non-isothermal crystallization exotherms of MgO-PCL samples measured at various cooling rates between 0.5 and 5 K/min.

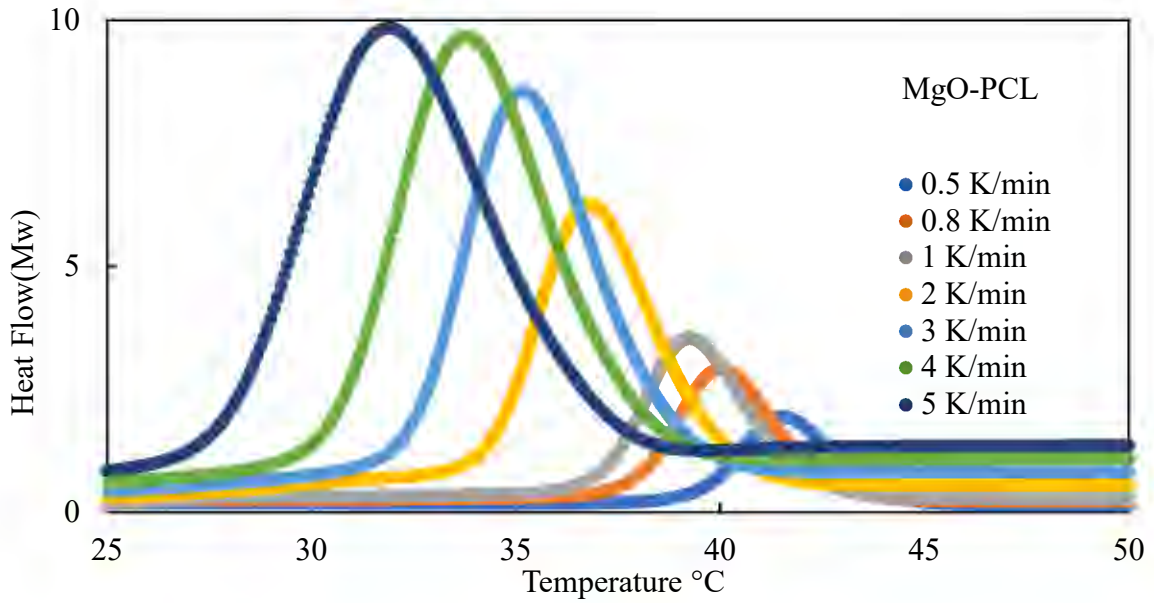


**Figure A 6.** Experiment 3: Non-isothermal crystallization exotherms of MgO-PCL samples measured at various cooling rates between 0.5 and 5 K/min.

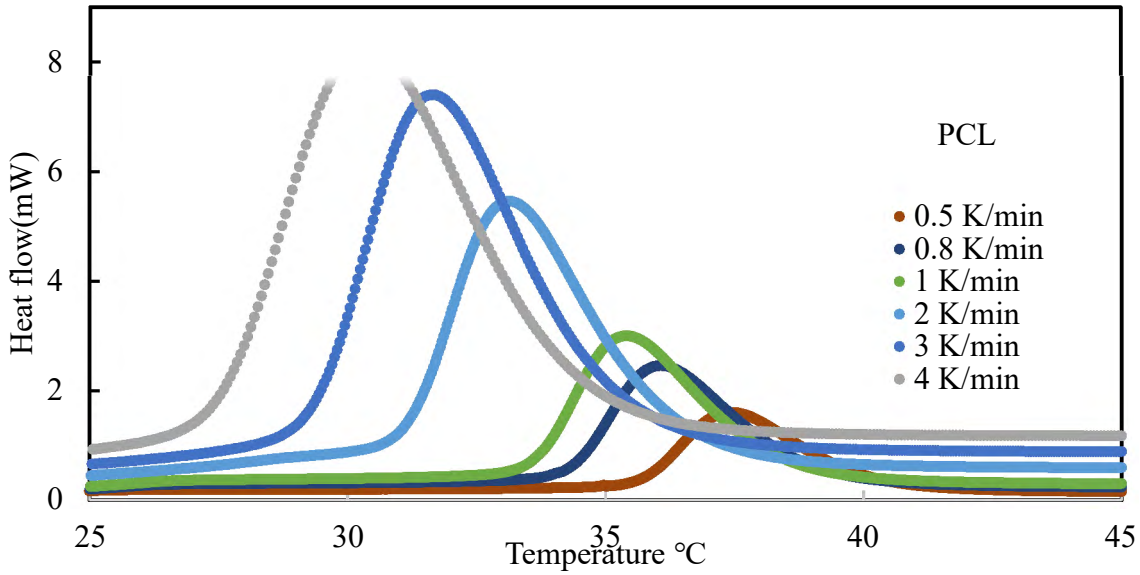


**Figure A 7.** Experiment 1: Non-isothermal crystallization exotherms of PCL samples measured at various cooling rates between 0.5 and 5 K/min.

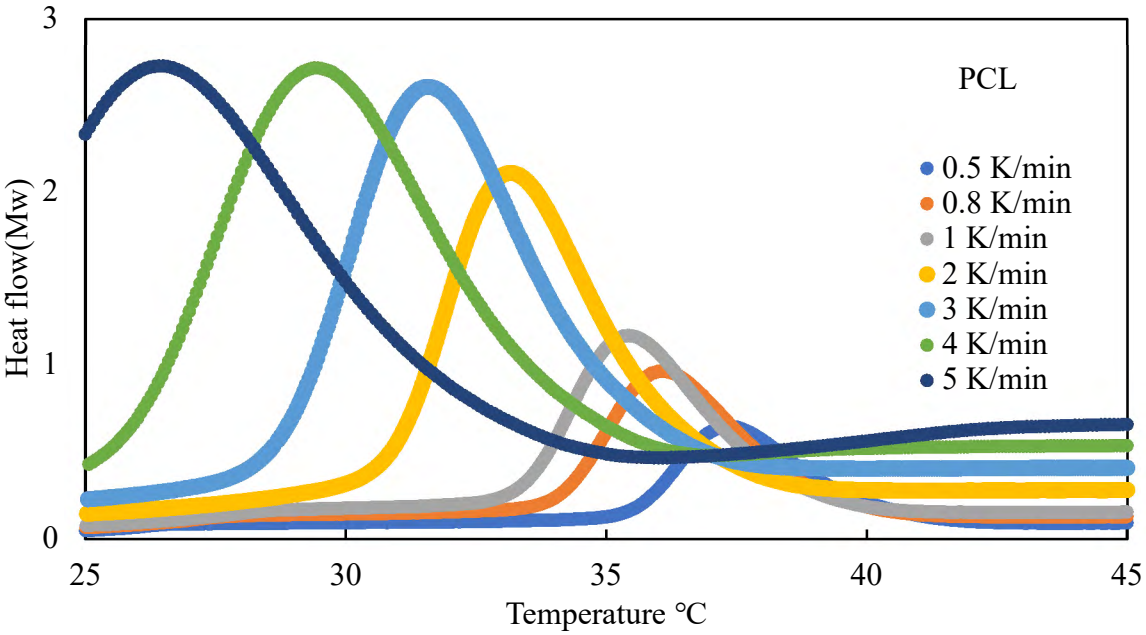


**Figure A 8.** Experiment 2: Non-isothermal crystallization exotherms of PCL samples measured at various cooling rates between 0.5 and 5 K/min.

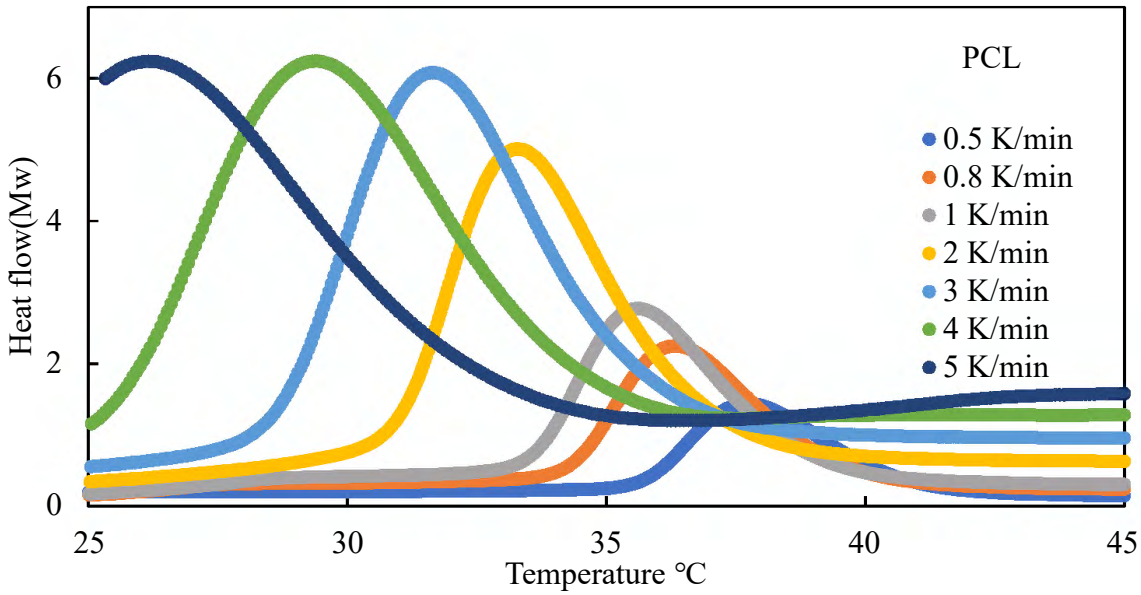


**Figure A 9.** Experiment 3: Non-isothermal crystallization exotherms of PCL samples measured at various cooling rates between 0.5 and 5 K/min.

***Appendix B: Contact Angle results***

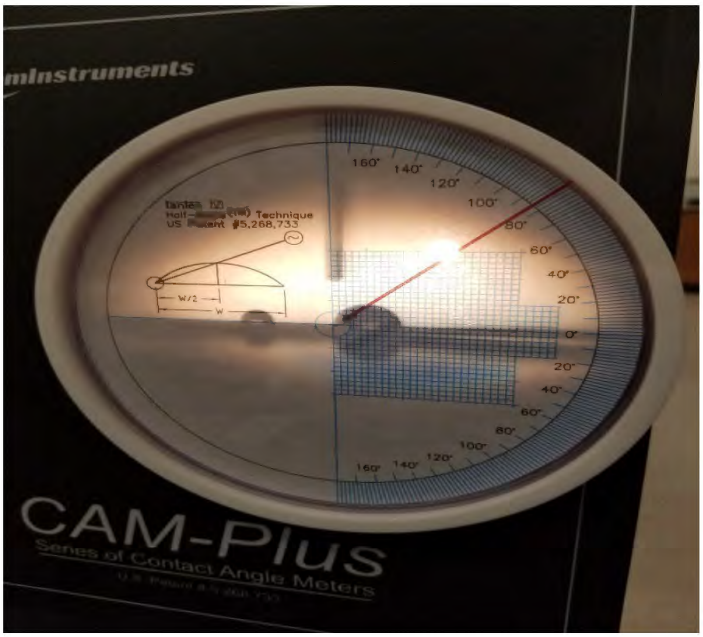


**Figure A 10.** Contact angle result of PCL nanofiber composite.

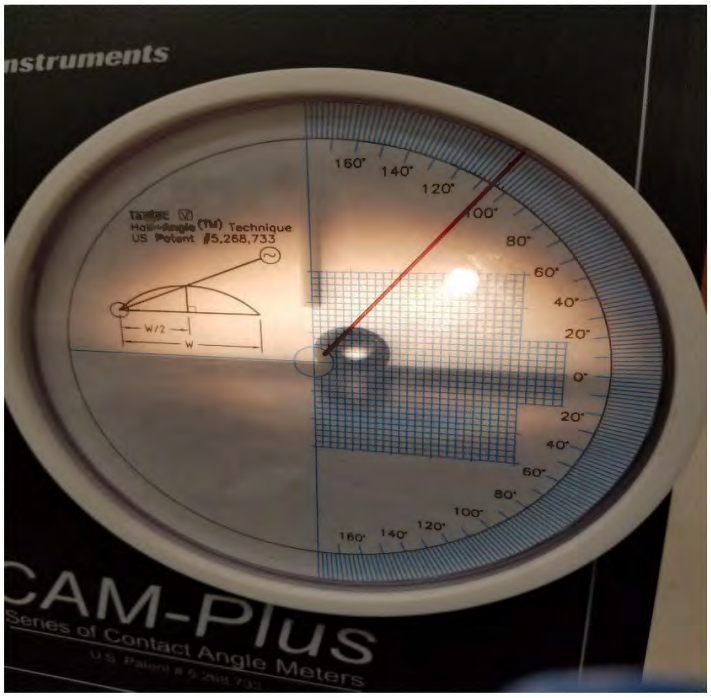


**Figure A 11.** Contact angle result of MgO-PCL nanofiber composite.

***Appendix C: X-ray diffraction results.***

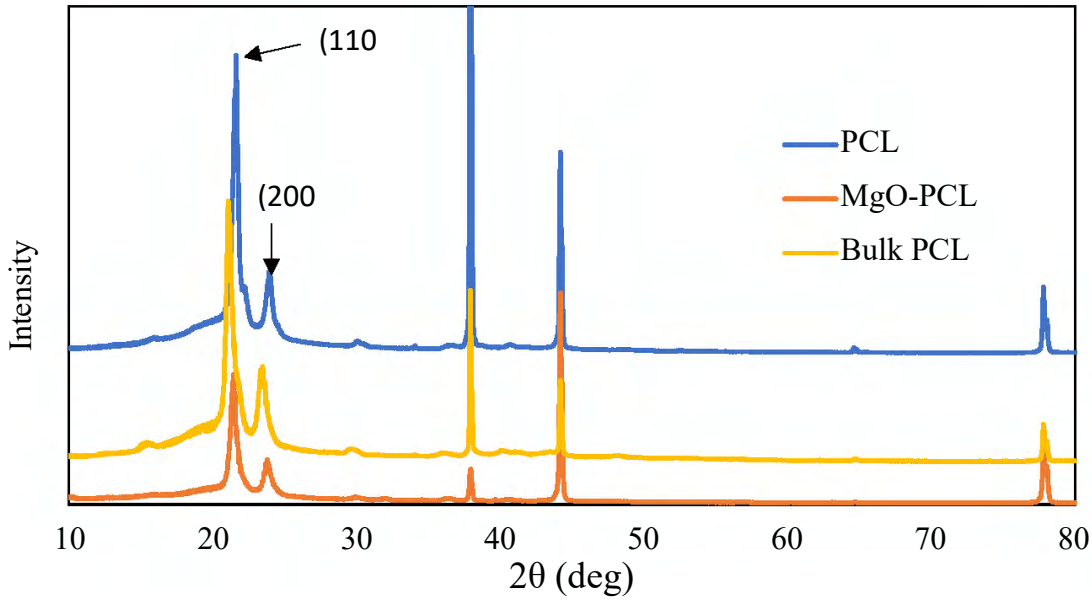


**Figure A 12.** X-ray diffraction patterns of bulk-PCL, PCL and MgO-PCL nanofibers.

**Table A 1:** X-ray diffraction data results.

| | Crystallinity | | | | |
|---|---|---|---|---|---|
| Sample | Exp 1 | Exp 2 | Exp 3 | Average | STDEV |
| PCL | 50.88 | 42.96 | 46.36 | 46.73 | 3.97469 |
| MgO/PCL | 58.19 | 56.06 | 54.84 | 56.37 | 1.69669 |
| Bulk/PCL(Vacuum) | 33.75 | 35.80 | 35.02 | 34.86 | 1.03582 |

# CURRICULUM VITAE

**Daisaku Gicheha**
**Dgicheha@pvamu.edu**

## EDUCATION

- B.A. Chemical Engineering, Prairie View A&M University, Prairie View, Texas, 2015
- M.S. Engineering, Chemical Engineering, Prairie View A&M University, Prairie View, Texas, 2023

## WORK EXPERIENCE

- Company: Prairie View A&M University
  Position: Investigate physicochemical properties of nanofibers, 2021-2023
  Job: Graduate Student Assistant

## PROFESSIONAL, TECHNICAL AND WORK-RELATED EXPERIENCE AND SKILLS

- Skilled in lab experiments and analyzing results.
- Expert in Aspen Plus & HYSYS Simulation and Microsoft Office Suite.
- Knowledgeable about Fourier transform infrared spectroscopy, Differential Scanning Calorimetry, and X-ray diffractometry characterization.

## PUBLICATIONS AND PRESENTATIONS

1. Daisaku Gicheha and Nabila Shamim, Non-isothermal Crystallization Kinetics of Poly (ε-caprolactone) (PCL) and MgO Incorporated PCL Nanofiber, Polymers, accepted, 2023.

2. Daisaku Gicheha, Morshed Khandaker, Nabila Shamim*, Physicochemical Properties of Poly (ε-caprolactone) (PCL) and MgO Incorporated PCL nanofibers, ASEE gulf southwest conference, American Society for Engineering Education, 2022, https://peer.asee.org/39196

3. Daisaku Gicheha, Aicha Cisse, Ariful Bhuiyan, Nabila Shamim*, Non-isothermal Crystallization Kinetics of Poly (ε-caprolactone) (PCL) and MgO Incorporated PCL nanofibers, MDPI, Polymers, 2023, https://www.mdpi.com/2073-4360/15/14/3013

4. Daisaku Gicheha and Nabila Shamim, Thermal Properties and Crystallinity of Poly (ε-caprolactone) (PCL) and MgO Incorporated PCL Nanofibers, AICHE Annual meeting, Phoenix, AZ Nov 13-18 2022

5. Daisaku Gicheha, Morshed Khandaker, and Nabila Shamim, Physicochemical Properties of Poly (ε-caprolactone) (PCL) and MgO Incorporated PCL nanofibers, 2022 ASEE Gulf-Southwest Annual Conference, Prairie View, TX. March 16-18 2022.